Cement-based Materials' Characterization using Ultrasonic Attenuation

A Dissertation
Presented to
The Academic Faculty

by

Wonsiri Punurai

In Partial Fulfillment
of the Requirements for the Degree
Doctor of Philosophy in the
School of Civil and Environmental Engineering

Georgia Institute of Technology
May 2006

Cement-based Materials' Characterization using Ultrasonic Attenuation

Approved by:

Dr. Laurence J. Jacobs, Advisor
School of Civil and Environmental Engineering
Georgia Institute of Technology

Dr. Kimberly Kurtis, Co-Advisor
School of Civil and Environmental Engineering
Georgia Institute of Technology

Dr. Jennifer Michaels
School of Electrical and Computer Engineering
Georgia Institute of Technology

Dr. Jianmin Qu
George W. Woodruff School of Mechanical Engineering
Georgia Institute of Technology

Dr. Jacek Jarzynski
George W. Woodruff School of Mechanical Engineering
Georgia Institute of Technology

Date Approved: March 31, 2006

To the first teacher of mine: my parents

Acknowledgements

There are many people I would like to recognize for their help and support with my research. Without them, I would not have been able to accomplish this milestone. I would like to thank my advisor Dr. Laurence Jacobs and my co-advisor Dr. Kimberly Kurtis who have always believed in my abilities and provided whatever advice and resources necessary for me to accomplish my goals. The rest of my thesis committee, Dr. Jacek Jarzynski, Dr. Jianmin Qu and Dr. Jennifer Michaels, each spent countless hours meeting with me to discuss aspects of my research and working revisions of my research study. While not officially a member of my thesis committee, Dr. Jin-Yeon Kim provided as much support as anyone else during the past few years, and added much more meaning to my work.

Next, I would like to acknowledge everyone who provided technical support. I gratefully thanks to Dr. Thomas Hsu, Dr. William Spillers, Dr. Methi Wecharatana from New Jersey Institute of Technology for giving me opportunity to pursue my PhD study here at Georgia Institute of Technology. Thank you Kritsakorn Luangvilai, Dr. Marc Niethammer, Dr. Stefan Hurlebaus and Dr. Brad Beadle, who spent much of their time for discussing and sharing their knowledge on signal analysis and on electrical components with me. Many thanks are conveyed to my friends here, Germany and back in Thailand who have given me wonderful advice, inspiration and friendship over the years. A special thanks go to Terry Vines and Besim Dragovic from Lafarge, and Grace companies.

I am indebted to Mahidol University, the Royal Thai Government and National Science Foundation for their supports during my stay in the United States. Without

this, my higher education thousands miles away from home is never possible.

Lastly, I express my deepest gratitude to my beloved parents for letting me be what I want to become, with incessant encouragement, love and understanding. I am deeply grateful to my grandpa. I am saddened by your passing. May you rest in peace and be with grandma. Also, I thank my dear three brothers for their correspondence and effort to assist me in many ways. I love you all.

Contents

List of Tables

List of Figures

Summary

The quantitative nondestructive evaluation (NDE) of cement-based materials is a critical area of research that is leading to advances in the health monitoring and condition assessment of the civil infrastructure. Ultrasonic NDE has been implemented with varying levels of success to characterize cement-based materials with complex microstructure and damage. A major issue with the application of ultrasonic techniques to characterize cement-based materials is their inherent inhomogeneity at multiple length scales. Ultrasonic waves propagating in these materials exhibit a high degree of attenuation losses, making quantitative interpretations difficult. Physically, these attenuation losses are a combination of internal friction in a viscoelastic material (ultrasonic absorption), and the scattering losses due to the material heterogeneity.

The objective of this research is to use ultrasonic attenuation to characterize the microstructure of heterogeneous cement-based materials. The study considers a real, but simplified cement-based material, cement paste - a common bonding matrix of all cement-based composites. Cement paste consists of Portland cement and water but does not include aggregates. First, this research presents the findings of a theoretical study that uses a set of existing acoustics models to quantify the scattered ultrasonic wavefield from a known distribution of entrained air voids. These attenuation results are then coupled with experimental measurements to develop an inversion procedure that directly predicts the size and volume fraction of entrained air voids in a cement paste specimen. Optical studies verify the accuracy of the proposed inversion scheme. These results demonstrate the effectiveness of using attenuation to measure the average size, volume fraction of entrained air voids and the existence of additional larger

entrapped air voids in hardened cement paste. Finally, coherent and diffuse ultrasonic waves are used to develop a direct relationship between attenuation and water to cement (w/c) ratio. A phenomenological model based on the existence of fluid-filled capillary voids is used to help explain the experimentally observed behavior.

Overall this research shows the potential of using ultrasonic attenuation to quantitatively characterize cement paste. The absorption and scattering losses can be related to the individual microstructural elements of hardened cement paste. By taking a fundamental, mechanics-based approach, it should be possible to add additional components such as scattering by aggregates or even microcracks in a systematic fashion and eventually build a realistic model for ultrasonic wave propagation study for concrete.

CHAPTER 1

Introduction

1.1 Research rationale

Cement-based materials are defined as any material that uses a mineral cement as a binder. Cement-based materials are critical building materials worldwide, with over 500 million tons produced annually in the United States alone [1]. The desired mechanical properties of cement-based materials can be readily improved by modifying the constituent components (water, cement and additives) and their relative proportions. However, improper mix design or manufacture can cause inherent defects or local imperfections. These defects can severely deteriorate material's the mechanical properties, thus jeopardizing the structural integrity and durability of the entire structure.

Characterization and condition assessment tools are needed to provide the basis for decisions on maintenance, repair and strengthening. Current assessment practice for much of the civil infrastructure consists of a visual inspection. Condition assessment is also carried out with nondestructive, or partly destructive evaluation methods. For example a hammer for sounding, ultrasonic velocity measurements, pull-out tests, electro-magnetic detections, and potential mappings can be used. Destructive methods are also available. Samples taken from a structure by core drilling can be analyzed

visually as well as with laboratory tests. Carbonation depth, determination of resistance to frost and salt scaling, as well as mechanical strength tests, can be carried out on these samples. The criteria of damage are expressed in terms of visual appearance and level concentration of depositions.

The importance of nondestructive evaluation techniques in inspection of concrete structures has increased during the last few decades. New nondestructive evaluation techniques have been created and the ones that already existed have been perfected and their applicability extended. Because of the non-invasive nature, nondestructive evaluation techniques have several advantages when compared to conventional destructive techniques. Some nondestructive evaluation methods based on the propagation of the mechanical stress waves are frequently used to assess distributed damage in materials. Properties of the propagating pulses after travelling through the damaged materials are compared with that of waves propagating through an undamaged sample to reveal microscopic changes and damaged in the inspected material's structure. Examples are acoustic emission, electrical methods, impact-echo, magnetic, radar, sonic, surface hardness, thermography, and ultrasonic.

1.2 Review of ultrasonic techniques

Previous researchers have been successful in relating the attributes of ultrasonic waves with specific material microstructure parameters in metal and ceramic materials. Truell and Hikata [2], Bratina and Mill [3], and Joshi and Green [4], for example, have successfully used the attenuation of longitudinal waves as an indicator of the fatigue damage in metals in which dislocation, microcrack, and non-uniform plastic deformation are the dominant attenuation mechanisms. Another example of the application

of amplitude attenuation is its use in characterizing the grain size distribution in polycrystalline materials and the cavity in metals [5].

The theoretical background for the use of ultrasonic wave scattering by inhomogeneities, such as grains and air voids, can also be found in Roney [6], Gubernatis and Domany [7], and Sayers [8]. As reported by Adler et al [9], Nair et al. [10], Kumar et al. [11], and Smith [12], there is a great deal of research on this topic. Attenuation of the longitudinal wave in fiber-reinforced composites has also been investigated by Mal et al. [13]. Attenuation of waves in graphite-epoxy composites laminates was studied through an ultrasonic experiment and theoretical analysis of the recorded waveforms. The specimens were immersed in water, insonified by a beam of acoustic waves from a broadband transducer, and the reflected signals are recorded by a second transducer in a pitch-catch arrangement. Results were presented for four unidirectional specimens of different thickness. A simple mode of wave dissipation was proposed and calculations based on wave propagation in the laminate were carried out. Their assumed attenuation model showed excellent agreement between measured and calculated waveforms in all four cases.

The investigation of multiple scattering of elastic waves in a fiber-reinforced composite was reported by Yang and Mal [14]. Both anti-plane (horizontally polarized shear waves) and in plane waves (longitudinal and vertically polarized shear waves) cases were considered in their studies. A multiple scattering theory and a statistical averaging procedure were implemented by means of so called Generalized Self Consistent Model. The effective phase velocity and attenuation of the coherent waves were calculated for a wide range of frequencies and fiber concentrations. The degree of interaction between fibers was determined and the average strain was calculated in a given inclusion by direct analysis and approximate homogenization was compared.

Their proposed method recovered three well-known static effective moduli of fiber-reinforced composites in the Rayleigh limit and their results at higher frequencies are physically reasonable.

1.3 Review of ultrasonic characterization of cement-based materials

In comparison, there has been a limited success in similar applications in cement-based materials. Many investigators [15– 20] have recently performed experimental studies and develop understanding of ultrasonic wave propagation in cement-based materials. They are motivated principally by the two important considerations: achieving a greater understanding of the role of microstructure in determining the mechanical properties of concrete and developing non-destructive tool for the *in situ* assessment of the remaining life potential of concrete structures. As far as the characterization of microstructure using ultrasonic measurement is concerned, this class of material is quite challenging. At first, the cement-based materials structure can be interpreted as a hierarchy of distinct levels, each possessing a characteristic length scale (Fig. 1.3), following Mehta and Monteiro [21].

At a scale of meters, e.g. concrete is considered a homogeneous material with specific engineering properties such as compressive strength, elastic modulus, and thermal expansion. At a scale of millimeters, concrete is a composite of entrained, entrapped air-filled voids and aggregates (0.1-30 mm in diameter) that are randomly dispersed in a matrix of cement paste (i.e., the solid that forms when cement reacts with water). At a scale of micrometers, cement paste is a composite of cement grains interspersed with hydration products, the two most prominent being an ionic solid that is slightly

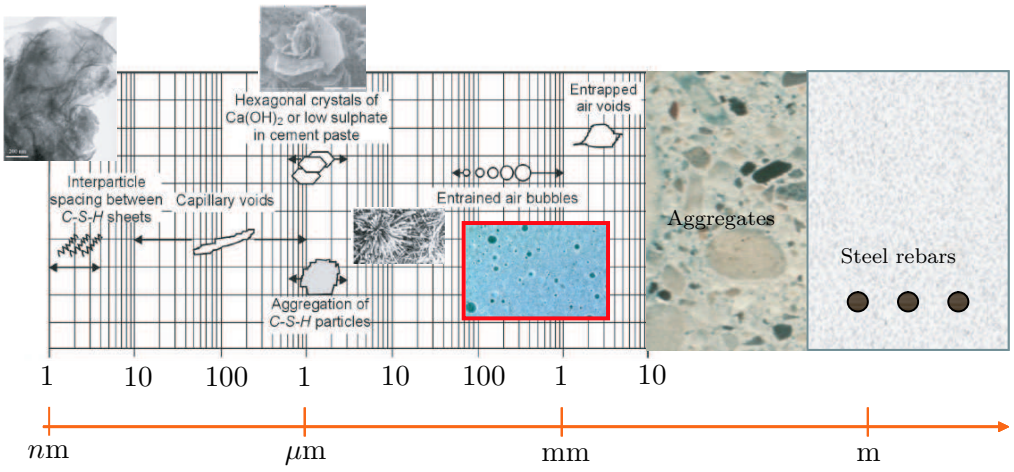

Figure 1.1: Multi-length scales existing in cement-based materials microstructure

soluble in water $Ca(OH)_2$ and a crystalline calcium silicate hydrate known as C-S-H; these products generally fail to fill all the space originally occupied by water, thus creating so called capillary pores in the paste. At a scale of tens of nanometers, the structure of C-S-H, resembling that of a particulate gel, is envisioned as agglomerates of approximately 10-20 nm in diameter that are subdivided into smaller particles approximately 5 nm across; this structure describes C-S-H at the particle level. At a scale of several nanometers, that is, at the sub-particle level, the structure of C-S-H resembles that of a disordered layered silicate. These heterogeneous length scales are seen at multiple ultrasonic wavelengths. As a result, ultrasonic waves that propagate in cement-based materials exhibit a high degree of material attenuation losses (i.e., absorption and scattering losses). That is, the recorded ultrasonic signal amplitude substantially decreases as ultrasonic waves propagate through several thicknesses and thus it is difficult to obtain and interpret actual signal amplitude transmitted into and out from the tested specimens. In addition to the dispersive nature of cement-based materials, it is often time very difficult to experimentally measure attenuation. There

are many external factors that affect the measurement of wave amplitudes. These factors include the system setting, coupling conditions between the transducer and the specimen being tested.

The understanding of the effects of each of the cement-based materials components, including concrete, mortar, paste, aggregates, cracks, and voids on attenuation characteristics is essential for the application of ultrasonic technique to characterize cement-based materials. Few researchers have attempted to perform attenuation and dispersion measurements in cement-based materials. The results of research by Suaris and Fernando [22] demonstrate the possible utilization of ultrasonic longitudinal wave attenuation to measure the growth of damage during cyclic loading of concrete specimens. A specially made transducer ring was used to hold the transducer in the circumference of a concrete cylinder when a compressive load was applied. Suaris and Fernando [22] reported a a substantial decrease in waveform amplitude, but little change in the longitudinal wave velocity during the compression test. Selleck et al. [23] performed an ultrasonic experiment by placing the freeze-thaw and salt scaling damaged concrete specimens inside a water tank. Distributed micro cracks and micro voids were produced by the freeze-thaw and salt scaling cycling. Their results show a slight variation of longitudinal wave velocity and a significant loss of ultrasonic amplitude in freeze-thaw and salt scaling damaged specimens. However, the feasibility of placing materials inside the water tank makes it unrealistic for practice.

Analysis of the longitudinal wave frequency spectrum for ultrasonic propagation in concrete have been conducted by Gaydecki et al. [24], Li [25], Berthelot et al. [26], and Daponte et al [27]. Gaydecki et al. [24] illustrated the derivations of the attenuation of exciting frequency as a function of the inhomogeneity and damage to the tested medium, as well as the propagation distance of the wave. Li on the other hand

studied the ultrasonic frequency spectrum of the longitudinal wave in concrete using compositions, including compact concrete, loose concrete, and concrete with voids. The results from his study showed that there is a shift of the peak exciting frequency in the frequency spectrum obtained from different specimens and that can be used to characterize concrete specimens with high porosity, cracking or severe segregation. Daponte et al. [27] indicated the use of Segmented Chirp Z-transform in the frequency domain analysis for the detection and monitoring of the crack growth in structural materials. However, the difficulty in separating the longitudinal and surface Rayleigh wave from the received ultrasonic signal makes this approach challenging in practical use.

Recent studies by Landis [17], Schickert [18], Popovics et al. [20], Jacobs and Owino [16] have quantified the effect of aggregate on the measured attenuation losses. These works assumed coherence between ultrasonic source and received signals and that they measured the combined attenuation due to absorption (viscoelastic effects) and scattering effects, although different setups wave types (longitudinal waves or surface Rayleigh waves) and specimens were used. Anugonda et al. [19] and Becker et al. [28] applied statistical incoherentness approach as well as diffusion theory to cement-based materials to calculate diffusion parameters (related type attenuation coefficients). Obvious changes in diffusion properties were found to resolve the differences in features of the microstructure of the specimens. Their studies illustrate the potential viability of this technique but do not conclusively provide a quantitative theoretical connection about the size or volume fraction of the microstructure of interest.

1.4 Thesis objective and hypothesis

The objective of this thesis is to develop a quantitative understanding of ultrasonic attenuation characteristics in cement paste. This study considers a real, but simplified cement-based material, cement paste, which consists of Portland cement and water, but does not include any fine or coarse aggregates. Cement paste is the binding matrix of all cement-based materials, and a quantitative understanding of attenuation in this material is a critical step in the understanding of ultrasonic wave propagation in concrete components. Better understanding in ultrasonic attenuation behavior in cement paste leads to the development of the measurement approach that uses ultrasonic attenuation to characterize microstructure of heterogeneous cement based materials.

The major hypothesis of this research is that the absorption and scattering attenuation of ultrasonic wave propagating through hydrated cement paste arising from the interaction of waves with air voids and hydrated cement paste matrix, and this varies with frequency. Experimental determination of frequency dependent attenuation can be used to quantitatively differentiate microstructure features (such as entrained air void size and volume fraction) of the hydrated cement paste. The results of the study provide a basic understanding of the effect of entrained air voids on the propagation of ultrasonic waves in the hydrated cement paste microstructure as well as supplying a first step in the characterization of the more heterogeneous microstructure in cement-based materials.

1.5 Structure of dissertation

First, this research presents the findings of the effect of distributed multiple spherical air-filled voids on systematic experimental measured attenuations obtained from cement paste specimens produced with and without a moderate percentage of entrained air voids. Next, a theoretical attenuation study, which uses a set of existing acoustics models to quantify scattered ultrasonic wavefield from a known distribution of air voids, is coupled with experimental measurements to develop an inversion procedure that directly predicts the size and volume fraction of entrained air voids cement paste specimens. Optical studies verify the accuracy of the proposed inversion scheme. These results demonstrate the effectiveness of using attenuation to measure the average size, volume fraction of entrained air voids and the existence of additional larger entrapped air voids in hardened cement paste. Finally, coherent and diffuse ultrasonic waves are used to develop a direct relationship between attenuation and water to cement (w/c) ratio. A phenomenological model based on the existence of fluid-filled capillary voids is used to help explain the experimentally observed behavior. Overall this research shows the potential of using ultrasonic attenuation to quantitatively characterize cement paste. The absorption and scattering losses can be related to the individual microstructural elements of hardened cement paste. By taking a fundamental, mechanics-based approach, it should be possible to add additional components such as scattering by aggregates or even microcracks in a systematic fashion and eventually build a realistic model for ultrasonic wave propagation study for concrete.

The cement-based materials background is given in chapter 2. Chapter 3 provides a background on wave propagation. Experimental and signal analysis used in this thesis is given chapter 4. Chapter 5 demonstrates the use of longitudinal wave attenuation

measurements to characterize entrained air voids in cement pastes. A theoretical model for attenuation behavior of longitudinal waves is applied to a two component system composed of entrained air voids and viscoelastic cement paste matrix (following Biwa [29]). The model is based on the evaluation of the energy loss of the propagating coherent wave due to the scattering by entrained air voids as well as the intrinsic absorption in the viscoelastic cement paste matrix. This model is used to demonstrate the influence of air void size and volume fraction on the attenuation coefficients. Next attenuation experiments (in the frequency range of 500kHz-5MHz) are performed in cement paste specimens with and without entrained air voids. Finally, an inversion procedure is used to predict the average size and the volume fraction of the entrained air voids. Chapter 6 presents the results of an experimental program carried out in order to quantify the effectiveness of using the inversion scheme to measure the average size and volume fraction of entrained air voids in hardened cement paste specimens. Attenuation coherent measurements are performed on a set of cement paste specimens with entrained air void contents that vary between 0 to 10%, and an inversion procedure (based on a theoretical attenuation model discussed and shown in chapter 5) is used to predict the average size and volume fraction of entrained air voids in each specimen, The accuracy of these ultrasonic predictions is verified with a direct comparison to optical results. There is very good agreement between the two set of values, demonstrating the effectiveness of using ultrasonic technique to measure air void properties. A final component discussed in the chapter is a direct relationship between attenuation and w/c ratio. A phenomenological model based on the existence of fluid-filled capillary voids is used to help explain the experimental observed absorption attenuation behavior in cement paste. Chapter 7 presents attenuation measurements using a statistical diffuse field measuring approach. As described in chapter 4, after wave propagating several distances away (or experiencing many scattering events) the average coherent wave loses its validity

and the incoherent (diffuse) wavefield gains importance. Experimentally measured ultrasonic waves can be interpreted using diffusion theory. The theory quantitatively separates absorption and scattering attenuations in terms of dissipation and diffusion coefficients. Extensive experimental results and discussions of the methods used for recovering dissipation and diffusion coefficients are described. The effect of cement paste matrix, entrained air voids, and w/c ratio on these parameters is shown. Finally, the quantitative connection between the two parameters obtained in this chapter and the attenuation coefficients obtained from the previous chapter is discovered and discussed. Conclusions and recommendations for future work are given in Chapter 8.

CHAPTER 2

Background on cement-based materials

Cement-based materials may be considered to consist of two phases: aggregates and hydrated cement paste (or a binder). The hydrated paste is comprised of cement, supplementary cementitious materials, water, and their reaction products. The paste binds the aggregates (typically sand, gravel or crushed stone of varying size and shape) and forms a rock-like mass.

2.1 Structure of the aggregate phase

The aggregate phase is generally divided into two groups: fine and coarse. Fine aggregates consist of natural or manufactured sand with solid particle sizes ranging from micron-sized fines up to 10 mm; coarse aggregates are those with particles ranging in bigger size. The chemical or mineralogical composition of the solid phases in aggregate is usually less important than the physical characteristics such as the volume size, and distribution of internal pores. In addition, the shape and texture also affect many properties of cement-based materials. For instance, the higher the proportion of elongated and flat aggregate particles, the greater tendency for water films to accumulate next to the aggregate surface causing the important phenomenon known as internal bleeding thus weakening the cement paste-aggregate interface so called the transition zone.

2.2 Structure of the hydrated cement paste

The structure of hydrated cement paste develops as a result of chemical reaction between the Portland cement and water. A summary of the structural composition of the hydrated cement paste is given in Fig. 2.1 as reproduced from Menta and Monteiro [21] and will be discussed here.

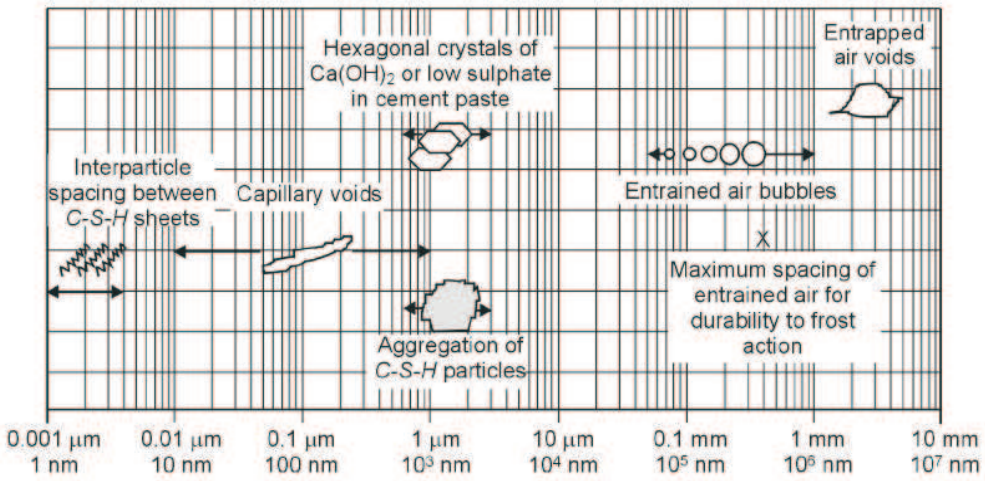

Figure 2.1: Dimensional range of solid and pore phases in hydrated cement paste [21]

2.2.1 Solids in hydrated cement paste

The types, amounts, and characteristics of the four principal solid phases generally present in a hydrated cement paste and that can be resolved by the use of electron microscope. They are as follows

> **Calcium Silicate Hydrate**, abbreviated as C-S-H, makes up 50 to 60 percent of the volume of solids in a completely hydrated Portland cement paste.The exact structure of C-S-H is not known. The colloidal dimensions a tendency to cluster full of crystals can only be resolved with the advent of electron microscopy.

Calcium Hydroxide, abbreviated as $Ca(OH)_2$ are crystals. They constitute 20-25 percent of the volume of solids in the hydrated cement paste. In contrast to the C-S-H, the calcium hydroxide is a compound with a distinctive hexagonal prism geometry. The presence of a large amount of calcium hydroxide adversely affect durability of hydrated cement paste to acid solutions because of the higher solubility of calcium hydroxide than C-S-H.

Calcium Sulfoaluminates including ettringite and monosulfate hydrate, occupy about 15 to 20 percent of the solids volume in the hydrated cement paste. Again, it is a compound with a distinctive needle-shaped prismatic crystals.

Unhydrated cement particles Depending on the rate of chemical reaction between water and cement particle, a small percentage of unhydrated cement particles can be found.

2.2.2 Voids in hydrated cement paste

In addition to the solid phases, which the aforementioned chemical reactions have produced significantly affects the properties of the hydrated cement paste. Hydrated cement paste contains several types of voids which also have important influence on hydrated cement paste properties. Through the use of electron microscopy, four types of voids can be found. They are discussed as follows.

Interlayer space in C-S-H also called "gel pores" have a volume equal to about 28% porosity in the hydrated solid paste and dimensions ranging from a few fraction of nm to several nm. These voids do not affect the durability of hydrated cement paste and its protection of the reinforcement because they are too small to allow significance transport of aggressive species.

Capillary voids are the voids not filled by the solids products of hydration of

cement paste. They have dimensions of 10 to 50 nm if the cement paste is well hydrated and produced using low water/cement ratios, but can also reach up to 3-5 μm if the paste is made using high water/cement ratios or it is not well hydrated.

Entrained air voids are the spherical air voids with diameters greater than 10 μm and less than 1 mm. They are introduced into the hydrated cement paste intentionally by means of synthetic air entraining admixtures, so as to produce resistance to freeze-thaw cycles when concrete is exposed to saturated condition during the winter. The practice of using entrained air in concrete has in generally been highly successful with few exceptions. These voids are capable of adversely affecting the compressive strength. For typical trial mixture, each 1% of added air entrainment results in a 3% to 5% loss in compressive strength (see Figure 2.2). Recently, efforts are now undertaken to understand the mechanisms of air entrainment, and testing procedures for determination of air entrained content and void characteristics in the hydrated cement paste.

Entrapped air voids are the larger pores of dimensions of up to a few mm and are the result of the air entrapped during the mixing process and not removed by the compaction of the fresh material. These voids are much bigger than the capillary voids. They are relevant to the durability of cement-based materials and its protection of the reinforcing steel. Entrapped air can be reduced by providing adequate workability to the fresh mix and proper compaction.

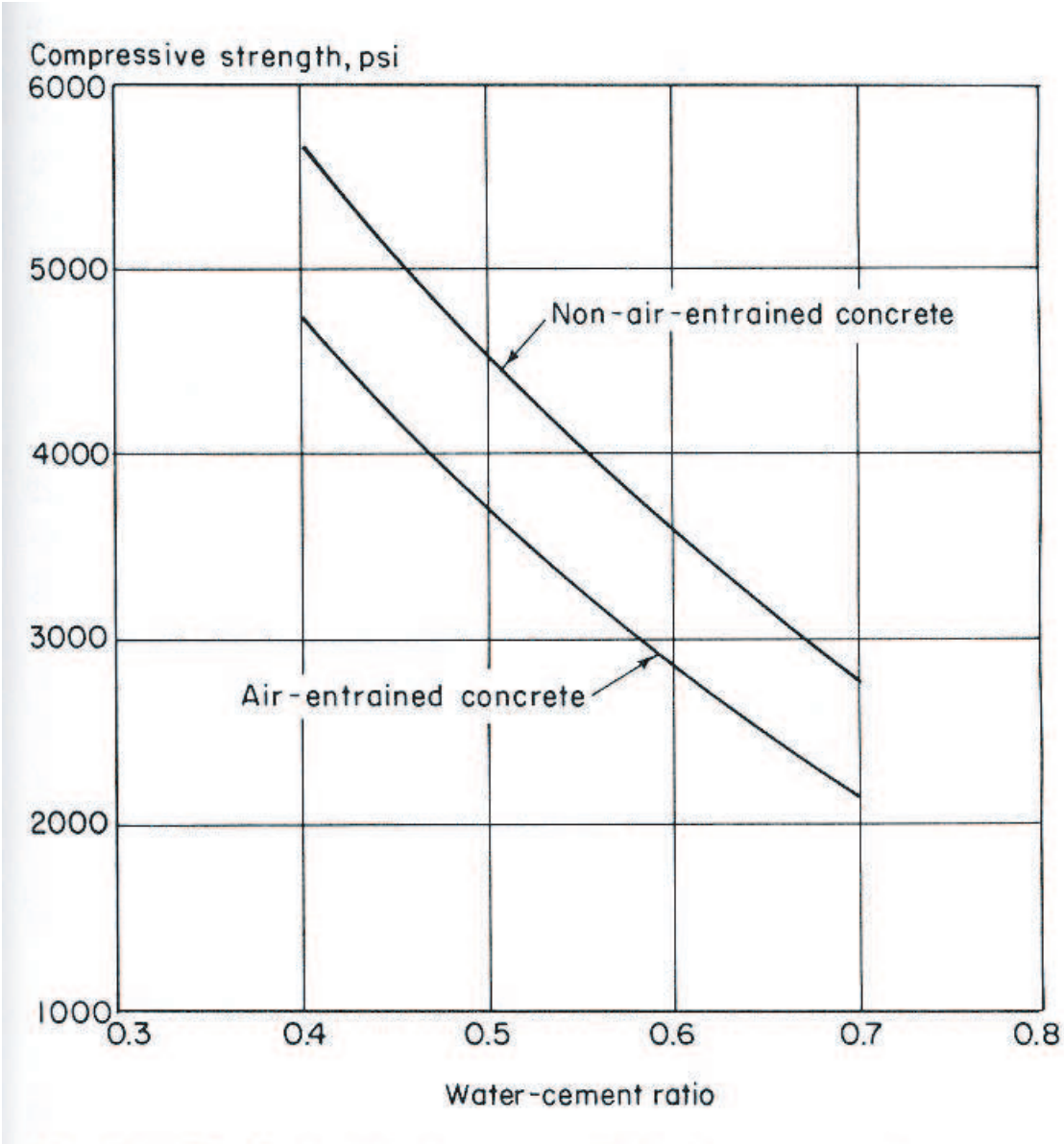

Figure 2.2: Approximate relationship between compressive strength and water to cementing materials ratio of entrained air vs. non entrained air concrete [21]

2.3 Factors to control the structure of hydrated cement paste

The ratio of water to cement materials together with curing are the two prime factors to control the aforementioned solid and void phases in the structure of hydrated cement paste. As indicated in Fig. 2.3 reproduced from Mehta and Monteiro [21], the gross volume of the cement mixture practically does not change during the hydration of cement paste.

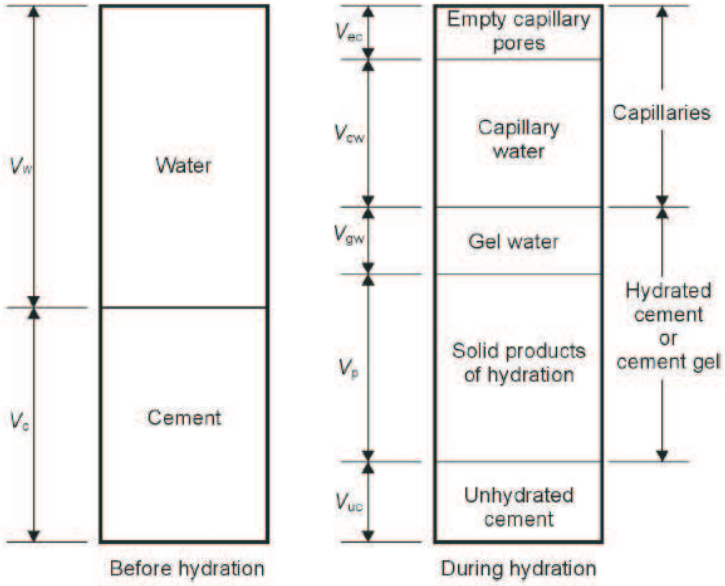

Figure 2.3: Schematic representation of the volumetric proportions in cement paste before and during hydration [21]

That is the initial volume of the system equals to the sum of the volumes of mixed water and cement particles is equal to the volume of the hydration products which is the sum of the volume of unhydrated cement grains, hydrated solid products, spaces that are filled by water or by air. The volume of the products of hydration can be assumed to be double that of the cement from which they form [30]; hence during

hydration the hydration products fill the space previously occupied by the cement that has hydrated and part of the surrounding space initially occupied by water. Therefore, if the cement-water mixture is kept moist (curing), the hydration proceeds and the volume of the pores decreases and will reach a minimum when the hydration has completed.

2.4 Time-dependent behavior

Once the hydration is completed, the casts of the original space occupied earlier by water and air are left behind. It is not surprising to find that structure of cement-based materials, especially the structure of hydrated cement paste shrinks as it dries out, so a knowledge of the changes in morphology that occur upon drying helps the understanding and prediction of shrinkage. In addition, hydrated cement paste deform progressively once subjected to a sustained load as it is said to creep. Conversely, when it is subjected to a constant strain level, the stress decreases with time and it is called relaxation of stresses [21]. The creep and relaxation of stresses are the two important phenomena in viscoelastic materials. Viscoelastic material behavior leads to attenuation that is known as material absorption [31].

2.5 Freeze-thaw deterioration

When saturated or near-saturated cement-based materials are exposed to alternating cycles of freezing and thawing, internal damage can result. As this damage accumulates, it is referred to as freeze-thaw deterioration. Freeze-thaw deterioration can occur in both the structure of the aggregate and hydrated cement paste of cement-based materials. A more detailed description of freeze-thaw deterioration of each phase is discussed as follows.

2.5.1 Freeze-thaw deterioration of aggregate

Freeze-thaw deterioration of aggregate is a distress associated with freezing and thawing of susceptible coarse aggregate particles in cement-based materials. Most susceptible aggregates are of sedimentary origin and are most commonly composed of limestone, dolomite or chert [32]. Such aggregates either fracture and or dilate as they freeze, resulting in cracking of the surrounding matrix. The best means of preventing freeze-thaw deterioration of aggregate is by prohibiting the use of susceptible aggregate, or creating a protective hydrated cement paste to prevent excess moisture buildup.

2.5.2 Freeze-thaw deterioration of hydrated cement paste

Hydrated cement paste freeze-thaw damage is considered to be a physical phenomenon arising from excess internal pressure buildup resulting from the freezing action of water. Damage related to freezing and thawing of saturated or near-saturated hydrated cement paste can occur internally or at the surface. To protect hydrated cement paste from freeze-thaw damage, the hydrated cement paste should be air-entrained by adding a surface active agent to the cement mixture. This creates a large number of small spherical air voids known entrained air voids in the hydrated cement paste. The entrained air voids relieve the pressure build-up by acting as expansion chambers. An excellent review of the literature related to this phenomenon is provided by Powers [33] and recently by Du and Folliard [34]. According to ACI [35], about $3-8\%$ entrained air contents of concrete is recommended and the entrained air voids should be well distributed within the hydrated cement paste. Adapted from ACI committee 201 report [35], Table ? shows a typical requirement for the air contents for frost resistance concrete given for the two conditions of exposure: severe and moderate.

Table 2.1: Recommended air contents for frost-resistance concrete [35]

Nominal maximum aggregate size, in. (mm)	Average air content, (%)*	
	Severe exposure†	Moderate exposure‡
3/8 (9.5)	7-1/2	6
1/2 (12.5)	7	5-1/2
3/4 (19.0)	6	5
1 (25)	6	5
1-1/2 (37.5)	5-1/2 §	6 §
3 (75)	4-1/2 §	3-1/2 §
6(150)	4	3

* A reasonable tolerance for air content in field construction is $\pm\ 1 - 1/2\%$

† Outdoor exposure in a cold climate where the concrete maybe in almost continuous contact with moisture before freezing or where deicing salts are used. Examples are pavements, bridge decks, sidewalks and water tanks.

‡ Outdoor exposure in a cold climate where the concrete will be only occasionally exposed to moisture before freezing and where no deicing salts will be used. Examples are certain exterior walls, beams, girders, and slabs not in direct contact with soil.

§ These air contents apply to the whole as for the preceding aggregate sizes. When testing these concretes, however, aggregate larger than 1-1/2 in. (37.5 mm) is removed by handpicking or sieving and the air content is determined on the minus 1-1/2 in. (37.5 mm) fraction of the mixture. (The field tolerance applies to this value.) From this, the air content of the whole mixture is computed.

Note: There is conflicting opinion on whether air contents lower than those given in the table should be permitted for high-strength (approximately 5500 psi)(37.8 MPa) concrete. The committee believes that where supporting experience and experimental data exist for particular combinations of materials, construction practices and exposure, the air contents can be reduced by approximately 1%. (For nominal maximum aggregate sizes over 1-1/2 in. (37.5 mm), this reduction applies to the minus 1-1/2 in.(37.5 mm) fraction of the mixture.

2.6 Methods for characterization of air-void system in hydrated cement paste

Despite the overall successful application of air entraining agents in concrete, it is important to ensure that an adequate system of air entrainment in terms of both the volume of air, the typical size of the air void, and the spacing of the voids-is achieved in ensure adequate durability. Several methods can be used for measuring air void content in hydrated cement paste. The more or less sophisticated ways such as the measurement of the penetration of mercury under pressure, or by the measuring the loss of moisture in a saturated sample equally yield the same result. Recently, however, it has been established that these measurements can alter the geometry of the air-void system [36], which may result in an erroneous data thus other methods are now commonly used instead.

The more actively used methods in examination of air void content in hydrated cement paste are the pressure method, the volumetric method and the gravimetric method [37– 38]. The pressure method is based on the principle that only significantly compressible ingredient of fresh cement mix is the air. The volumetric method relies on simple displacement of air with water in a vessel of pre-calibrated volume. The gravimetric method can be used to determine the air content based on the unit weight of fresh cement paste. The specific gravities (densities) of all materials must be known so that the theoretical unit weight (without air) can be determined and then compared with the actual unit weight to determine air content. The actual unit weight is determined by weighing a known volume of fresh cement mixes.

When air void content in fresh cement paste is compared to air content in hydrated cement paste, differences can exist. The way cement paste is produced and handled

can have a significant effect on its air content and its air-void system. Variables associated with production include the methods of batching, mixing procedures, and time and speed of mixing. Construction-related variables and field conditions such as transport and delivery, retempering, placement, consolidation, finishing, and temperature can also greatly alter the air content and the air-void system of cement paste. To obtain air void content in hydrated cement paste, it is often time needed for a polished section of hydrated cement paste to be taken from a laboratory beam, field cylinder, or core and tested by a petrographer according to ASTM C457, Standard Test Methods for Microscopically Determination of Parameters if the Air-Void System in Hardened Concrete [39]. The results of this test are neither timely nor inexpensive. The method also yields the total air content in the hydrated cement paste rather the size, number of voids and specific between specific air void types (e.g. entrained and entrapped air voids) which is what affect the strength and the durability of concrete.

Ultrasonic methods show the potential to be fast, reliable, inherently safe tools to quantitatively measure and characterize the air-void system in cement pastes. Refering to section 1.2, a number of researchers have developed correlations between ultrasonic wave properties (such as phase velocity and attenuation) with microstructural porosity in other materials, but not in cement-based materials. In this thesis, the potential of using attenuation to characterize air-void system in hydrated cement paste is addressed.

CHAPTER 3

Background on wave propagation

This chapter provides a brief introduction to the basic principles of ultrasonics stress wave propagation in solids. First, geometrical acoustics applying to homogeneous, isotropic, linearly elastic solids are presented. The microscopic structure is considered to have characteristic lengths much smaller than the lengths arising in the deformations of the material. Thus, the propagation is unaffected by the microstructure. Next the pressure wave reduction in real materials due to scattering and absorption, is discussed. The effect of pressure wave of from the divergence of the wavefield is also presented. Then, the frequency dependence of scattering from inhomogeneities is discussed. Lastly, the total wave field in a randomly scattering medium is briefly presented. Interested reader is referred to books on wave propagation theory for details [40],[41],[42].

3.1 Propagation of stress wave in solids

In linear elasticity, the traction t_i on a plane within a solid $n_i x_i = d$ is given by

$$t_i = \sigma_{ij} n_j, \tag{3.1}$$

where σ_{ij} is the stress tensor.

The balance of linear momentum for a solid body with volume V and surface S can be expressed as

$$\int_S \sigma_{kl} n_k dS + \int_V \rho f_l dV = \int_V \rho \ddot{u}_l dV \tag{3.2}$$

with ρ representing the material mass density and f_i the body force. Gauss' theorem applied to Eq.(3.2) leads to

$$\int_V (\sigma_{kl,k} + \rho f_l - \rho \ddot{u}_l) dV = 0 \tag{3.3}$$

Eq.(3.3)has to be fulfilled for any arbitrary volume V of the solid body, and therefore the stress equations of motion becomes

$$\sigma_{kl,k} + \rho f_l = \rho \ddot{u}_l \tag{3.4}$$

Ultrasonic testing utilizes mechanical waves being composed of oscillations of particles in the material. It is more efficient to have the equations of motion given solely in terms of the displacement, u_i (as opposed to Eq.(3.4), which has terms of stress σ_{ij} and displacement u_i). This can be achieved by applying Hooke's law. For a homogeneous, isotropic and linear elastic solid, the generalized form of Hooke's law is given by

$$\sigma_{ij} = \lambda \epsilon_{kk} \delta_{ij} + 2\mu \epsilon_{ij}, \tag{3.5}$$

where ϵ_{ij} is the strain tensor, related to the displacement u_i by

$$\epsilon_{ij} = \frac{1}{2}(u_{i,j} + u_{j,i}), \tag{3.6}$$

and μ and λ are the Lamé constants. Plugging Eq.(3.6) into Eq.(3.5) and subsequently into Eq.(3.4) leads to Navier's equations of motion

$$\begin{aligned} \mu u_{i,jj} + (\lambda + \mu) u_{j,ji} &= \rho \ddot{u}_i \\ \mu \nabla^2 \mathbf{u} + (\lambda + \mu) \nabla \nabla \cdot \mathbf{u} &= \rho \ddot{\mathbf{u}}. \end{aligned} \tag{3.7}$$

It should be noted that body forces $\mathbf{f}$ are neglected here. Solving Eq.(3.7) is somewhat difficult, because it couples a partial differential equation (PDE). The Helmholtz decomposition

$$\mathbf{u} = \nabla \varphi + \nabla \times \psi, \tag{3.8}$$

provides a convenient way to uncouple these equations. Eq.(3.8) represents the three components of displacement u with the four functions φ, ψ_1, ψ_2, and ψ_3. To guarantee the uniqueness of the solution, an additional constraint

$$\nabla \cdot \psi = 0 \tag{3.9}$$

is introduced. Substitution of Eq.(3.8) into Eq.(3.7) leads to the two uncoupled wave equations expressed in terms of the displacement potentials φ and ψ

$$\nabla^2 \varphi = \frac{1}{{c_L}^2} \ddot{\varphi}, \quad \nabla^2 \psi = \frac{1}{{c_T}^2} \ddot{\psi}, \tag{3.10}$$

whereas c_L represents the wave speed of the longitudinal wave (P-wave) and c_T the wave speed of the vertically and horizontally polarized shear waves (SV and SH waves),

$${c_L}^2 = \frac{\lambda + 2\mu}{\rho}, \quad {c_T}^2 = \frac{\mu}{\rho} \tag{3.11}$$

It always the case that $c_L > c_T$. Both wave speeds are expressed in terms of material properties density ρ and the Lamé constants μ and λ. The Lamé constants define the elastic behavior of isotropic solid. For convenience, however, the two constants are often expressed in terms of material properties Young's modulus E and Poisson's ratio ν as

$$\lambda = \frac{E\nu}{(1+\nu)(1-2\nu)}, \tag{3.12}$$

$$\mu = \frac{E}{2(1+\nu)}. \tag{3.13}$$

Using these relations, the two wave speeds can also be written as

$${c_L}^2 = \frac{E}{\rho} \cdot \frac{1-\mu}{(1+\mu)(1-2\mu)}, \quad {c_T}^2 = \frac{E}{\rho} \cdot \frac{1}{2(1+\mu)} \tag{3.14}$$

3.2 Geometrical acoustics in homogeneous solids

It has been shown in the earlier section that two types of elastic wave maybe propagated through solids. It is explained in many comprehensive books on wave propagation theory that, when a wave of either type impinges on a boundary between the two media, both reflection and refraction take place. As an example one shall first look what happens when longitudinal and transverse plane waves are reflected at a stress free boundary.

3.2.1 Plane wave phenomena

Assuming a wave with constant properties (ϵ, σ, u) on a plane perpendicular to its direction of propagation $\mathbf{p}$. Eq.(3.15) shows the mathematical representation of a plane wave,

$$\mathbf{u} = f(x \cdot \mathbf{p} - ct)\mathbf{d} \tag{3.15}$$

where $\mathbf{d}$ is the unit vector defining the direction of particle motion, and c is either the longitudinal wave speed c_L or the transverse wave speed c_T. By substituting Eq.(3.15) into Eq.(3.7), one obtains

$$(\mu - \rho c^2)\mathbf{d} + (\lambda + \mu)(\mathbf{p} \cdot \mathbf{d})\mathbf{p} = 0. \tag{3.16}$$

Since $\mathbf{p}$ are the two different unit vectors, it can immediately be seen that the two possible solutions that form the basis of wave propagation are either $\mathbf{d} = \pm\mathbf{p}$ or $\mathbf{p} \cdot \mathbf{d} = 0$:

1) $\mathbf{d} = \pm\mathbf{p}$ leads to $\mathbf{p} \cdot \mathbf{d} = \pm 1$ and yields with Eq.(3.16), $c = c_L$ (see Eq.3.14). Since $\mathbf{d}$ and $\mathbf{p}$ are linearly dependent, this represents a particle movement in the direction of propagation - a longitudinal or P-wave.

2) $\mathbf{p} \cdot \mathbf{d} = 0$ yields with Eq.(3.16), $c = c_T$ (see Eq.3.14). Now the direction of motion is normal to the direction of propagation, and the wave is called

a transverse wave. If a two dimensional plane of propagation is considered (for example, the (x_1, x_2) plane), a wave with an in-plane displacement (in the (x_1, x_2) plane) is called an SV-wave (vertically polarized), while a wave with out-of-plane displacement (in the x_3 direction) is called an SH-wave(horizontally polarized).

In a homogeneous, isotropic material, longitudinal and transverse wave speeds are independent of frequency or they are nondispersive.

3.2.2 Mode conversion

The wave types derived so far propagate independently in an infinite media. As soon as a finite media in the direction of propagation is considered, reflections and coupling will occur. An incident P-wave (or SV-wave) as described previously, is

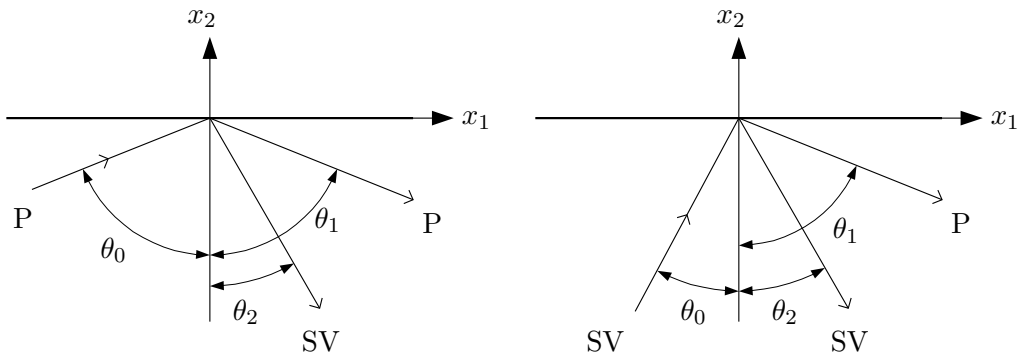

(a) Reflection of a P-wave (b) Reflection of a SV-wave

Figure 3.1: Reflection of waves

reflected at a stress free boundary ($\sigma_{21} = 0$ and $\sigma_{22} = 0$), a wave of each type is reflected. Figure (3.1) shows the reflections of an incident P and SV-wave. The effect of a single incident wave-type producing two different waves (after reflection from a

boundary) is called mode conversion. The displacement field of a harmonic wave in the x_1, x_2 plane (propagating in an infinite media, plane strain case) can be expressed as,

$$\mathbf{u}^{(n)} = A_n \mathbf{d}^{(n)} e^{ik_n(x_1 p_1^{(n)} + x_2 p_2^{(n)} - c_n t)}, \tag{3.17}$$

whereas n denotes the wave (longitudinal or transverse), $k_n = \frac{\omega}{c_n}$ is called the wave number of wave n and the respective wave speeds are c_n. Using these definitions, and noting that the angular frequency ω is the same for the incident and reflected waves, it is possible to determine the relationship between the angle of the incident and the angles of the reflected waves, to obtain non-trivial amplitudes A_n, the angles of incident and reflected waves, θ_0, θ_1, and θ_2 as depicted in Fig.3.1, must satisfy Snell's law:

$$k_0 \sin\theta_0 \;=\; k_1 \sin\theta_1 \;=\; k_2 \sin\theta_2. \tag{3.18}$$

Exceptions of mode conversion are the normal incidence with $\theta_0 = 0$-in this case, the waves are reflected as themselves and if the angle θ_0 is greater than a critical angle,

$$\theta_{cr} = \arcsin \frac{c_T}{c_L}; \tag{3.19}$$

Then only a SV-wave is reflected. The P-wave portion of the reflected signal degenerates into a surface wave (Rayleigh wave), travelling along the surface and exponentially decreasing in amplitude with increasing depth.

3.3 Attenuation

3.3.1 Definition

Consider a plane stress wave that is attenuated as it propagates through the medium:

$$\sigma(x,t) = \sigma_0 e^{i(\omega t - kx)} \tag{3.20}$$

where ω denotes the angular frequency and k is called the propagation vector. As expression for an attenuated wave is obtained by assuming that the wave number k or the velocity c is complex. Take the wave number to be complex: $k = k_1 - i\alpha$, one obtains the equation of a plane attenuated wave:

$$\sigma(x,t) = \sigma_0 e^{-\alpha x} e^{i(\omega t - k_1 x)} \tag{3.21}$$

The attenuation factor α is thus defined as the imaginary part of the complex wave number and the phase velocity is given by $c = \frac{\omega}{k_1}$. It is known that α causing an exponential decay in pressure amplitude, one can use

$$\sigma(x) = \sigma_0 \cdot e^{-\alpha x} \tag{3.22}$$

to specify the attenuation α which is not dependent on x. Another way of expressing the same thing is to write

$$\log_e \sigma(x) = \log_e \sigma_0 - \alpha x \tag{3.23}$$

Then for two different points x_1 and x_2 where $x_1 < x_2$, the difference of expressions at the two points is

$$\alpha = \frac{1}{x_2 - x_1} \log_e \frac{\sigma(x_1)}{\sigma(x_2)}, \tag{3.24}$$

and, since any ratio of two pressure amplitudes such as $\sigma(x_1)$ and $\sigma(x_2)$ must, in order to be expressed in decibels (dB) or in nepers (Np), be written, respectively, as

$$20 \log_{10} \frac{\sigma(x_1)}{\sigma(x_2)} \text{ dB} \quad \text{or} \quad \log_e \frac{\sigma(x_1)}{\sigma(x_2)} \text{ Np} \tag{3.25}$$

then

$$\alpha = \frac{1}{(x_2 - x_1)} 20 \log_{10} \frac{\sigma(x_1)}{\sigma(x_2)} \text{ dB/unit length}, \tag{3.26}$$

$$\alpha = \frac{1}{(x_2 - x_1)} \log_e \frac{\sigma(x_1)}{\sigma(x_2)} \text{ Np/unit length}, \tag{3.27}$$

$$\alpha \text{ (Np/unit length)} = 8.686 \ \alpha \text{ (dB/unit length)} \tag{3.28}$$

The ratio between pressures $\sigma(x_2)$ and $\sigma(x_1)$ at two different distances, due to the attenuation along the transducer axis, is shown in Fig.3.2 versus path difference $x_2 - x_1$. The coefficients of α vary between 0 and 50 dB/m.

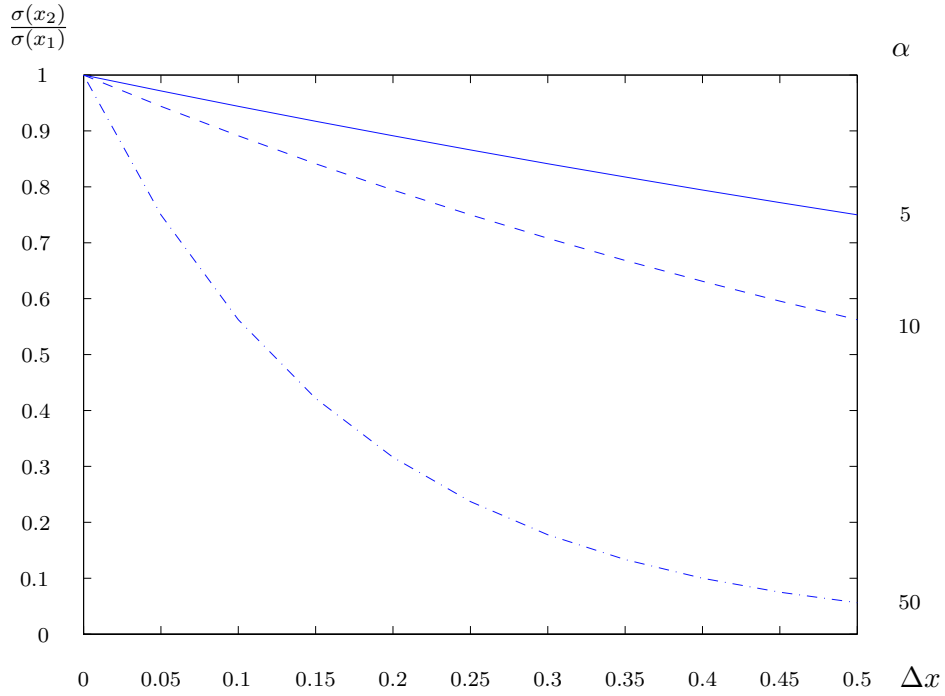

Figure 3.2: Relative pressure $\frac{\sigma(x_2)}{\sigma(x_1)}$ versus path difference Δx [m], due to attenuation α [dB/m]

3.3.2 The cause of attenuation

The cause of total attenuation may be divided into two classes: those "intrinsic" attenuations that are of physical interest, having to do with physical properties of the material, and those apparent or "extrinsic" attenuations that arise as a consequence of the method by which the attenuation measurements are made.

3.3.2.1 Extrinsic attenuation

Extrinsic attenuation can be caused by beamspreading. The pressure wave field emitted from a real vibrating transducer of finite size differs from a plane wave behavior. The ratio between transducer diameter d and wavelength λ affects the radiation pattern [43]. Figure 3.3 shows a polar representation of the directivity function at three different transducer diameter-to wavelength ratios. The figure shows that increasing the diameter of the transducer makes the wave field less divergent. The divergence of the transmitted beam causes the energy to drop.

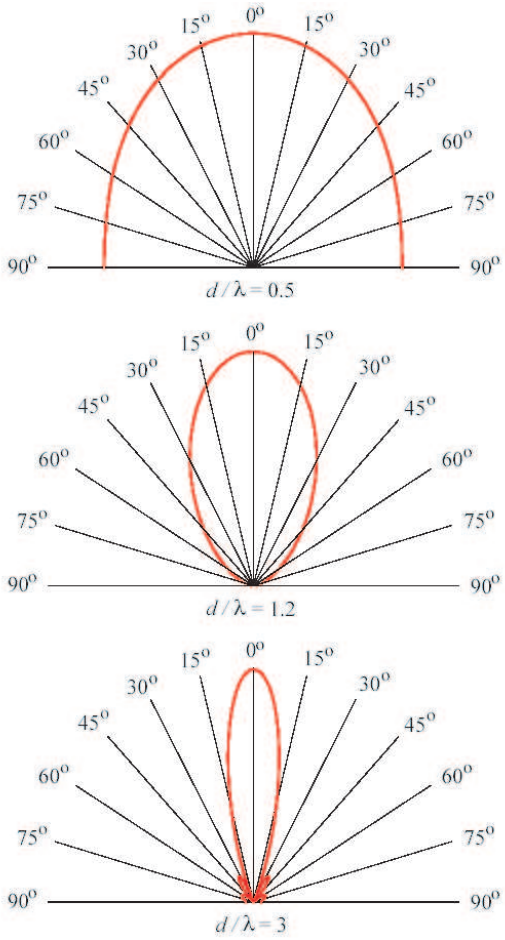

Figure 3.3: Pressure wave at different angles, for different ratios between transducer diameter d and wavelength λ

For a circular transducer, the pressure wave reduction at point x along the axis of the transducer due to the beamspreading is described by

$$p(x) = 2p_0 \cdot \sin[\pi \frac{d}{\lambda}(\sqrt{(\frac{1}{2})^2 + (\frac{x}{d})^2}) - \frac{x}{d}] \tag{3.29}$$

The pressure wave exhibits large variations near the transmitting, in the so called the near-field, as shown in Fig 3.4 for d/λ equal to 3. Further away from the transducer surface, in the so called far-field, the pressure wave reduction follows a decay approximation inversely related to the distance. The actual pressure is also related to the area of the transducer. The approximated pressure wave in the far field is expressed as

$$p(x) = p_0 \cdot \frac{\pi}{(x/d)} \cdot \frac{d}{\lambda} \cdot \frac{1}{4} \tag{3.30}$$

Increasing d/λ decreases the angle of divergence and thereby the beam spreading effect. This implies that larger transducer sizes and higher frequencies both give a less divergent beam. The absolute values of the ratio between distance and diameter are shown in Fig.3.4, for different ratios between transducer diameter and wavelength.

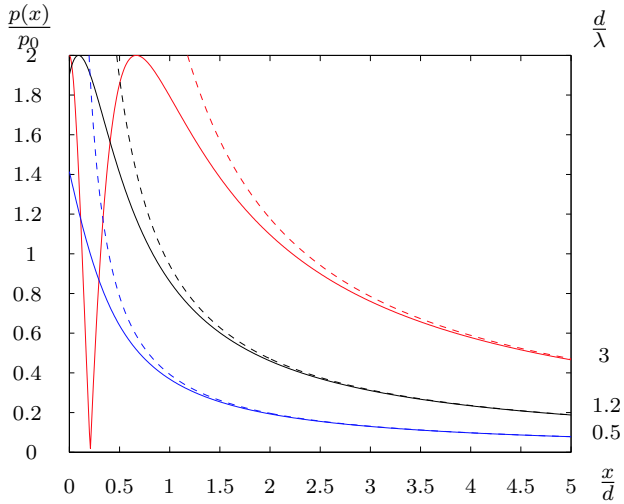

Figure 3.4: The absolute value of the relative pressure wave $\frac{p(x)}{p_0}$ due to beamspreading, versus distance related to transducer diameter $\frac{x}{d}$ for various diameter to wavelength relations $\frac{d}{\lambda}$. Approximated relative pressure, dotted lines

Diffraction correction It is shown earlier that the beam diverges and the wave front is neither plane nor spherical. This effect is what so called a "diffraction effect". Very large errors in attenuation measurement can occur from the diffraction effect. It is necessary that this effect must be separated from the total measured attenuation in order to find the attenuation of physical interest for material characterization purposes. Calculation of corrections from the diffraction effects can be done either be experimentally measured for any given transducer or analytically calculated for many simple transducer shapes.

When the transmitting and receiving transducers are circular with radius a, the diffraction can be corrected from the Lommel expression given by Rogers and Van Buren [44]:

$$D_L = 1 - e^{-i2\pi/s}[J_0(2\pi/s) + iJ_1(2\pi/s)], \tag{3.31}$$

The magnitude of D_L calculated from Eq.(3.31) is plotted and shown in Fig. 3.5 with solid line, as a function of s. Noting from Eq.3.31 that s is the normalized distance $x/\frac{a^2}{\lambda}$ which is a function of some distance x away from the transducer over the near/far field transition distance $\frac{a^2}{\lambda}$. The transducer radius is denoted as a and λ is the propagation wavelength in the medium. J_0 and J_1 are Bessel functions. In the far field, the diffraction correction approaches

$$\lim_{s\to\infty} D_L = \frac{i\pi}{s} \tag{3.32}$$

which is also plotted in Fig. 3.5 with dotted line. Roughly, one can assume that there is no beam spreading at all up to the near/far field transition and that the beam diverges like a spherical wave beyond this point. Figure 3.6 shows the Lommel diffraction correction versus frequency for a circular transducer of 8 mm-diameter and x = 25 mm separation in cement paste.

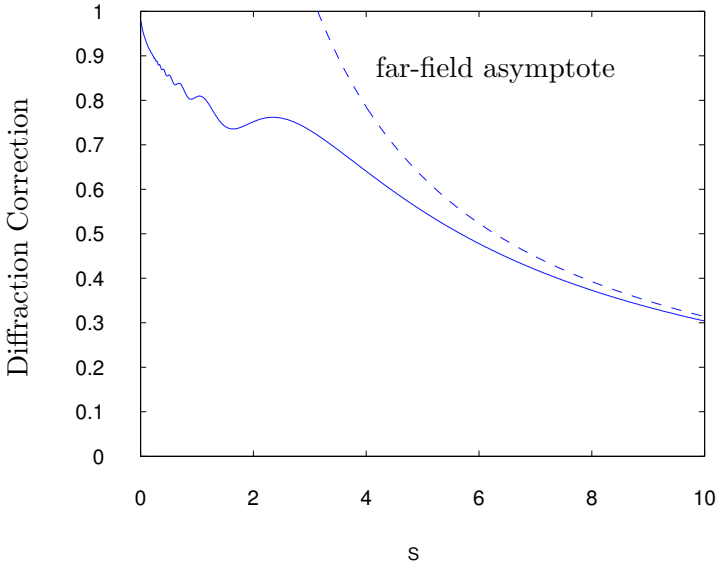

Figure 3.5: Magnitude of the Lommel diffraction correction for a circular transducer

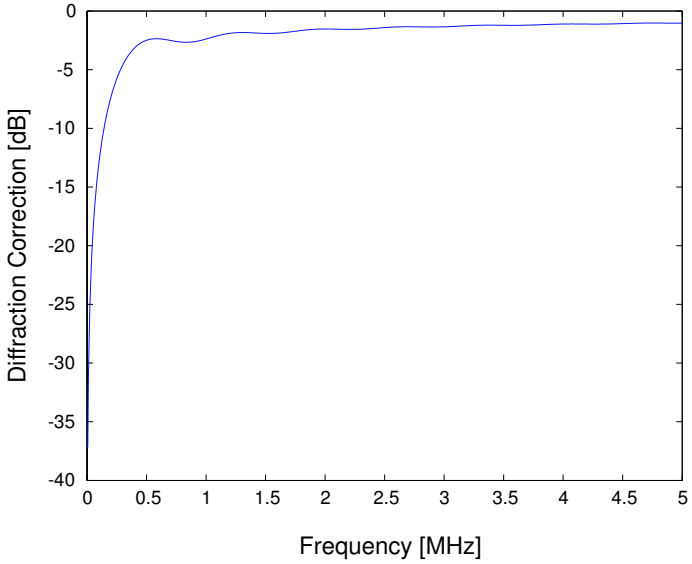

Figure 3.6: The Lommel diffraction correction vs. frequency for a circular piston radiator of 8 mm-diameter and x = 25 mm separation in cement paste

3.3.2.2 Intrinsic attenuation

The group of losses of physical interest is divided into two main types: material absorption and scattering effect.

Material absorption, α_a: Material absorption causes dissipation of the stress wave energy. It occurs if the material stress and strain are not single-valued functions of one another for a complete cycle of oscillatory stress. The lack of such single-valued behavior arises where time derivatives of stress or strain are present in the equation relating stress and strain. Even when the stress-strain part of the equation remains piecewise linear, the presence of time derivatives assures dissipation. The result is the hysteresis effect – the strain can not keep up with the alternation in stress. And if the strain is not homogeneous, as for example, longitudinal ultrasonic wave is propagated through metals [45], temperature gradients will be set up between regions of compression and of rarefaction. This will lead to a flow of heat, accompanied by a production of entropy and thereby causing irreversibly energy lost in the ultrasonic wave which will result in an attenuation of the pressure wave amplitude. This type of attenuation is reportedly proportional to the square of frequency.

In some polymers, in the glassy state (above the rubber-glass transition), an absorption has been observed with attenuation coefficient, α proportional to the first power of the frequency [46]. This type of absorption is called hysteresis absorption. Hysteresis absorption has also been observed in biological tissues [47]. A quantitative model was proposed for hysteresis absorption in polymers [46]. However, so far no quantitative model for hysteresis has been developed for any material in which this type of loss has been observed. It should be noted that

hysteresis loss can be accounted for formally by assuming a relaxation mechanism with a very broad distribution of relaxation times extending over many decades of frequency [47].

Scattering, α_s: Scattering, which is the other part of the intrinsic attenuation, arises at the boundaries between materials, grains, or inclusions with different elastic properties. These differences are associated with the grain structure, multiple phases, precipitates, crystal defects from dislocations, etc. In short, any inhomogeneity can serve as scatterer. The general problem of expressing attenuation due to scattering through a medium containing scatterers with given size, shape, material property, and density of scatterers dates further back. When the scatterer density is low, the loss caused by a single scatterer is not affected by the presence of other scatterers and the total loss can be calculated from the so called *single scattering theory.* The scattering from an individual

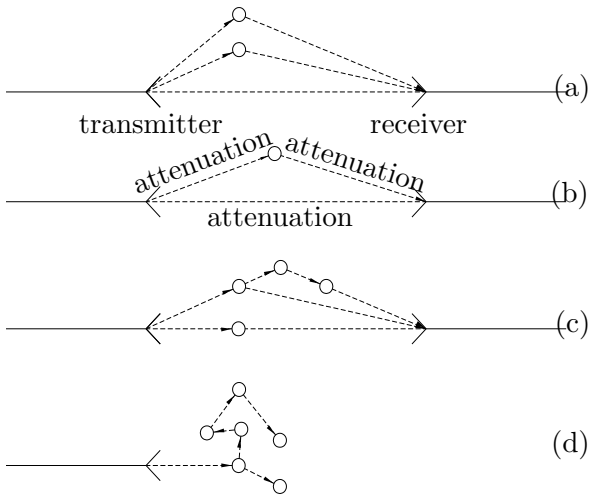

Figure 3.7: Scattering models (a) single scattering, (b) first order multiple scattering, (c) multiple scattering, and (d) diffusion approximation

can be treated independently [42], as anticipated in Fig. 3.7(a) and the combined scattering attenuating effect is simply the arithmetic addition of their individual contributions. When propagating waves experience many scattering events (high scatterer density), as one shown Fig 3.7(b)-(d), multiple scattering effects are present and the problem for obtaining scattering attenuation is much more complicated. The approach to multiple scattering involves methods primarily due to Foldy [48], Waterman and Truell [49], who utilized the technique called configuration average and by Dainty and Toksoz [50], who modelled the scattered wavefield energy by a diffusion approximation (or *diffusive wave theory*).

Three scattering regions are usually defined on the basis of (single, or self similar) scatterer size a to the wavelength λ ratios [5] and the functional dependence of scattering losses on frequency can be often established without really solving the wave equation.

$$\begin{aligned} \alpha_s &\sim f^4 \cdot a^3 \quad - \text{ Rayleigh Domain}, 2\pi a/\lambda << 1 \\ \alpha_s &\sim f^2 \cdot a^3 \quad - \text{ Stochastic Domain}, 2\pi a/\lambda \approx 1 \\ \alpha_s &\sim a^{-1} \quad - \text{ Geometric Domain}, 2\pi a/\lambda > 1 \end{aligned} \tag{3.33}$$

This thesis will use the experimental measured intrinsic attenuation to characterize the microstructure of heterogeneous cement paste.

CHAPTER 4

Experimental and signal analysis

Ultrasonic attenuation measurements require either fully automated apparatuses picking out the required information from the measured signal in real time or equipments that store the entire data recorded for further signal processing and for the determination of material attenuation. Basic components of ultrasonic measurement and experimental systems typically used in this thesis for the attenuation measurement are discussed.

4.1 Equipment

Pulser-receivers generate high energy, high gain broadband performance necessary for high frequency investigation of attenuating materials. They are used in conjunction with transducers and oscilloscope. The pulser section produces an electrical pulse to excite crystal in a piezoelectric transducer, which then emits an ultrasonic pulse. In through transmission applications, this pulse travels through the test material to a second transducer acting as a receiver and is converted into an electrical signal which is then amplified and conditioned by the receiver section and made available for further analysis.

Piezoelectric transducers emit and receive ultrasonic waves using principle called the piezoelectric (pressure electricity) effect, the phenomenon that certain crystals for example quartz change their physical dimensions when subjected to

an electric field, and vice versa [51]. The rapid shape changes or vibrations of the crystals produce mechanical pressure wave that travel outward. Conversely, when pressure waves hit the crystals, they emit electrical current therefore the same crystals can be used to send and receive pressure waves.

Oscilloscopes are graphical displayed devices. In most applications, digital oscilloscopes are used to show how signals change over time: the vertical (Y) axis represents voltage and the horizontal (X) axis represents time. To capture signals over time, the analog-to-digital converter (ADC) unit samples the voltage signal travels through the probe which is attached to the ADC unit at discrete points and converts the signal's voltage at these points to digital values called "sample points". The horizontal systems's sample clock determines how often the ADC takes a sample. The rate at which the clock "ticks" is called the "sample rate" and is measured in "samples per second". The faster the oscilloscope can sample, the more accurately it can represent fine details in a fast signal. The sample points from the ADC are stored in memory as "waveform points" in "bits". Together, the waveform points make up one "waveform record". The number of waveform points used to make a waveform record is called the "recorded length". The "trigger" system determines the start and stop points of the record. Depending on the capabilities of the oscilloscope, additional processing of the sample points and pre-trigger can also take place. This to enhance the display and to allow users to see events before the trigger point. More information about oscilloscopes can be found the book by Middleton [52].

Passive probes are made of resistors, capacitors, cables and wires that add resistive, capacitive, and inductive in order to limits the voltage or loading before damaging oscilloscopes. A general rule of thumb is to select passive probes with a resistance greater than 10 times the oscilloscopes resistance. This will also

result in less than 10% reduction in measured voltage.

4.2 Attenuation measurement system

There are various measurement systems to acquire signals for measuring attenuation and different methods for quantitatively estimating the attenuation coefficient. In this thesis, two are chosen and they are coherent and diffuse measurement systems. All the equipments mentioned in the previous section are used in these two systems for the measuring of attenuation.

4.2.1 Coherent measurement system

A schematic diagram of the coherent measurement system for the attenuation measurement is shown in Fig. 4.1(a). Using a matched pair of broadband ultrasonic transducers, an ultrasonic (longitudinal or transverse wave) pulse is sent into the specimen from the transmitting transducer (labelled as T), and the "coherent" $S_1(t)$ and $S_2(t)$ pulses that propagates through one and three thicknesses between receiving transducer (labelled as R located on axis on the opposite faces of the specimen) are acquired, transmitted and stored digitally in the personal computer via GPIB (general purpose interface bus) for further signal processing. Figure 4.1(b) shows a typical time coherent signal $S_1(t)$ and $S_2(t)$ obtained from the experiment. It is the changes in phase and amplitude of the frequency spectra of these coherent waves[1] that can be used to measure phase velocity and ultrasonic intrinsic attenuation.

[1] waves that theirs behavior at various times/spaces are linked in a deterministic way

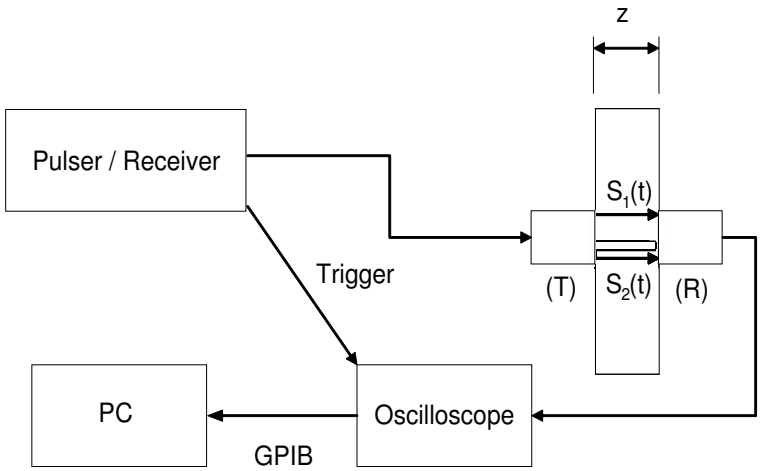

(a)

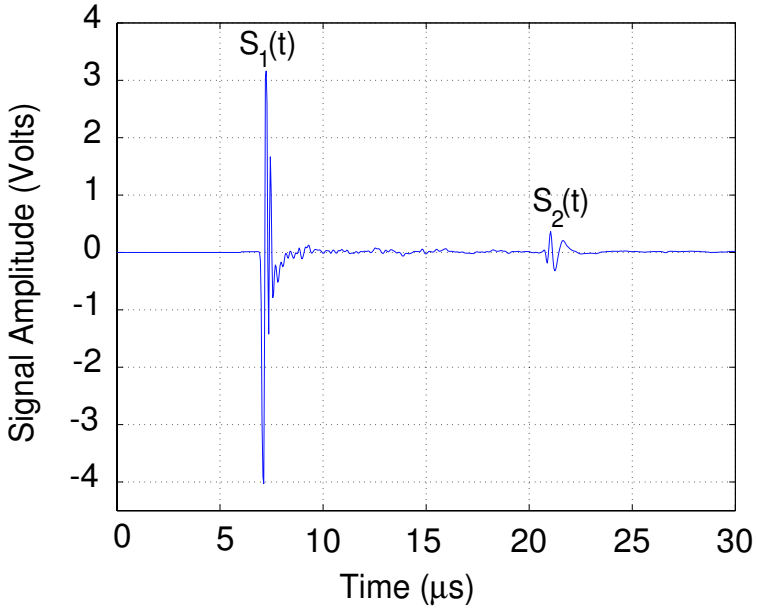

(b)

Figure 4.1: (a) a schematic diagram of the coherent measurement system (b) a typical time coherent signal obtained from the coherent measurement

4.2.2 Diffuse measurement

Attenuation measurements using coherent measurement system measures the effect of both material absorption and scattering as well as extrinsic attenuation. In contrast, diffuse measurement can naturally separate the absorption and scattering contributions, and have shown to be effective in the measuring of the intrinsic absorption of a material.

Figure 4.2(a) shows the experimental setup for the diffuse ultrasound field measurement system. The system in general consists of a transmitting broadband transducer (labelled as T) located at the geometric center of the specimen and a broadband pad receiving transducer located on the opposite side of the specimen (labelled as R). Noting that the pad, a millimeter square plastic foil, is carefully attached to a receiving transducer to enable a point like detector. This point-like detection is critical because the diffuse ultrasound field[2] cancels itself out over a large transducer surface. The impulse response of the tested specimen is measured off epicenter, on the opposite side (with respect to the source), at a location where only diffuse field response is measured. The acquired signal (Fig. 4.2(b)) is then amplified and transmitted to the personal computer via GPIB for further signal analysis.

4.3 Waveform acquisition

4.3.1 Sampling rate and record length

In data acquisition systems, digitization is performed by an analog-to-digital converter (ADC). An ADC converts the analog signal from a transducer into a digital signal

[2]generated by a wide band source transducer in specimen enclosure occur at late times. The field is postulated to be completely incoherent and uniformly distributed in space after many transits across the specimen

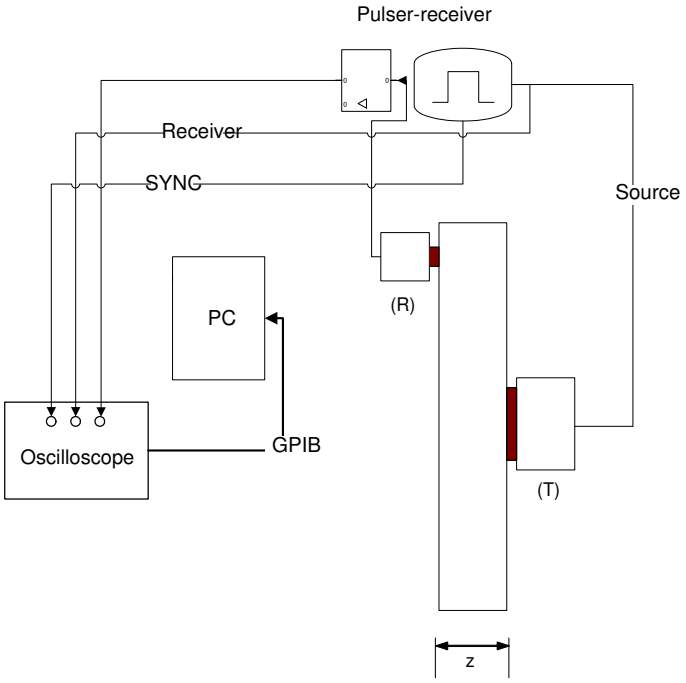

(a)

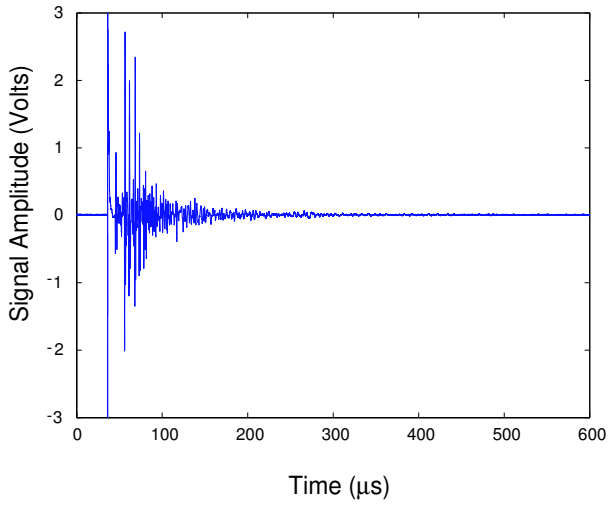

(b)

Figure 4.2: (a) a schematic diagram of the diffuse measurement system (b) a typical time diffuse signal obtained from the diffuse measurement

that can be read by the acquisition system's computer. Digital sampling theory states that, at a minimum, a signal must be sampled at a rate equal to twice of its highest frequency. In other words, there must be at least two samples for every shortest cycle of the signal. This is done to prevent frequency aliasing [53]. At present, all measurements (both coherent and diffuse) presented are obtained with oscilloscopes with special memory extension which allows a measured signal to sample up to 60000 points with the maximum sampling rate of 50 mega samples per second.

4.3.2 Signal averaging

Experimental measured signals are never perfect, even with sophisticated equipments. Noise or unpredicted variations in the measured signals occur from moment to moment or from measurement to measurement. Signal averaging is a technique commonly employed to improving signals. Signal averaging exploits the fact that the desired signal is coherently summed. By contrast, any source of noise that is incoherent with respect to the well-defined trigger signal will diminish in amplitude with successive averaging operations. Thus signal averaging can be used to reveal signals that are buried in the background noise and to increase signal-to-noise ratios from below unity to more acceptable levels if the signal can be measured more than once. More details on how to calculate the decrease of the noise power level by the averaging process should refer to [53]. All measurements presented in this thesis are obtained by averaging over 500 individual a well-defined trigger signal during the acquisition with the oscilloscope.

4.4 Signal processing techniques

An informative way of quantifying attenuation is to determine the frequency dependent attenuation coefficient; The approach analyzes the acquired signal in the

frequency domain. This is accomplished by removing the DC offset, applying an appropriate window to capture the signal portion of interest, and then transforming this waveform into the frequency domain using the discrete or fast fourier transform. The purpose of this section is to give a short overview of the signal processing techniques used in this thesis.

4.4.1 The Discrete Fourier Transform (DFT)

A digital signal of finite duration can be specified in the time domain as a sequence of N scaled impulses occurring at regular sampling instants. Each impulse taking on the amplitude of the signal at that instant, The same signal may also be described as a combination of N complex sinusoidal components, each of a given frequency and phase, and each being a harmonic of the sampling rate/N. This representation, called a frequency domain representation and may be obtained from the time-domain form through the use of the "Discrete Fourier Transform (Fourier transforms in terms of discrete) or DFT". The time domain form and the frequency domain form are simply different way of representing the same digital signal, one is chosen over the other simply in terms of utility for a given purpose. The Discrete Fourier Transform and its pair are defined as:

$$V(f_n) = \triangle t \sum_{j=1}^{N} v(t_j) \exp[\ 2\pi i(j-1)(n-1)/N] \quad (n = 1, 2, ..., N) \tag{4.1}$$

$$v(t_k) = \frac{1}{N\triangle t} \sum_{n=1}^{N} V(f_n) \exp[\ -2\pi i(n-1)(k-1)/N] \quad (k = 1, 2, ..., N)$$

where $v(t_k)$ and $V(f_k)$ are values of a time signal and its Fourier transform at discrete frequency and time values, respectively, $\triangle t = t_{k+1} - t_k$ is the sampling time interval, and N is the total number of sampled points.

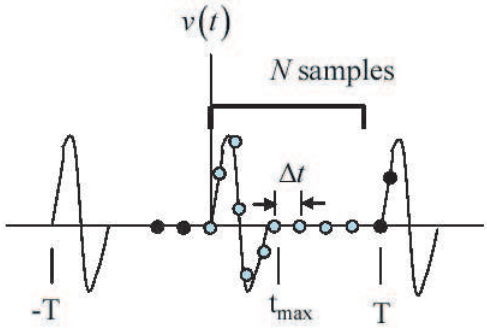

Figure 4.3: A sampled periodic time signal showing N sampled values used in the DFT (light circles) and other sampled values (dark circles). The sampling interval is t, the time t_{max} is the time at which the transient signal ends and the time $T = N\triangle t$ is the period

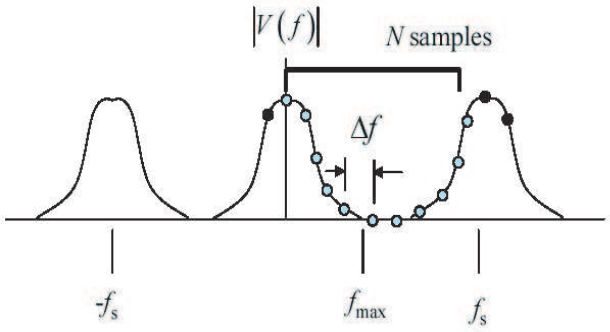

Figure 4.4: The magnitude of a sampled periodic frequency domain function showing the N sampled values. The frequency sampling interval is $\triangle f = \frac{1}{T}$, the frequency f_{max} is the maximum frequency contained in the time signal and the sampling frequency $f_s = \frac{1}{\triangle t}$

The DFT and its pair are usually periodic functions. For example, the first sampled time signal value, $v(t_1)$, is the value sampled at $t = 0$. There are N samples values from $t = 0$ to $t = (N-1)\triangle t$. The sampled value $v(t_{N+1}) = v(N\triangle t)$, however, is the same as the value at time $t = 0$ and subsequent samples also repeat previous values. As Fig. 4.3. shows the sampled time function is periodic with period $T = N\triangle t$. Similarly, in the frequency domain the first sampled value, $V(f_1)$, is the frequency component for $f = 0$ to $f = (N-1)\triangle f$, where $\triangle f = 1/T$. The sampled

value $V(f_{N+1}) = V(N\triangle t)$, is again the D.C. value. The frequency domain function is also periodic with period $f_s = 1/\triangle t$, where f_s is the sampling frequency (see Fig. 4.4).

As long as the original time domain is shorter than the sampling period, T, and the sampling frequency is sufficiently high to capture all the significant components in the signal. It can be seen from Fig. 4.4 that the frequency spectrum of a real time signal must contain both negative as well as positive frequency components, Fig. 4.4 shows that unless the sampling frequency f_s is at least $2f_{max}$, the highest frequency contained in the signal, then the positive and negative frequency components will overlap. To prevent this phenomenon, which is called "aliasing", one must therefore choose a high enough sampling frequency. This requirement is what called the Nyquist criterion, which is the sampling frequency $f_s = 1/\triangle t$, must be at least twice the maximum significant frequency f_{max}, contained in the time signal being sampled.

To implement the DFT efficiently, one uses Fast Fourier Transform (FFT) algorithms, which are readily available in Matlab. Many books [53– 54] have been written on FFTs if one interested in the details of those algortithms. To perform these discrete transforms in MATLAB®, one can use built in functions fft and ifft, which are defined such that the signs are exchanged in the exponentials appearing in Eq. 4.1 and the Matlab functions do not include the sampling time constant $\triangle t$ or N appearing in the coefficients of Eq. 4.1. The most common use of the FFT is to compute the magnitude—the graphical representation of $|V(f)|$ against frequency and phase spectrum—the graphical representation of arg $V(f)$ against frequency, of an acquired time signal as might be obtained from the experiments.

4.4.2 Windowing

One of the thing that was mentioned in DFT section is that the sampled signal becomes periodic. If the signal sequence finishes on a whole number of periods then a discontinuity will not occur. If this is not the case, the signal value (in time) suddenly jumps. The input sequence that the DFT sees for a sequence consisting of one and half periods of a signal and this is demonstrated in Fig.4.5 for a regular sine wave. A discontinuity in time results in what so called the spectral leakage in the DFT [53].

To ensure that signal sequence finishes (or at least closer to) on a whole number of periods. One can simply truncate a signal in the time domain and that can be done by the use of windowing. The main characteristics of windows are given by the main lobe width and the relative peak side lobe amplitude. The two properties together with the position of zeros and the amplitude decay in the frequency domain are relevant to for where leakage can occur. Some common window functions and their properties are available in [53]. In this thesis, only hanning/hamming window such as one shown in Fig. 4.6 will be used. As demonstrated in Fig. 4.6, this window function has a broader and deeper main lobe, which means that more of the energy is in the main lobe, causing less leakage and therefore a better function for signal processing.

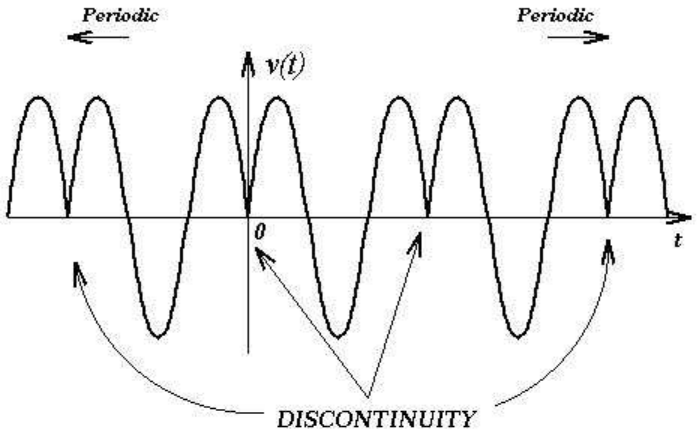

Figure 4.5: Spectral leakage in the DFT

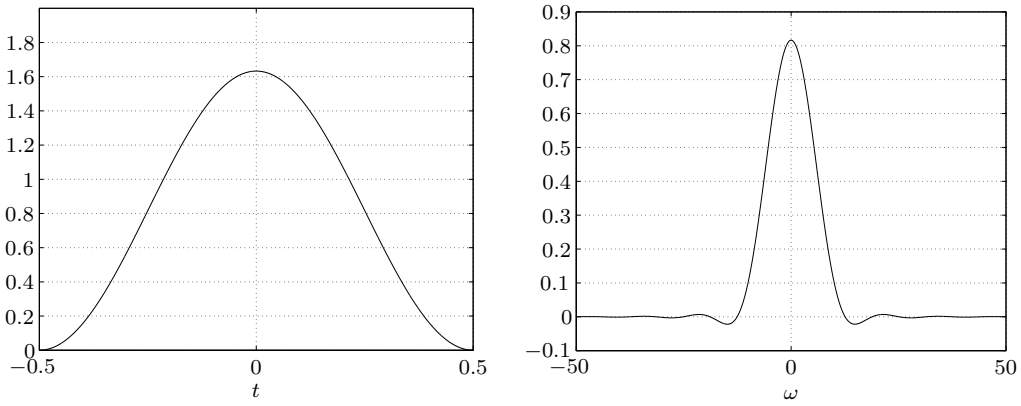

(a) normalized Hanning window

(b) Fourier transform of Hanning window

Figure 4.6: Hanning window

CHAPTER 5

Theoretical model of attenuation of coherent ultrasonic signals in entrained air hardened cement paste combining scattering and absorption losses

The passage of ultrasound waves through cement-based materials exhibit a high degree of material attenuation losses (absorption and scattering). In this chapter, the collective scattering and absorption attenuation of ultrasound interaction with hardened cement paste that contains entrained air voids for protection against damage during freeze-thaw cycles is studied. An estimated of the effects can be obtained using independent single scattering theory (following [29]). The resulting attenuation characteristics are illustrated numerically. These results are discussed in comparison with experimental data of longitudinal wave attenuation in the hardened cement paste containing a low volume fraction of entrained air voids of less than 10% for a large frequency range of 500 kHz - 5 MHz. The study results serve as proof-of-principle; demonstration examples of applicability of using ultrasonic attenuation measurement to characterize microstructure of cement-based materials. A more understanding also leads to a systematic development of inversion technique to recover entrained air void size and volume fraction of entrained air voids from experiments. All that will be presented in great detail in this chapter.

5.1 Morphological-based model of entrained air hardened cement paste

As can be seen through an optical microscope, the entrained air hardened cement paste can be modelled as a composite material consisting of a viscoelastic cement paste matrix and a collection of uniformly mono-sized spherical air voids of radius a and volume fraction ϕ (Fig. 5.1). The total number of entrained air voids in a unit volume of the composite is denoted as n_s and is related to the volume fraction, ϕ, by $\phi = \frac{4}{3}\pi a^3 n_s$.

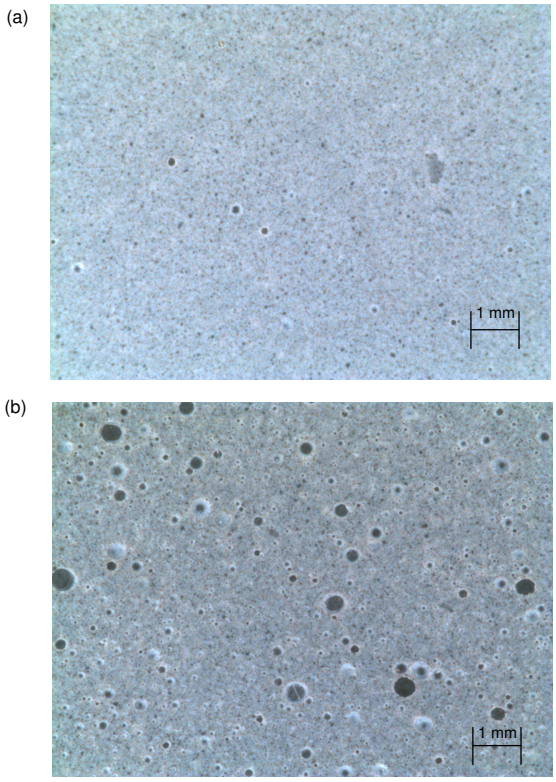

Figure 5.1: (a) A photomicrograph of a typical cross section of entrained air hardened cement paste; (b) morphological-based model of entrained air hardened cement paste

5.2 Estimates for energy losses

Consider a time-harmonic plane wave propagates in a system shown in Fig. 5.1(b). Such a plane wave can, for example, be a Fourier component of the coherent signal. It is hypothesized that the reduction of the energy flow density of the plane wave propagate a unit distance that is assumed small on a macroscopic scale but sufficiently large compared to typical microstructural lengths is due to the energy absorption in the matrix and the wave scattering by the entrained air voids. From this, the spatial decay of the time-averaged energy flow density $< e >$ of the plane waves as it propagates a unit distance in the x_1 direction can be written as [29]

$$\frac{d < e >}{dx_1} = - [< I^{abs} > + < I^{sca} >] \tag{5.1}$$

where $< I^{abs} >$ and $< I^{sca} >$ are the absorption and scattering loss rates in a region V of unit scale and volume as depicted in Fig. 5.2. These losses are estimated using Biwa [29] and Beltzer et al. [55– 56] in the following manner.

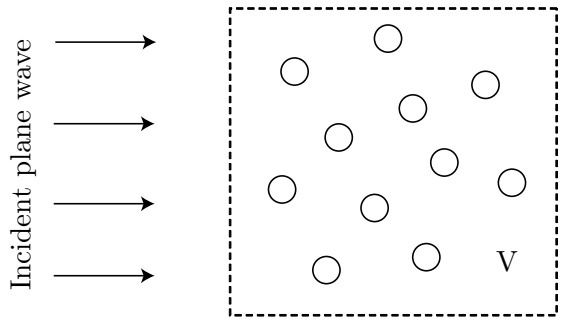

Figure 5.2: A representation volume element for an estimation of energy losses

5.2.1 Scattering loss

To evaluate the scattering loss, it is assumed that no interaction occurs between neighboring voids in the medium. Thus, scattering from an individual void can be

treated independently from one another and the combined effect of multiple voids is simply the arithmetic addition of the individual contributions. With this approximate assumption, a simplified problem is considered for a plane wave scattering by a single inclusion in an infinitely extended viscoelastic matrix as shown in Fig. 5.3.

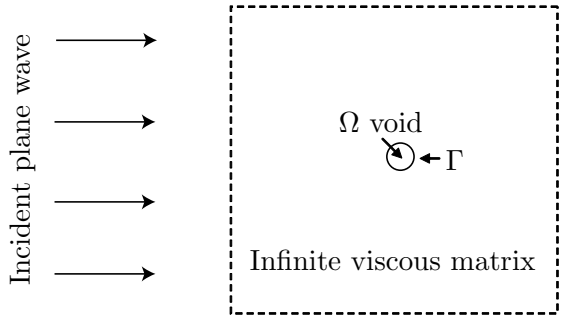

Figure 5.3: A representation volume element for an estimation of scattering loss

The incident plane wave is expressed by ${u_i}^{inc} = \mathrm{Re}[\bar{u}_i e^{i(\omega t - k_1 x_1)}]$ where $k_1 = \frac{\omega}{c_1} - i\alpha_a$ denotes the complex wave number in the viscoelastic matrix, ω the angular frequency. The frequency dependent phase velocity and the attenuation coefficient of the matrix are denoted by $c_1(\omega)$ and $\alpha_a(\omega)$, respectively. The time-averaged energy flow density of the plane wave decays along the x_1 direction having the unit vector denoted by β_i. As a reference, the energy flow density is evaluated at the origin taken at the center of the inclusion. Using the energy flux density vector, or Poynting vector ${P_i}^{inc}$ [55] of the incident wave, the energy flow density is given by

$$< e >_0 \; = \; < e > |_{x=0} \; = \; \frac{1}{T} \int_0^T {P_i}^{inc} \beta_i |_{x=0} \, dt \; = \; \frac{1}{2} \rho_1 \omega |\bar{u}|^2 \mathrm{Re}(k_1 {c_1}^2) \tag{5.2}$$

Introducing the wave fields in and outside Ω. Here Ω denotes the region inside the inclusion and Γ its boundary. The scattering energy loss rate is given by the time-averaged energy flow of the scattered wave integrated over Γ and is written as

$$< I^{sca} >_1 = \; \frac{1}{T} \int_0^T \int_\Gamma {P_i}^{sca} n_i \, dS \, dt \; = \; \gamma^{sca} < e >_0 \tag{5.3}$$

In the above expression, P_i^{sca} is the energy flux density vector of the scattered wave and n_i is the unit normal vector, taken positive outwards from Γ. This loss is normalized by the reference incident energy flow density and the scattering cross section γ^{sca} has been invoked [57]. The suffix 1 stands for the scattering by the single inclusion. To combine the effects of n_s inclusions, the scattering is given in additive manner as

$$< I^{sca} >= n_s < I_1^{sca} >= n_s \gamma^{sca} < e >_0 \tag{5.4}$$

5.2.2 Absorption loss in the matrix

Next, the absorption loss in the matrix is evaluated. Problems like this one are solved using a superposition method. To do so, the energy dissipation of the incident plane wave in a net region occupied by the matrix is considered. It should be noted here that the net region is defined proximity by the area occupied solely by a homogeneous solid, which does not include space taken up by scatterers (see Fig. 5.4).

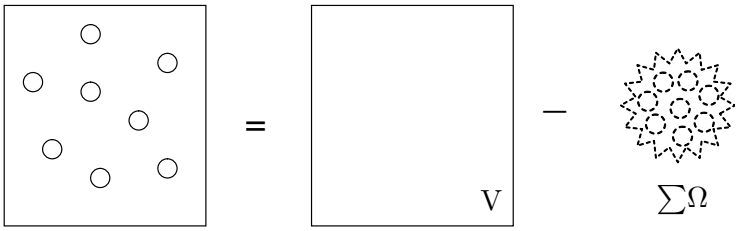

Figure 5.4: A representation volume element for an estimation of absorption loss

This approximation is valuable in situations where it is difficult to solve in an exact manner and $< I^{mat} >$ is given by the time average of the stress work rate integrated over the region $V - \sum \Omega$ as

$$\begin{aligned} < I^{mat} > &= \frac{1}{T|V|} \int_0^T \int_{V-\sum \Omega} \sigma_{ij}^{inc} \dot{\varepsilon}_{ij}^{inc} dV dt \\ &= \frac{1}{T} \int_0^T (- \int_{\partial V} P_i^{inc} {n_i}^V \, dS + n_s \int_\Gamma P_i^{inc} n_i \, dS) \, dt \end{aligned} \tag{5.5}$$

The first integral in the right hand side of Eq. (5.5) can then be carried out by the Gauss theorem to yield

$$-\frac{1}{T|V|}\int_0^T\int_{\partial V} P_i^{inc} n_i{}^V dSdt = -\frac{1}{T|V|}\int_0^T\int_V (-\frac{1}{2}\rho\frac{\partial}{\partial t}(\dot{u}_j^{inc}\dot{u}_j^{inc}) - \sigma_{ij}^{inc}\dot{\varepsilon}_{ij}^{inc})dVdt \tag{5.6}$$

The first term in Eq. (5.6) vanishes when integrated with respect to time. The second term in the integrand can then be evaluated and simplified as

$$\begin{aligned} -\frac{1}{T|V|}\int_0^T\int_V (-\sigma_{ij}^{inc}\dot{\varepsilon}_{ij}^{inc})dVdt &= -\frac{1}{|V|}\frac{i\omega}{4}\int_V(\sigma_{ij}^{inc}\varepsilon_{ij}^{inc^*} - \sigma_{ij}^{inc^*}\varepsilon_{ij}^{inc})dV \\ &= \frac{|\bar{u}|^2}{|V|}\frac{\omega^4\rho_1\alpha_a}{|k_1|^2 c_1}\int_V e^{(-2\alpha_a x_1)}dV \\ &\approx 2\alpha_a < e >_0 \,(\text{ for small } \alpha_a x_1\,) \end{aligned} \tag{5.7}$$

The second integral in Eq. (5.5) is determined by the properties of the matrix as well as inclusion shape. At present, this integral is expressed in the same analogy to Eq. (5.3) as

$$n_s\frac{1}{T}\int_0^T\int_\Gamma P_i^{inc} n_i\, dS\, dt \;=\; -n_s\gamma^{mat} < e >_0, \tag{5.8}$$

then $< I^{mat} >$ is written as

$$< I^{mat} >= 2\alpha_a < e >_0 - n_s\gamma^{mat} < e >_0, \tag{5.9}$$

where an absorption cross section γ^{mat} is introduced [29]. For a spherical inclusion of radius a, the integral shown in Eq. (5.8), which denotes the definition of γ^{mat} can be carried out as

$$\begin{aligned} \gamma^{mat} &\cong 2\alpha_a\int_\Omega e^{(-2\alpha_a\beta_p x_p)}dV, \\ &= 2\alpha_a a^3\int_0^\pi e^{(-2\alpha_a a\cos\theta)}\sin^3\theta\, d\theta \\ &= 2\alpha_a a^3(\frac{\pi}{\alpha_a a})^{\frac{3}{2}} I_{\frac{3}{2}}(2\alpha_a a) \end{aligned} \tag{5.10}$$

The above expression can be derived and simplified similarly to that mentioned before in Eq. (5.7). In the last expression, $I(\cdot)$ is a modified bessel function of the $\frac{3}{2}$ order.

When the argument of the function is small then the function can be approximated as the leading term of its expansion and so γ^{mat} can be written as

$$\gamma^{mat} = 2\alpha_a a^3 (\frac{\pi}{\alpha_a a}) \frac{4}{3\pi^{\frac{1}{2}}} (\alpha_a a)^{\frac{3}{2}} = \frac{8}{3}\pi a^3 \alpha_a, \tag{5.11}$$

which is described as a volume of a single sphere, $\phi = \frac{4}{3}\pi a^3$ multiplied by the factor of $2\alpha_a$. From this the matrix absorption, Eq. (5.9), becomes

$$< I^{mat} >= 2\alpha_a < e >_0 -2\phi\alpha_a < e >_0, \tag{5.12}$$

5.2.3 An approximate expression for the attenuation coefficient

Based on the two considerations discussed above, the energy loss rate of the wave in entrained air hardened cement paste composite is examined. In the present study, no interaction among the neighboring voids is taken into account. Then the scattering loss due to n_s void is given by $< I^{sca} >= n_s < I_1^{sca} >= n_s \gamma^{sca} < e >_0$, and the matrix absorption becomes $< I^{mat} >= 2\alpha_a < e >_0 -2\phi\alpha_a < e >_0$. Identifying $< e >_0$ with $< e >$ and substituting these results into Eq. (5.1)to yield

$$< e > (x_1) \propto e^{-(2\alpha_a - 2\phi\alpha_a + n_s\gamma^{sca})\, x_1} \tag{5.13}$$

Because the energy is a quadratic function of the displacement amplitude, the attenuation coefficient of the system shown in Fig. 5.1(b) is obtained as

$$\alpha = (1-\phi)\alpha_a + \frac{1}{2} n_s \gamma^{sca} \tag{5.14}$$

It should be noted that α has a unit of 1/m or Np/m. The above attenuation expression implies that the presence of the voids of volume fraction ϕ reduces the absorption effect of the matrix to the ratio $(1-\phi)$. This reduction effect has been naturally deduced and observed in experimental studies by Kinra et al. [58]. More over, except for the factor $(1-\phi)$, Eq. 5.14 coincides with the first (single scattering) term of the expression for α derived by Waterman and Truell [49].

5.3 Analysis of longitudinal wave attenuation in the entrained air hardened cement paste

Eq. (5.14) is subsequently applied to the attenuation of longitudinal ultrasonic wave in the entrained air hardened cement paste.

5.3.1 Identification of cement paste matrix material properties

As shown in Eq.(5.14), the analysis of longitudinal wave attenuation in the entrained air hardened cement paste requires data of material properties of the cement paste matrix as well as material properties of entrained air voids. To this purpose, the phase velocities and attenuation coefficients of the cement paste matrix, similar to that used in the entrained air hardened cement paste for which there hardly exist measured values in the literature, are measured for longitudinal as well as transverse waves. Cement paste[1] 10 cm x 20 cm cylindrical specimens were cast from mixing commercially available Type I Portland cement with water at a water-to-cement mass ratio of 0.4 in a Hobart mixer in accordance with ASTM standard. Immediately after the completion of mixing, a vibration table was used to take away entrapped air bubbles from the mix prior to the molding. After the molding cycle, the specimens were covered with plastic caps and kept in moist, sealed plastic containers for 24 hours. After 24 hours, the specimens were demolded and stored in lithium saturated water at 22^{o}C for 27 more days to prevent cracking. At 28 days of age, the specimens were removed from the curing room, and were cut using a diamond saw and polished to provide a 25 mm section parallel finished surface. Those specimens found to be most free of visible cracks are selected for use in for the attenuation measurement (see

[1]see Sec. 5.1 for a qualitative visual description of the specimen

Sec.4.2.1).

Coherent measurements are performed by using contact transducer pairs (1, 2, and 5 MHz nominal frequency, Panametrics Inc.) along with the Panametrics 5072PR pulser-receiver to transmit ultrasonic longitudinal as well as transverse wave pulse into the specimen. The electrical signal is amplified with a maximum of 45 dB, with a power amplifier. The transmitting transducer (T) then converted the electrical signal to a pressure wave. The pressure wave propagated through a specimen and is received by another transducer (R) and converted into the electrical signal. The signal is acquired with a sampling rate of 50 mega samples per second, and with 8-bit resolution into a digital oscilloscope. The amount of noise is suppressed by averaging over 500 signals. The measurement is fully automated by GPIB for transmission of the signal and signal acquisition from the digital oscilloscope to the computer for the post processing.

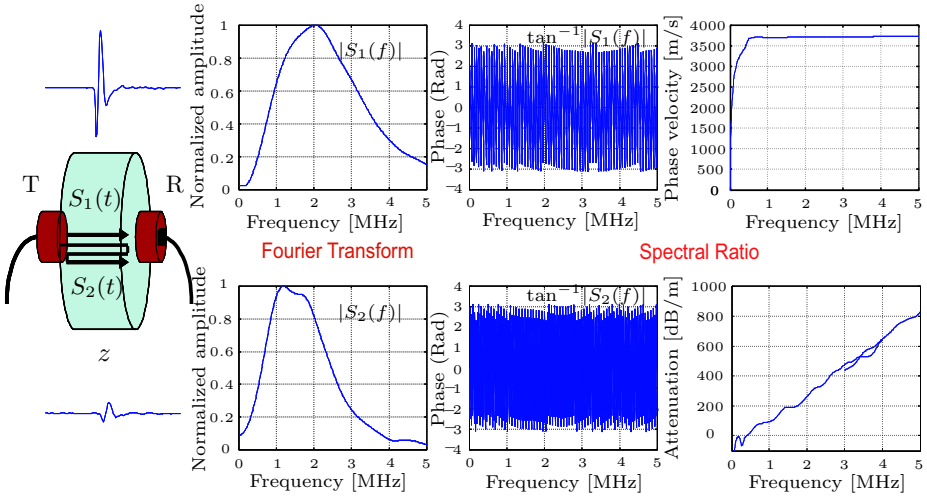

Figure 5.5: Attenuation and phase velocity measurement using spectral ratio technique

In measuring attenuation and phase velocity, spectral ratio analysis [59] is carried out. An analysis involves the extraction from the total signal of two successive coherent signals, $S_1(t)$ and $S_2(t)$, using an appropriate hanning/hamming window. Then, based on Fast Fourier Transforms, the amplitude and phase of the frequency spectra of the $S_1(t)$ and $S_2(t)$ are determined and diffraction corrected. The ratio of the two power spectra allows the calculation of the ultrasonic attenuation. As demonstrated in Fig. 5.5, the first windowed signal $S_1(t)$ propagates through one thickness of the specimen (direct compressional or transverse wave) where as the second one $S_2(t)$ propagates through three thicknesses of the same specimen after reflections on both specimen sides. With a pair of finite circular transducers, the amplitude spectra of the frequency spectra of the two signals are:

$$\begin{aligned} S_1(f) &= D_L(x=z)S_0(f)e^{-\alpha(f)z}e^{i[\omega t-k(f)z+\phi_0]} \\ S_2(f) &= D_L(x=3z)S_0(f)e^{-\alpha(f)3z}e^{i[\omega t-k(f)3z+\phi_0+\delta\phi]} \end{aligned} \tag{5.15}$$

where $\alpha(f)$ denotes the absorption attenuation coefficient, $D_L(s)$ is the diffraction coefficient (see chapter 3, section 3.3.2.1) proposed by Rogers and Van Buren [44] with $s = \frac{2\pi z}{ka^2}$, $k(f) = \frac{2\pi f}{c(f)}$ with c the phase velocity, z is the thickness of the specimen, $S_0(f)$ and $\phi_0(f)$ are the source spectrum and the source phase for $z = 0$, and $\delta\phi$ is the phase shift between the time base of the first and second signal. Thus corresponding expressions for the attenuation and the phase velocity are:

$$\begin{aligned} \alpha(f) &= \frac{1}{2z}[\ln[\frac{S_1(f)}{S_2(f)}] - \ln(\frac{D_L(x=z)}{D_L(x=3z)})] \\ c(f) &= \frac{4\pi f z}{\arg[\frac{S_1(f)}{S_2(f)}] + \delta\phi} \end{aligned} \tag{5.16}$$

where $\arg(\cdot)$ designates the argument of the considered complex number. One can see from Eq.(5.15) and Eq.(5.16) that the effect of geometric divergence (the change in the amplitude due to the diffraction effects) is needed to account for when computing attenuation coefficients. The phase velocity, on the other hand, is not altered by the

geometric divergence.

In the appendix B, experimental results obtained from ultrasonic absorption measurements in methyl methacrylate polymer (Lucite) are presented. The polymer used here was made by the Altuglas Co., Philadelphia, PA under the trade name Plexiglas G and was received in the form of a cast amorphous block of high optical clarity and of thickness 2.54 cm. Its reported specific gravity was 1.1 to 1.2. The measurement gives the values $c_L = 2787m/s$ for the longitudinal wave speed and $\alpha\lambda = 0.045$ Np for the longitudinal absorption attenuation at room temperature. These should be compared with $c_L = 2690m/s$ and $\alpha\lambda = 0.022$ Np measured by Hartmann and Jarzynski [46] and with $c_L = 2750m/s$ and $\alpha\lambda = 0.041$ Np given for clear Plexiglas in a recent book by Cheeke [60]. It can be seen that there is some variability in published values, particularly for attenuation, and these differences may be due to differences in Lucite type. The experimental measurement values reported here are within the range of published values. This establish reliability and accuracy of the experimental setup as well as the spectral ratio technique for attenuation measurements.

As a result of the measurements, it is found that within the range of the frequency bandwidth of interest, the phase velocities of longitudinal and transverse wave are well approximated as frequency-independent constant and the attenuation coefficients as first-order equations of the frequency. The frequency dependence of the phase velocity determined by spectral ratio technique is delineated in Fig. 5.6(a) for longitudinal and transverse waves. Only weak dispersion is observed in the frequency ranges of interest. The attenuation coefficients of cement paste matrix for longitudinal and transverse waves are plotted and shown in Neper/m , as shown in Fig. 5.6(b). It is observed that the attenuation coefficients increase proportionally with frequency.

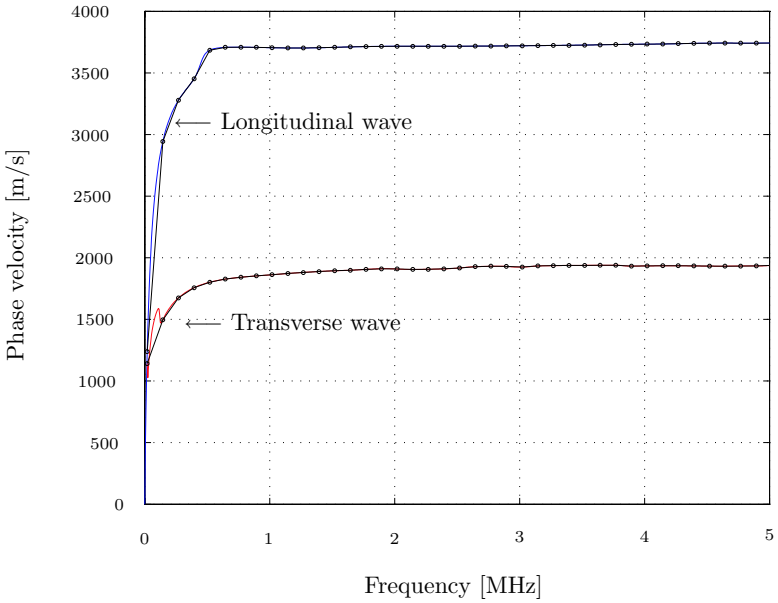

(a) Phase velocities

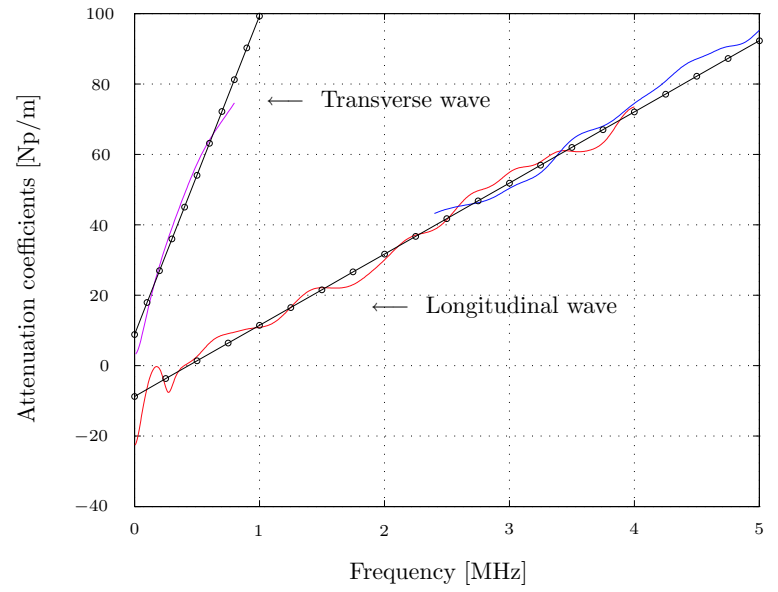

(b) Attenuation coefficients

Figure 5.6: Frequency dependent (a) phase velocities and (b) attenuation coefficients of the longitudinal and transverse waves in cement paste matrix $\frac{w}{c} = 0.4$

Hartmann and Jarzynski [46] found a similar behavior for ultrasonic absorption in some polymers. This behavior is referred to as hysteresis absorption, has also been observed in rocks, biological tissues [47] and recently recognized in cement based materials [21]. Some other material properties of the cement paste extracted from the measurements are summarized in Table 5.1.

Table 5.1: Material properties of cement paste matrix

Property	Symbol	Value
Longitudinal phase velocity	$c_L[\frac{m}{s}]$	3750
Transverse phase velocity	$c_S[\frac{m}{s}]$	1990
Longitudinal attenuation coefficient; $\alpha_L(\omega) = \alpha_{L0} + \frac{\alpha_{La}\omega}{2\pi}$		
	$\alpha_{L0}[\frac{1}{m}]$	-8.50
	$\alpha_{La}[\frac{1}{m \cdot MHz}]$	20.21
Transverse attenuation coefficient; $\alpha_S(\omega) = \alpha_{S0} + \frac{\alpha_{Sa}\omega}{2\pi}$		
	$\alpha_{S0}[\frac{1}{m}]$	8.85
	$\alpha_{Sa}[\frac{1}{m \cdot MHz}]$	90.46
Poisson's ratio	ν	0.26*
Young's modulus	$E[\,\mathrm{GPa}\,]$	19.5*
Density	$\rho[\frac{kg}{m^3}]$	1945
Water to cement mass ratio	$\frac{w}{c}$	0.40

* Values are calculated from phase velocities

5.3.2 Scattering cross section γ^{sca}

The scattering cross section is a quantity which expresses the relationship between the respective energies associated with the incident and scattered waves in a medium containing a scattering obstacle. Thus, the scattering cross section is defined as that area which, if placed into the incident field normal to the direction of the propagation, would intercept an energy flux equal to that of the total scattered field through a closed surface which contains the scattering obstacle, all energies being understood in the sense of the time averages over one cycle. The scattering cross section is thus to be expressed in terms of the incident and scattered waves, the latter of which must be found from the scattered wave field by a single void. Analytical treatments can be found in several books [41], [61]. Here, a full derivation of the cross section using a classical technique introduced earlier by Ying and Truell [57] is to be found in appendix A. This section should contain a brief but adequate description to support further analysis.

For an incident time harmonic $< e^{i\omega t} >$ plane longitudinal wave propagating in x_1 direction, two dimensional complex displacement potentials,Φ and Ψ, satisfy Helmholtz equations, $(\nabla^2 + k^2)\Phi = 0$ and $(\nabla^2 + \kappa^2)\Psi = 0$, with the propagation constants, $k = \frac{\omega}{c_L} - i\alpha_L$ (longitudinal wave) and $\kappa = \frac{\omega}{c_S} - i\alpha_S$ (transverse wave). Using these equations, the problem of a plane longitudinal incident wave encountering a sphere in a viscoelastic solid can be solved using spherical coordinates. The spherical void gives rise to scattered longitudinal and transverse waves outside the sphere (Fig. 5.7). The solution of the wave equations consists of series expansions of spherical Bessel functions and spherical harmonics with two unknown scattering coefficients (A_m and B_m). These coefficients are then determined numerically from the stresses continuity conditions at the void-viscoelastic paste matrix interface (at $r = a$).

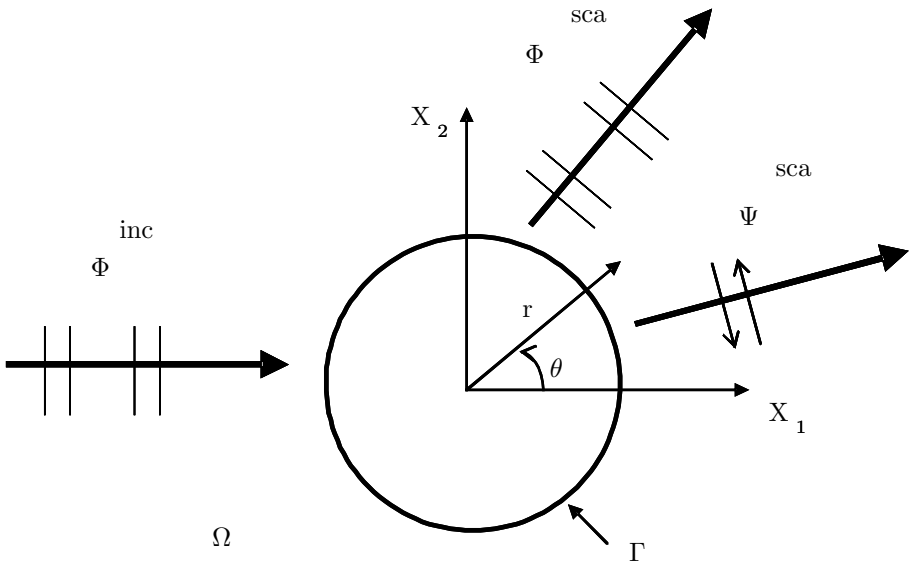

Figure 5.7: Single scattering by a spherical cavity

Using stresses relations described in Appendix A, the results in two simultaneous algebraic equations are sufficient to determine the two coefficients A_m and B_m. In matrix form, these equations are

$$\begin{pmatrix} H_{11} & H_{12} \\ H_{21} & H_{22} \end{pmatrix} \begin{pmatrix} A_m \\ B_m \end{pmatrix} = \frac{-1}{k}(-i)^{m+1}(2m+1) \begin{pmatrix} J_{11} \\ J_{21} \end{pmatrix} \tag{5.17}$$

where

$$\begin{aligned} H_{11} &= -(m^2 - m - \frac{(\kappa a)^2}{2})h_m(ka) - 2(ka)h_{m+1}(ka) \\ H_{12} &= m(m+1)[(m-1)h_m(\kappa a) - (\kappa a)h_{m+1}(\kappa a)] \\ H_{21} &= (m-1)h_m(ka) - (ka)h_{m+1}(ka) \\ H_{22} &= -(m^2 - 1 - \frac{(\kappa a)^2}{2})h_m(\kappa a) - (\kappa a)h_{m+1}(\kappa a) \\ J_{11} &= -(m^2 - m - \frac{(\kappa a)^2}{2})j_m(ka) - 2(ka)j_{m+1}(ka) \\ J_{21} &= (m-1)j_m(ka) - (ka)j_{m+1}(ka) \end{aligned} \tag{5.18}$$

In Eq.(5.18), $j_m(\xi)$ and $h_m(\xi)$ are the spherical Bessel function of the first and the

third kind, respectively. Numerical calculations have been performed for the longitudinal wave scattering by a spherical void in viscoelastic cement paste solid in terms of the normalized wave numbers, ka. After some lengthy manipulations, the scattering cross section is finally related to the finite sums of the expansion coefficients. Using for this the optical theorem [49]:

$$\gamma^{sca} = -\frac{4\pi}{\mathrm{Re}(k)}\,\mathrm{Im}\,(\ -\sum_{m=0} i^m A_m\ ) \tag{5.19}$$

For viscoelastic paste matrix, k is defined earlier and can also be rewritten as $k = \omega(\frac{1}{c_L} - i\frac{\alpha_a}{2\pi f})$. Notice that the latter quantity presented above, $\frac{\alpha_a}{2\pi f}$, is just a slope of the attenuation (in Neper per meter) versus frequency function (in Hz) obtained from attenuation measurement made in specimen consists of cement paste matrix.

For an entrained air hardened cement paste composite, the typical material data for longitudinal and shear motion in cement paste matrix are listed in Table 5.1. Within the model, a spherical entrained air void is also assumed to have a void radius a of 0.3 mm. Using these values the scattering cross section of the spherical entrained air void embedded in the cement paste matrix for the longitudinal wave incidence is computed. Results of the computations are shown in Fig. 5.8. In Fig. 5.8., the scattering cross section is normalized by the planar void area $\frac{\gamma^{sca}}{\pi a^2}$ and is plotted as a function of normalized frequency, $0 \leq ka \leq 5$ which corresponds roughly to $0 \leq f \leq 10$ MHz. One finds from Fig. 5.8. that the scattering effect is relatively small in the low frequency range while it grows substantially and eventually flatten out as the frequency increases. The influence of matrix viscoelasticity on the scattering cross sections of a longitudinal wave is also illustrated in Fig. 5.8. It is seen that viscoelasticity affects mainly the fine structure of the scattering cross section especially in the high frequency $ka > 1$.

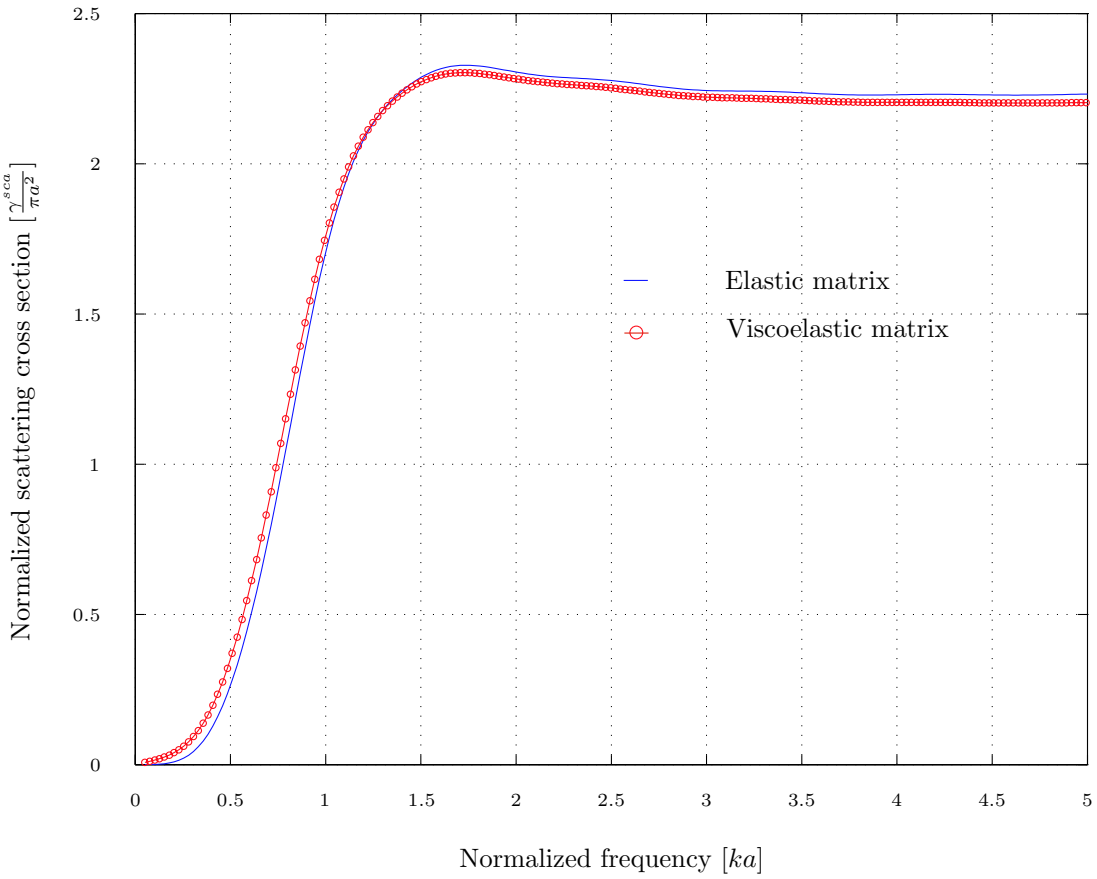

Figure 5.8: Normalized scattering cross section of entrained air hardened cement paste

5.3.3 Attenuation coefficient

The total attenuation coefficient, α, calculated with Eq.(5.14) is shown in Fig. 5.9(a) and Fig. 5.9 (b) for an incident longitudinal wave as a function of frequency, for a number of different void fractions, ϕ, and void radii, a. The experimentally measured absorption attenuation of the cement paste matrix is presented as a dashed line in both figures to indicate the relative contribution of each of the two loss mechanisms — absorption and scattering. These figures show the influence of the void fraction and void radius — the vertical and horizontal shift in the attenuation profile are due to a change in volume fraction and void radius, respectively.

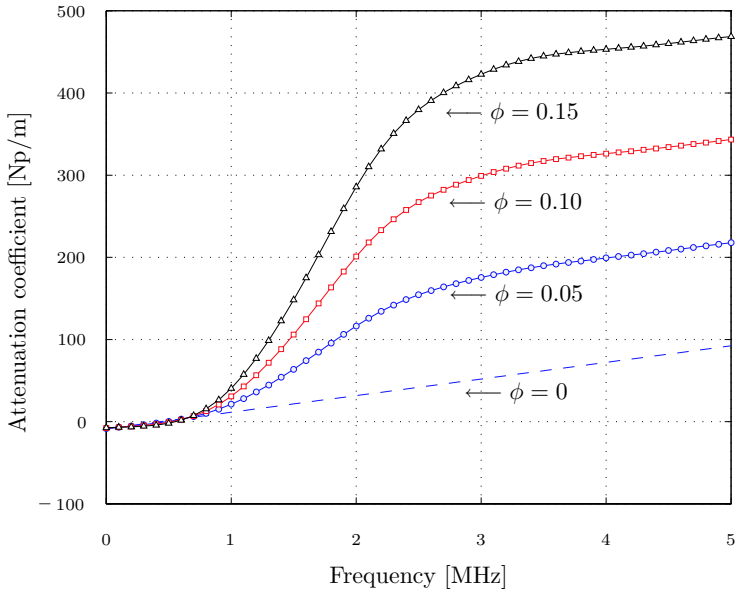

(a)

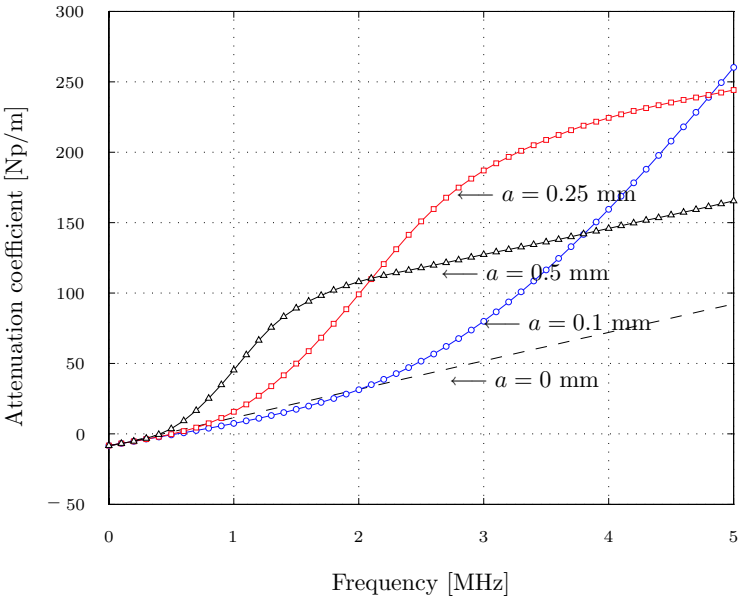

(b)

Figure 5.9: Total attenuation, α versus frequency for (a) different void fractions, ϕ and void radius fixed ($a = 0.3$ mm) and (b) different void radii, a and void fraction fixed ($\phi = 5\%$)

The above results can be used as the "forward problem" for the inversion scheme. It can be seen that the total attenuation is directly related to the entrained air void size and volume through this frequency range, and these figures indicate that it should be possible to extract quantitative information about the entrained air void size and distribution in real entrained air hardened cement paste specimens.

5.4 Experimental coherent measurement procedure and preliminary results

10 cm x 20 cm entrained air hardened cement paste[2] cylindrical specimens were made from mixing commercially available Type I Portland cement with water at a water-to-cement mass ratio of 0.4 in a Hobart mixer. A chemical air-entraining agent (Darex supplied by W.R. Grace) is added at about 0.2 percent of the cement by mass during the process of mixing without adjustment of the total volume to produce entrained air voids in the hardened cement paste specimen. This is similar to procedure by Kalliopi and Phillip [62]. Immediately after the completion of mixing and molding, all specimens were covered with plastic caps and kept in moist, sealed plastic containers for 24 hours. After 24 hours, the specimens were demolded and were stored in sealed plastic containers for 27 more days at 22°C. At 28 days of age, they were removed from the curing room, and were cut using a diamond saw and polished to provide a 25 mm section parallel finished surface. Those specimens found to be most free of visible cracks were selected for the attenuation measurement.

Using the coherent measurement together spectral ratio technique described in section 5.3.1, attenuation in the entrained air hardened paste specimens can be measured. Figure 5.10 shows the experimentally measured attenuation, α (in Neper/m)

[2]see Sec. 5.1 for a qualitative visual description of the specimen

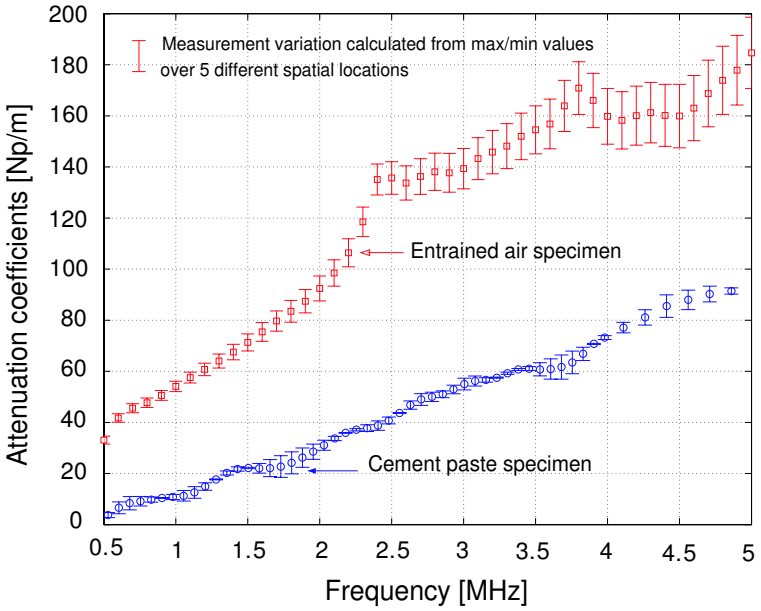

Figure 5.10: Comparison of frequency dependent attenuation coefficients, α (longitudinal only) measured in the entrained air and cement paste specimens

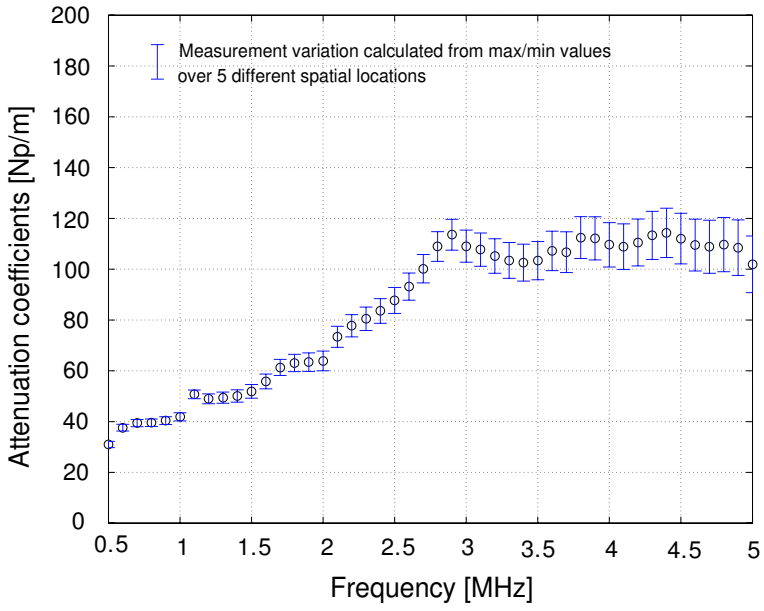

Figure 5.11: Scattering portion (only) as a function of frequency (longitudinal waves) in the entrained air specimen

as a function of frequency (longitudinal wave only) and compares it to the experimentally measured cement paste results. Error bars indicate point-to-point difference in measured attenuation variation across the specimen surfaces. Noting from Eq. (5.14) that the total attenuation is this entrained air hardened cement paste is the sum of both absorption (cement paste matrix) and scattering (entrained air voids), it becomes clear that the additional attenuation present in the entrained air hardened cement paste specimens is only due to scattering from the scattering from the entrained air voids. It should be possible to separate these two effects (the scattering effect from the absorption effect) by subtracting the (longitudinal) attenuation measured in the cement paste specimen from the attenuation measured in the entrained air hardened cement paste specimen — this result is presented in Fig. 5.11. This scattering only attenuation can be used in the proposed inversion analysis (described in the next section) to obtain quantitative information about the entrained air void size and volume fraction that exist in the entrained air hardened specimens.

5.5 Determination of entrained air void size and fraction - the inverse problem

Section 5.1- 5.3 examined the forward problem — application of a single scattering model to determine the attenuation coefficient when the size and volume fraction of the entrained air voids are assumed to be known. The more important problem is the opposite — determination of the entrained air void fraction and size using a set of experimentally measured attenuation coefficients. Ideally , this inverse procedure should also treat the distribution of air void sizes as a third unknown, but as a first step, this research assumes that there is only a single size of entrained air voids present within the volume fraction, ϕ. The Nelder-Mead downhill simplex method [63] is used

to predict the entrained air void radius, a, and volume fraction, ϕ, from the experimentally measured attenuation coefficients. This inversion procedure is accomplished by comparing the theoretical results of the attenuation model (which is a function of two variables, a and ϕ) with the experimentally measured attenuation coefficients to determine the best fit between the experimental results and the theoretical prediction. The proposed objective function is – $\varepsilon = \sum_f [\alpha(a,\phi)_m - \alpha(a,\phi)_{th}]^2$. The subscript "$m$" denotes that experimentally measured attenuation coefficients, while "th" denotes the values predicted with the theoretical attenuation model. A flow diagram of the inversion procedure and associated criterion is shown in Fig. 5.12.

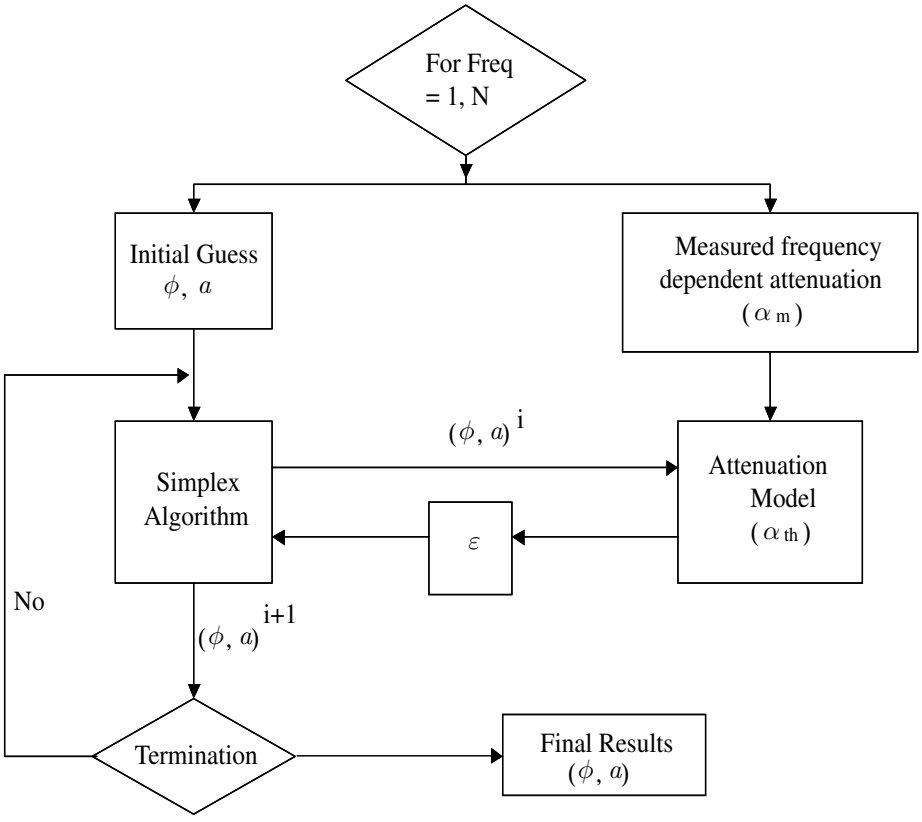

Figure 5.12: A flow diagram for the inversion procedure

5.5.1 Downhill simplex method

The simplex method is an efficient iterative algorithm to solve unconstrained minimization problems numerically for several but not too many variables. Quick convergence and intelligent choice of linearization of the function to be minimized are non-trivial key elements in general minimization algorithms. The method does not use derivatives, analytic or numeric. It attempts to enclose the minimum inside an irregular volume defined by a *simplex* (= an n-dimensional convex volume bounded by (n-1)-dimensional hyperplane and defined by n + 1 linearly independent corners, e.g. a tetrahedron for n = 3). The simplex size is continuously changed and diminished, so that finally it is small enough to contain the minimum with the desired accuracy. The operations of changing the simplex optimally with respect to the minimal/maximal function values found at the corners of the simplex are contraction, expansion and reflection, each determining new simplex corner points by linear combinations of selected existing corner points [63]. The following demonstrates the easiest example of how downhill simplex algorithm works for finding a local minimum of a function of two variables. Let $f(d_1, d_2) = (d_1 - 12)^2 + (d_2 - 3)^2$ be the function that is to be minimized. A simplex in this case is a triangle. First, the three vertices of the triangle are given: $P_i = (d_{1k}, d_{2k})$, for $k = 1, 2, 3$. It should be noted that these given values must not be the same (the simplex volume can not be zero) otherwise the motion of the simplex is restricted and the algorithm will not converge to a minimum. The function $f(d_1, d_2)$ is then evaluated at each of the three points: $y_i = f(d_{1k}, d_{2k})$, for $k = 1, 2, 3$. Next, the points with the highest and lowest values of y_i are determined. They are called P_h(high) and P_l(low). The corresponding values of $f(d_1, d_2)$ at these two points are y_h and y_l, respectively. The centroid of the points P_i with $i \neq h$ is then calculated. There are now three possibilities how the point P_h can be replaced for the next iterations: P_h can be reflected, expanded, or contracted towards the centroid. Figure 5.13 shows the possible movements of a 2−D simplex during one iteration.

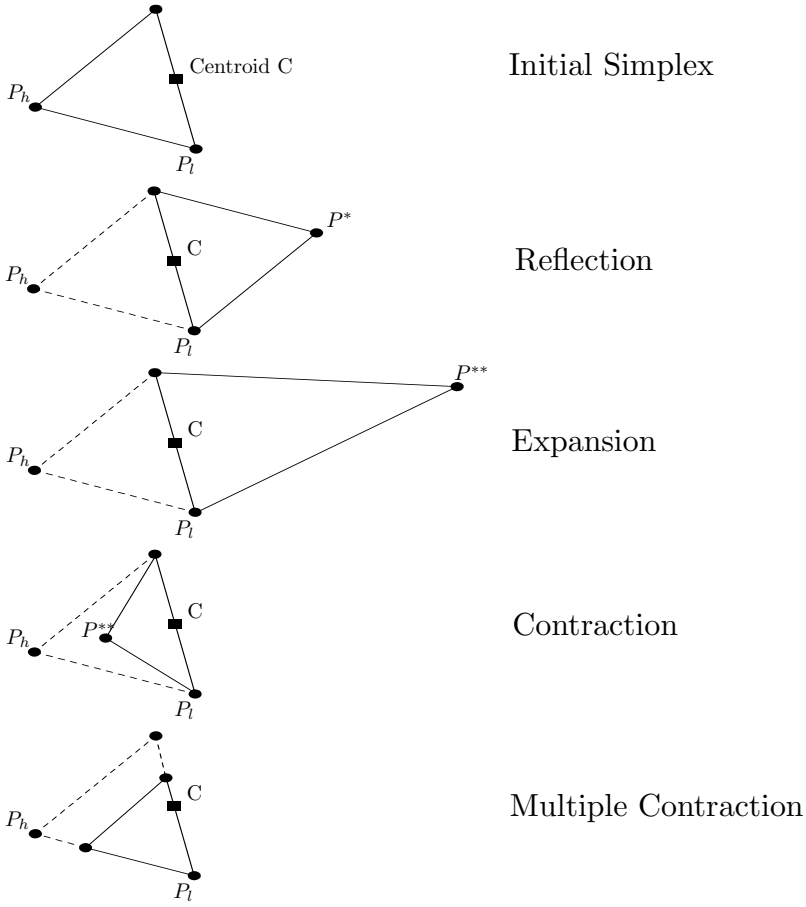

Figure 5.13: Possible motions of a simplex

The values of d_1 and d_2 found from the minimization of the function using downhill simplex algorithm are 11.9990 and 3.0013, respectively. It should be noted that the minimization is terminated when 20 iterations have been completed. These values are obviously the absolute minimum of the function and so the convergence of the optimization is not critical. Figure 5.14 shows that the points of simplex move through d_1-d_2-plane originating at the values initially guessed. The choice of the values is arbitrary. The centroid of the simplex is marked with a small circle. It can be seen

from Fig. 5.14 that the area enclosed by the simplex decreases and finally converges to zero. Figure 5.15 shows the range of the minimal and maximal values for d_1 and d_2 which the points of the simplex have at each iteration. After 20 iterations the points have converged to the real solutions.

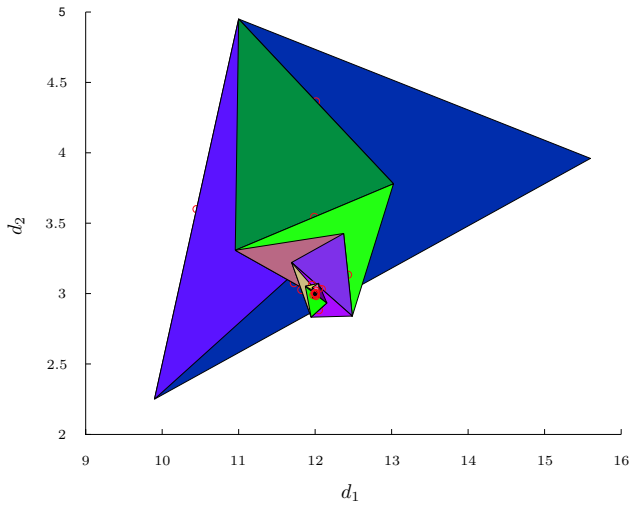

Figure 5.14: Simplex vertices and triangles drawn after 20 iterations

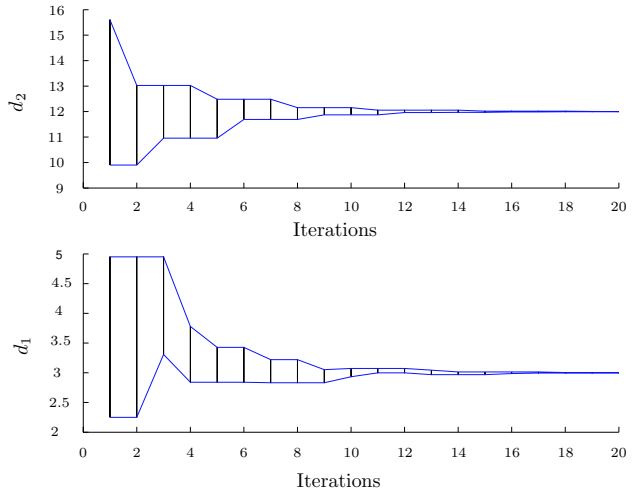

Figure 5.15: Convergence of the Simplex algorithm after 20 iterations

5.5.2 Entrained air void size and fraction measurement

The results of measurements of entrained air void size and volume fraction using the Nelder-Mead simplex method are presented in Figs. 5.16 and 5.17, these figures clearly show the convergence to the values of $a = 0.26$ and $\phi = 3.3\%$. These values are within the range measured by Kalliopi et al. [62].

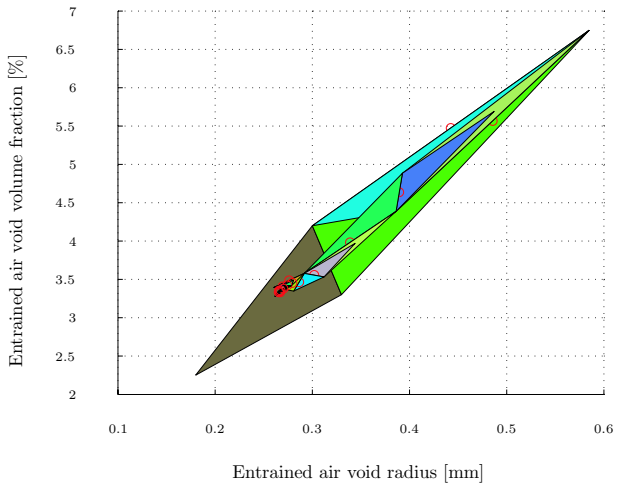

Figure 5.16: Convergence of simplex algorithm, minimization of, ε, 20 iterations

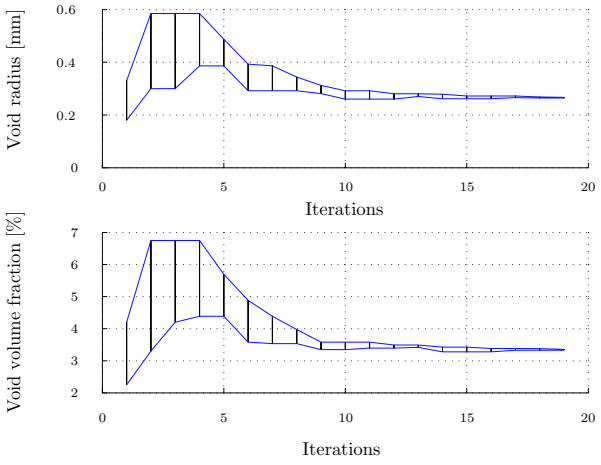

Figure 5.17: Simplex convergence after 20 iterations, a and volume fraction, ϕ

The values predicted by the inversion procedure ($a = 0.26$ and $\phi = 3.3\%$) are substituted into the theoretical model (5.14) and the resulting attenuation coefficient is compared to the experimentally measured values; these results are used as a final verification and are shown in Fig. 5.18. It is seen from this figure that there is good agreement between the two data sets, with the best agreement in the 2-5 MHz range. There is a great difference for frequencies below 2 MHz. A possible explanation for this difference could be due to the assumption of only a single size of entrained air voids present within the volume fraction, ϕ. It might be that the average void size found from the simplex optimization is in fact an estimate of the dominant size that exists in the microstructure of the specimen.

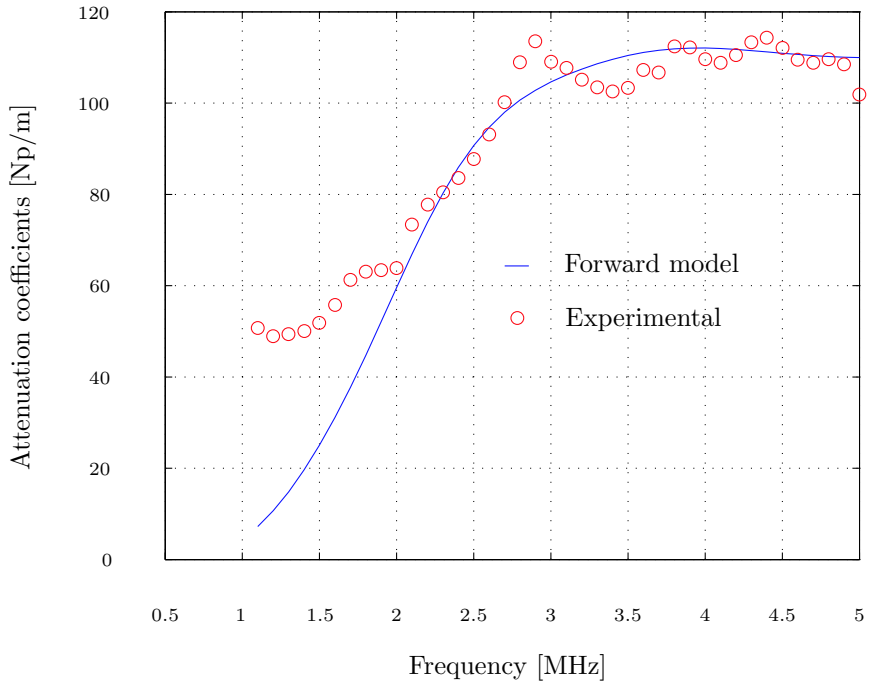

Figure 5.18: Comparison of the experimentally measured attenuation with the simplex optimized vales substituted into the theoretical model

5.6 Effect of a void size distribution

Thus far, it has been assumed that there exist only entrained air voids in the cement paste microstructure and they all have the same radius $a = 0.26$ mm and fraction $\phi = 3.3\%$. In general a distribution of void sizes and fractions (entrained and entrapped air voids) will be present [21]. It is assumed in this section that the probability of the two voids having different radii and fractions is a combination of normal distributions: $P(x) = \frac{1}{2\pi\sigma^2} \exp\left[\frac{-(x-\mu)^2}{2\sigma^2}\right]$ where μ and σ are the mean and variance of the distribution, respectively. Given that, the void volume distribution ϕ is approximated as shown in Fig. 5.19(a), by N discrete segments. For the i^{th} segment, the void radius is a_i and the number of voids at particular radius per unit volume $n_{s,i}$ can be calculated, as shown in Fig. 5.19(b). Also, the scattering cross-section is γ_i^{sca}. In the single scattering approximation, Eq.(5.14) is modified to give the expression for total attenuation,

$$\alpha = (1-\phi)\alpha_a + \sum_{i=1}^{N} \frac{1}{2}\, n_{s,i}\, \gamma_i^{sca} \tag{5.20}$$

Using Eq.(5.20), it is now possible to recalculate theoretical scattering attenuation. The calculation results are plotted together with the results of the measurements of the ultrasonic scattering attenuation coefficient in entrained air specimen and illustrated in Fig. 5.20. It is seen that the assumption of a normal distribution is reasonably good. As is shown in Fig. 5.20, the distribution influences the results significantly. The deviation between the theoretical and measured scattering attenuation in the frequency below 2 MHz (as observed from the previous section) no longer exists. It is clear that these larger entrapped voids ($>$ 1 mm in diameter) are most likely present in the entrained air specimen. Entrapped air voids are approximately up to 3 mm in diameter [21] and they can be accounted for in the expression for total attenuation.

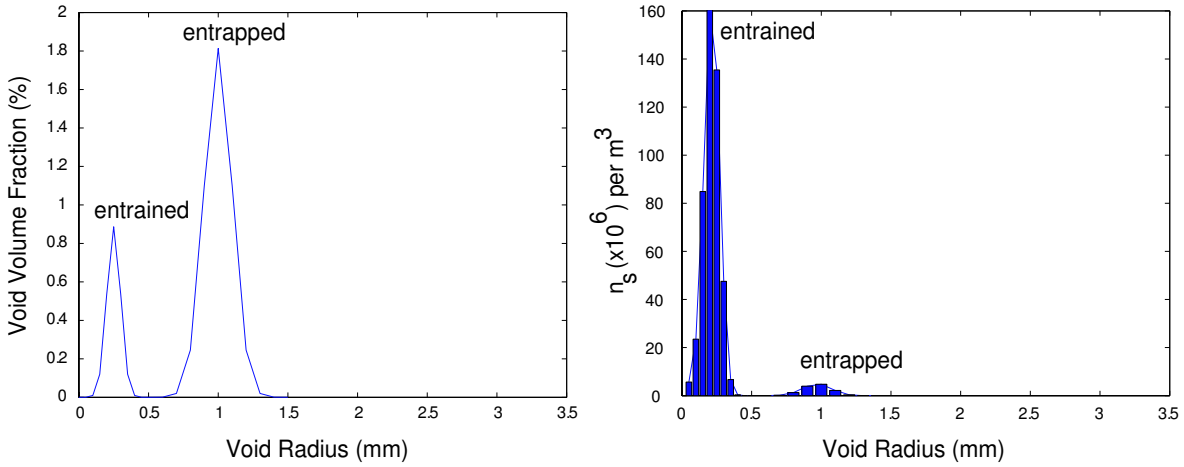

(a) percentage of void fraction (b)number density

Figure 5.19: A plot of (a) percentage of void fraction (normal distribution) and (b) number void density vs. void radius (mm)

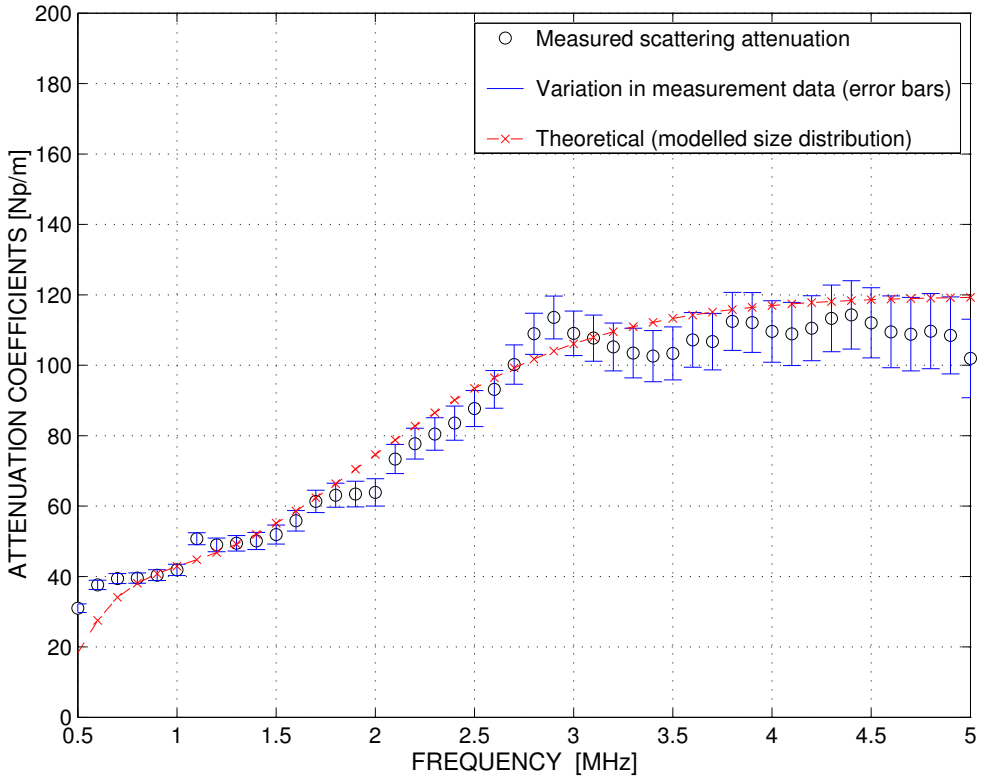

Figure 5.20: Comparison of the experimental and theoretical scattering attenuation result for the void size distribution

Note that the Figure 5.19 and Figure 5.20 leave out some important details of the forward problem — the problem of selecting the entrapped void fraction distribution that would improve the match of the theoretical scattering attenuation values to the experiment ones. Through the use of Figure 5.21 and Figure 5.22, the steps necessary to operate on the forward problem will be explained as followed.

1. Fix a void volume fraction distribution of the smaller void to be such as one shown in Figure 5.21(a). As illustrated in a black curve, the distribution of the entrained air voids has a mean void radius $a = 0.26$ mm.
2. Pick several void volume fraction distributions of the second larger one (referred to as entrapped air voids) that has a mean void radius $a = 1$ mm. These distributions are shown as green, red, and dotted blue curves in Figure 5.21(a).
3. Compute a number of entrained and entrapped air voids that are based on the distribution of entrained air voids (as illustrated in black bars in Figure 5.21(b)) and entrapped air voids (as illustrated in green, red, and dotted red bars in Figure 5.21(b))
4. Compute theoretical scattering attenuation values that are based on a number of air voids given in step 3. As shown in Figure 5.22, the black curve corresponds to the entrained air voids while the green, red, and dotted red curves correspond to the entrapped air voids.
5. Add up the theoretical scattering attenuation values obtained in step 4 (black+green; black+red; black+dotted red), which then gives the dashed blue, solid blue, and dotted blue curves in Figure 5.22. Notice that the solid blue (theoretical) curve shows the best match to the experimental measured ones. This curve is calculated based on the assumed distribution shown as red curve in Figure 5.21(a) and is the solution one expect to obtain from the forward problem.

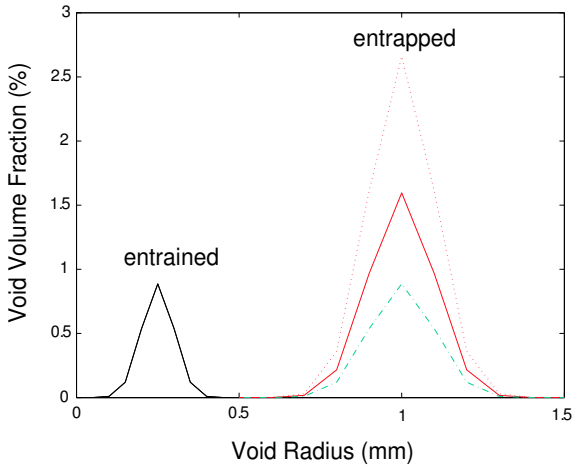

(a) percentage of void fraction

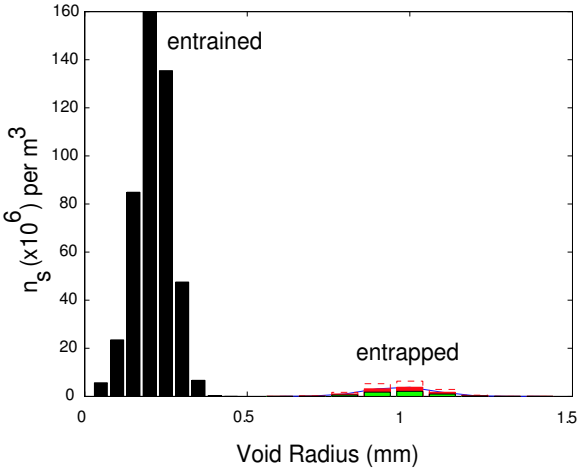

(b)number density

Figure 5.21: A plot of (a) percentage of void fraction and (b) number void density vs. void radius (mm) (forward problem)

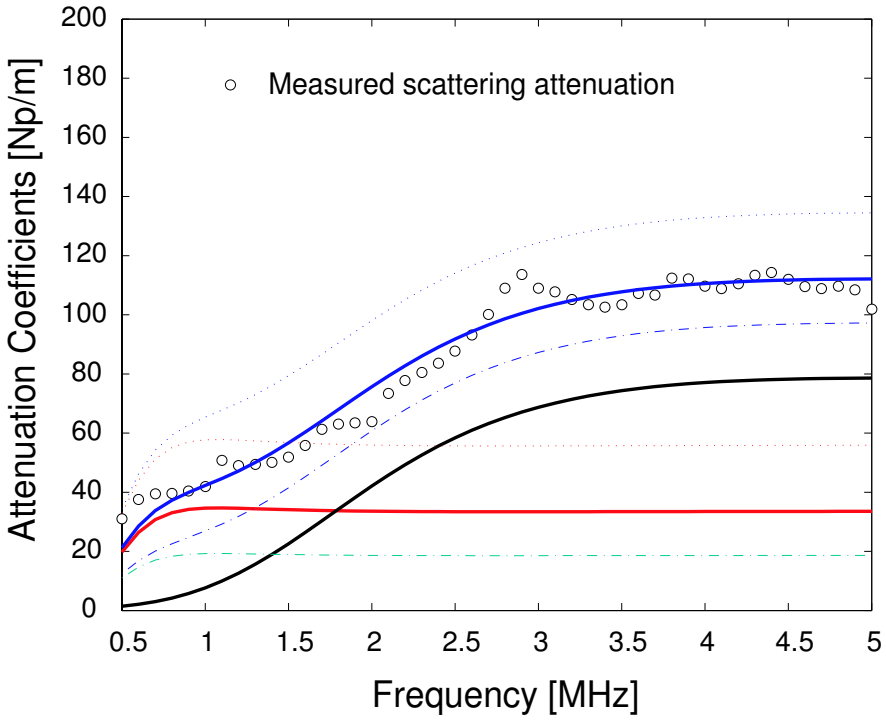

Figure 5.22: Comparison of the experimental and theoretical scattering attenuation result for several void size distributions (forward problem)

It is important to note that it is always possible to have multiple solutions (that is, different combinations of void size and fraction leading to the same scattering attenuation profiles) for a single set of experiments. The scattering attenuation coefficient let alone can not be used to discriminate a broad-size distribution if the attenuation values are not measured over a broader frequency range. The phenomenon can be depicted in Fig. 5.23 where different void fractions of entrained and entrapped air voids are consider. They are all lead to the same scattering attenuation as depicted in the same figure. This is in fact the most important observation and one really needs to account for in the inversion when the information regarding the broadness and uniformity of the void distribution are of important parameters.

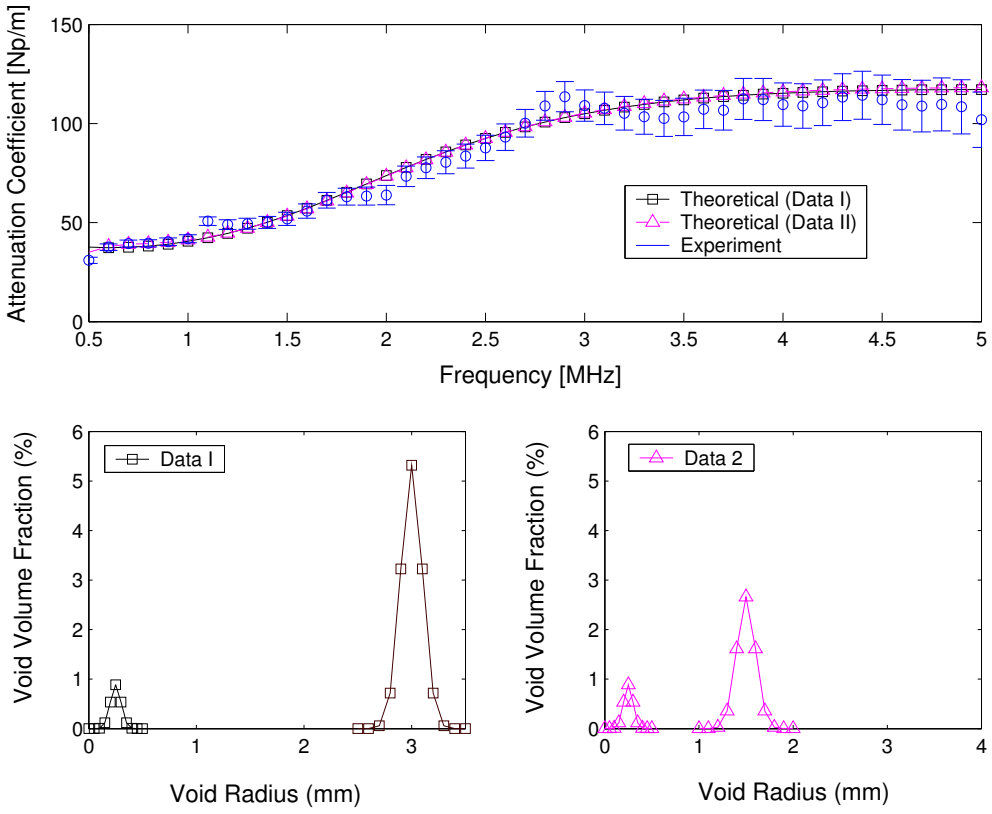

Figure 5.23: Comparison of the experimentally measured attenuation with the simplex optimized vales substituted into the theoretical model

5.7 Summary

It has been shown that the theory of Ying and Truell [57] combined with the independent single scattering approximation of equation 5.14 (following [29]) offers a good description of ultrasonic attenuation in cement paste matrix containing a low volume fraction of entrained air voids with μm radius. A complementary proof-of-principle experimental program measures attenuation coefficients from pulse-burst signals in the frequency range of 500 kHz-5MHz. An inversion algorithm is then used to determine the average size and the volume fraction of the entrained air voids. It is important to note that the theoretical study does not account for any possible distribution of different air void sizes, although it is shown that a distribution of larger void sizes and fractions can influence the profile of the scattering attenuation especially in the frequency below 2 MHz. A future work could include a phase velocity profile, a cumulative frequency distribution of void sizes and fractions into the inversion algorithm for a more robust techniques.

CHAPTER 6

Measurement of entrained air void size and volume fraction in hardened cement paste by ultrasonic techniques

By using the experience gained in the preliminary experiments, it is now possible to apply the knowledge for the hardened cement paste composition characterization. The microstructure of cement based materials varies within much wider limits than that of metals and polymers. According to the selected mixture properties, cement-based materials can contain many internal structural components and types (cement, sand grains, coarse aggregates, voids and cracks filled with air or water) presenting in varying sizes and distributions. Nevertheless, after slight modifications of say the air-entraining mixture and water dosage, these voids and solid particles can also vary in quantity to a much greater extent. The objective of this chapter aims to use ultrasonic attenuation for the characterization of hardened cement paste. Hardened cement paste, a binder matrix of all cement-based materials is chosen because the structural morphology is well documented. The constituents used for the hardened cement paste are cement and water. Chemical air entraining agents can be incorporated in the fresh cement paste mix to generate a system of well-dispersed spherical voids that can help protect the paste from freezing and thawing cycles. Varying water to cement mass ratio (w/c ratio) as well as entrained air void content makes the structural morphology of hardened cement paste specimens very different. Its attenuation behavior therefore is expected to be different. Ability to differentiate this difference

using the ultrasonic attenuation knowledge base developed in previous chapters is undoubtly crucial for the development of powerful nondestructive evaluation (NDE) techniques for diagnostic test of cement-based materials. In this investigation, seven different hardened cement paste specimens are made (each with a different entrained air void content and w/c ratio). Attenuation analysis with coherent ultrasonic measurement is then used for differentiation of w/c ratio and identifying the entrained air void volume fraction and size.

6.1 Specimen Properties

Seven hardened cement paste specimens were manufactured with selected mixture proportions as described in Table 6.1. These specimens contain various entrained air void contents (by volume ϕ) and w/c ratio that are in a range commonly used in practice. The basic ingredients for all specimens were were commercially available Portland ASTM type I cement and water. A chemical air-entraining agent (Darex supplied by W.R. Grace) was added to one set of specimens (the three specimens with the EACP prefix, for entrained air cement paste) during the mixing process to produce entrained air voids.

Table 6.1: Specimen specifications

Name	w/c	Darex entrained agent (% by cement mass)	Diameter (mm)	Thickness (mm)	Entrained air fraction (% by volume)
CP1	0.3	-	100	23.1-25.5	-
CP2	0.4	-	100	23.3-24.7	-
CP3	0.5	-	100	23.2-26.5	-
CP4	0.6	-	100	22.5-24.8	-
EACP1	0.4	0.2	100	23.6-26.5	4.1*
EACP2	0.4	0.6	100	24.7-26.2	8.1*
EACP3	0.4	1	100	22.7-24.8	12.2*

*As examined by a petrographer at Lafarge according to ASTM C 457

A second set of four specimens (with the CP prefix, for cement paste) do not contain the air-entraining agent. Prior to the mixing and molding, all the ingredients were weighted with 0.1 milligram accuracy. 100 mm x 200 mm sealed plastic cylinders were used to store fresh mixes and covered with plastic caps and kept in moist for 24 hours. After 24 hours, all specimens were demolded and restored in an environmentally controlled room for 27 more days at 22°C. At 28 days of age, all specimens were removed and cut using a water diamond saw. Clean cut specimens were polished and dried to provide two parallel surfaces (22.5-26.5 mm thick) to allow transmission of the ultrasonic longitudinal wave without reflections from the side boundaries. Figure 6.1 shows magnified digital images of typical areas of all specimens enabling a qualitative, visual presentation of the relatively homogeneous cement paste matrix as well as the entrained air void scatterers that exist in the EACP specimens but not in the CP specimens.

6.2 Experimental

A schematic diagram of the experimental setup used for the attenuation measurement is the same as the one shown in section 4.2.1 (coherent measurement setup). In brief, two matched pairs of broadband transducers (one pair with a nominal center frequency of 2 MHz, and a second pair with a nominal center frequency of 5 MHz) are used to generate and detect longitudinal ultrasonic waves. The method outlined in section 5.3 is subsequently applied to the acquired signals to achieve a proper analysis of the total (intrinsic) attenuation – the coupling of both absorption and scattering over a broad ultrasonic frequency range of 0.25-5 MHz.

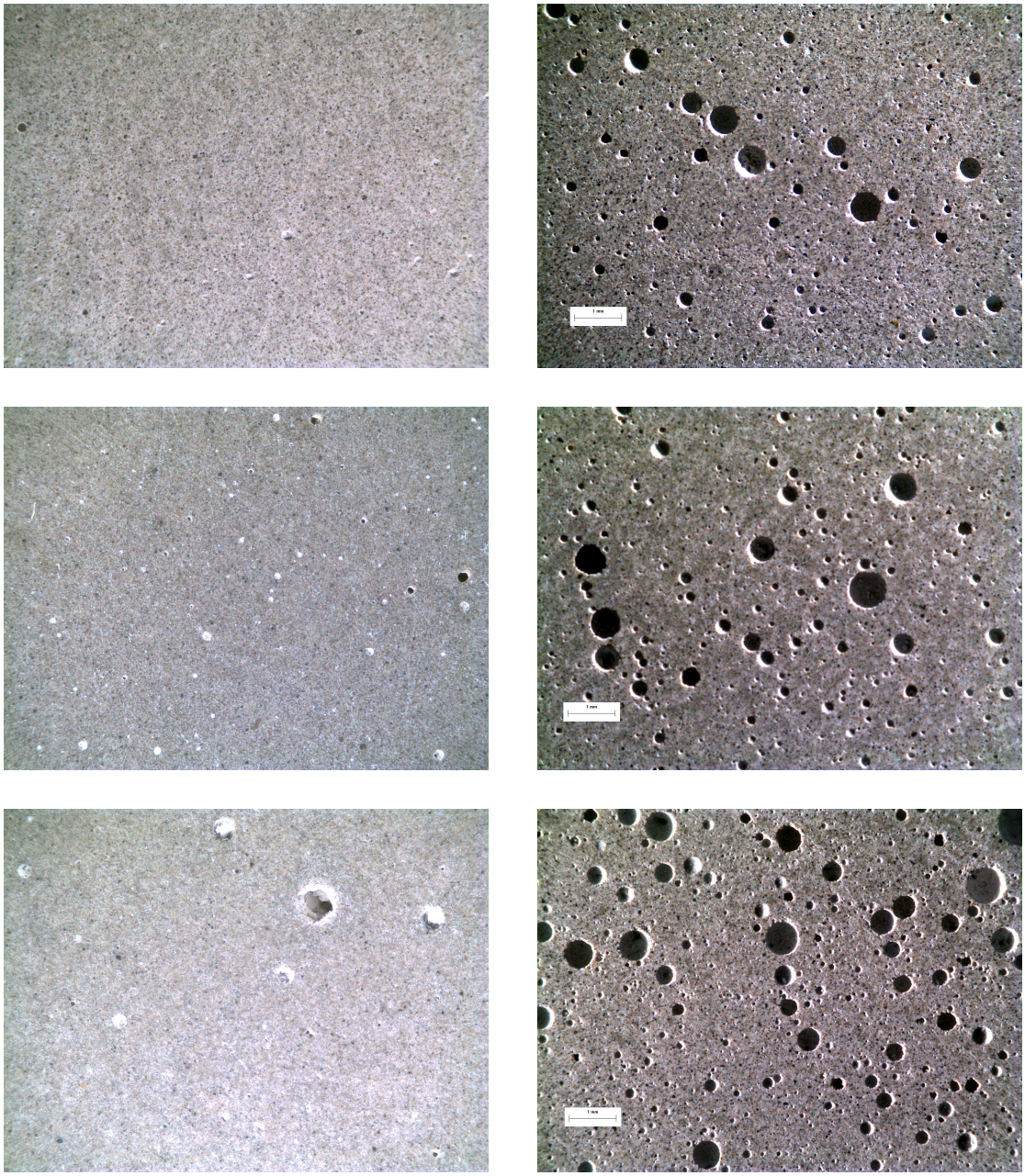

Figure 6.1: From the top: typical structure of (a) CP2, CP3, and CP4 (b) EACP1, EACP2, and EACP3

6.3 Quantitative results for each material system

Figure 6.2 and 6.3 show the total attenuation coefficients of the longitudinal waves as a function of frequency for the hardened cement paste specimens with different entrained air void contents and hardened paste specimens with different water to cement mass ratio respectively. Noting from the measurement procedures described in section 5.4, attenuation measurements are made at five different spatial locations in each of the seven specimens. The results from these five locations are averaged to develop a frequency dependent, total attenuation curve for each specimen.

6.3.1 Effect of entrained air void content

Figure 6.2 presents a summary of the (average) total attenuation values for all three EACP specimens (the three specimens made with air-entraining agent), plus the CP2 specimen (a cement paste specimen made without the air-entraining agent, but with the same w/c ratio). Note that the error bars which are based on the maximum and minimum values of the five spatial locations (at each specific frequency) are not included for visual clarity. Figure 6.2 enables a qualitative comparison of the directly measured attenuation results in these four specimens, and clearly shows that the influence of the entrained air voids. In brief, the attenuation in cement paste specimen is much lower than all three of entrained air specimens; the entrained air voids cause significant (scattering) attenuation (in this frequency range).

Next, the total attenuation in the three EACP specimens is directly related to the amount of air-entraining agent included in their respective mixes; the more air entraining agent, the larger the total attenuation (at a specific frequency). Finally, the attenuation behavior in the CP2 specimen is generally linearly increasing with frequency, while the three EACP specimens exhibit a nonlinear frequency behavior; this overall behavior is predicted by fundamental scattering theory.

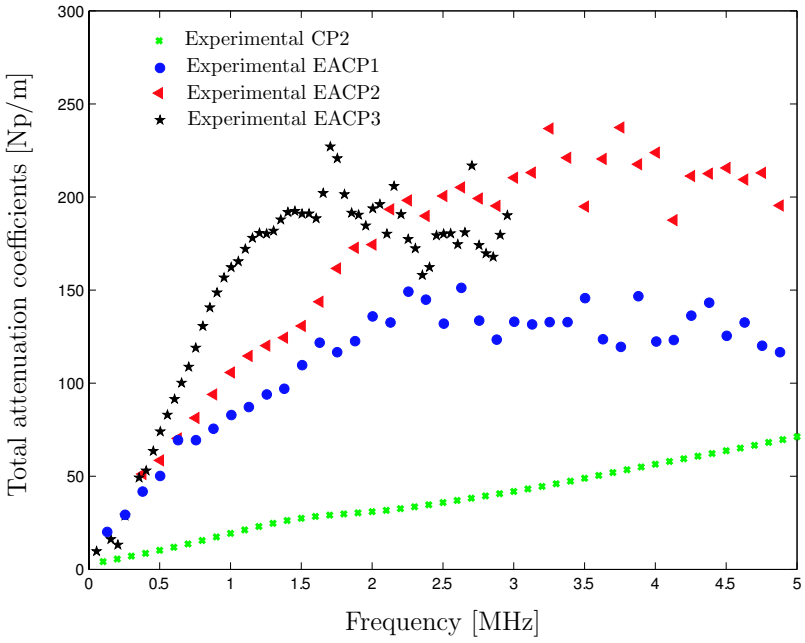

Figure 6.2: Effect of entrained air content on frequency dependent attenuation coefficient, α (longitudinal only) measured in the hardened cement paste specimens

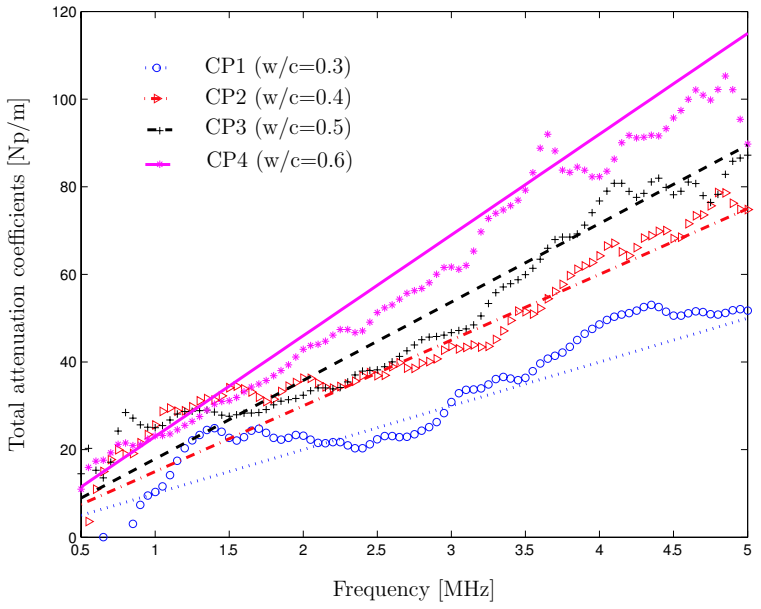

Figure 6.3: Effect of w/c ratio on frequency dependent attenuation coefficient, α (longitudinal only) measured in the hardened cement paste specimens

6.3.2 Effect of w/c ratio

The most crucial parameter affecting the inhomogeneous nature of hardened cement paste is considered to be the w/c ratio and the increase of void (irregular shape and population) with increasing ratio of water dosage has been reported for hardened cement pastes [64]. The case concerning water content influence on attenuation measurement is considered here. Figure 6.3 shows the (average) measured total attenuation, α as a function of frequency for the four cement paste (CP) specimens (each cast with different w/c ratios). There is generally a linear relationship between α and frequency in Fig. 6.3, and note that the total attenuation is much higher in the EACP as compared to the CP (as evidenced by Fig. 6.2). The reason for this lower attenuation is that the scattering contribution, α_s, is nonexistent in the CP specimens at these frequencies, so Fig. 6.3 shows the relationship between changes in w/c ratio and absorption attenuation, α_a. This same linear relationship between absorption attenuation and frequency has been reported in polymers and biological tissues [46– 47] and is referred to as hysteresis absorption.

6.3.3 Entrained air void fraction and size estimation

In order to draw specific information aiming at composition characterization of entrained air void in hardened cement paste, the theoretical model relating the total frequency dependent attenuation coefficient α with entrained air void parameters, previously described in chapter 5, is considered.

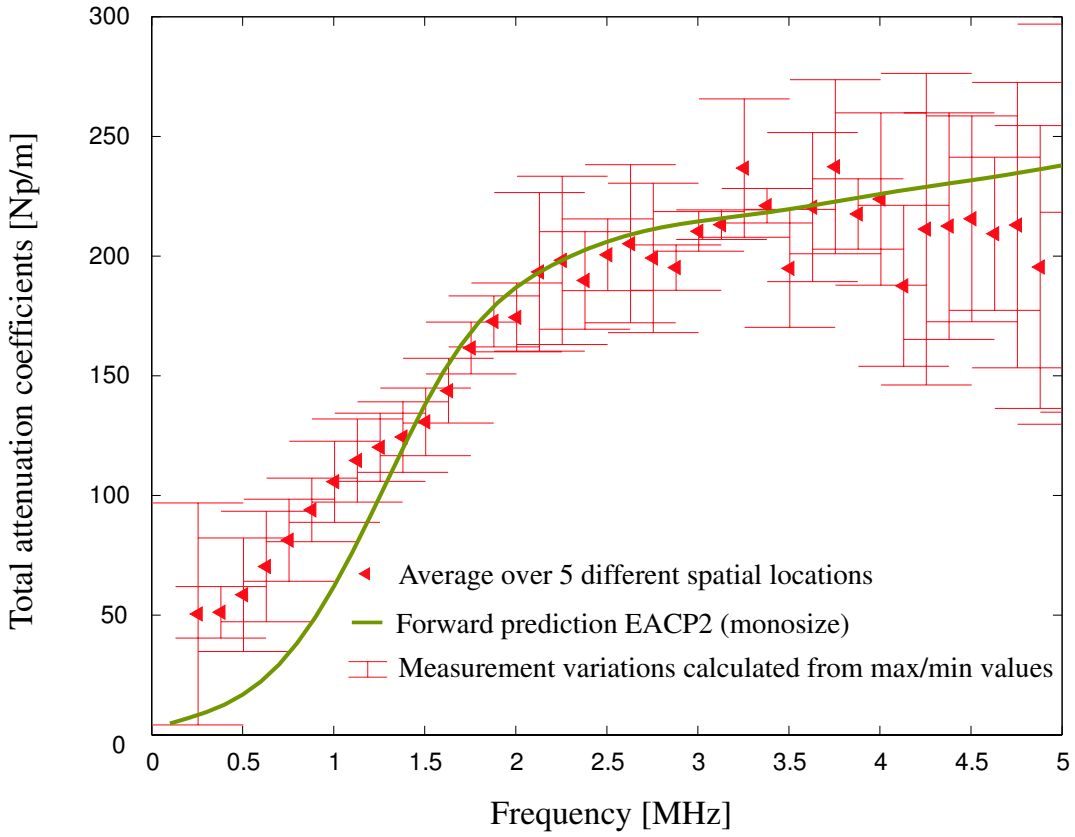

Figure 6.4: Comparison of the experimentally measured total attenuation with the forward predictions using simplex optimized values assuming single sized void distribution for EACP2 specimen

As detailed demonstration of the use of the model, consider the results from a typical EACP2 specimen. Figure 6.4 shows the experimentally measured total attenuation together with error bars, α (in Np/m), as a function of frequency (longitudinal waves only). This is to compare to the attenuation values predicted by the inversion procedure [labeled as Forward Prediction EACP2 (monosize)]. Noting from the previous chapter that the total attenuation in this entrained air specimen is the sum of both absorption (cement paste matrix – CP2) and scattering (entrained air voids). The scattering effect could be separated out by subtracting the (longitudinal) attenuation measured in the cement paste specimen CP2 and this scattering only

attenuation is used in the inversion analysis to obtain quantitative information about the entrained void size and volume fraction that exist in the EACP2 specimen. The inverse procedure treats the entrained air average void size, a, and volume fraction, ϕ as unknowns. Starting with the arbitrary initial guesses the theoretical frequency dependent attenuation values of entrained air hardened specimen is optimized to fit with the measurement values using the 2-dimensional Nelder-Mead downhill derivative free simplex algorithm to obtain the quantitative information about the entrained air average void size a and volume fraction ϕ. The inversion for this particular application is smooth with direct convergence to a single set of values, without any local minima. The range of the minimal and maximal values for entrained air void size a and volume fraction ϕ which the points of the simplex have at each iteration are shown in Fig. 6.5 and 6.6. After 30 iterations the points have converged to the real solution and the values a and ϕ predicted by the inversion are 0.35 mm and 7 %, respectively.

The values predicted by the inversion method are back-substituted into the theoretical model so that the total attenuation coefficient of the longitudinal wave in entrained air hardened cement paste specimens can be recomputed as shown in Fig. 6.4. A comparison of the obtained attenuation shows that there is good agreement between the model prediction and the experiment, with the best agreement in the 1.5-5 MHz range. There is also a greater difference between the model prediction and experiment for frequencies below 1.5 MHz. A possible explanation for this could be due to the assumption of only a single size scatterer (entrained air void) present within the microstructure; this behavior can be explained by the presence of additional larger entrapped air voids, which do exist in reality with a certain distribution but are not accounted for in the monosize scatterer model.

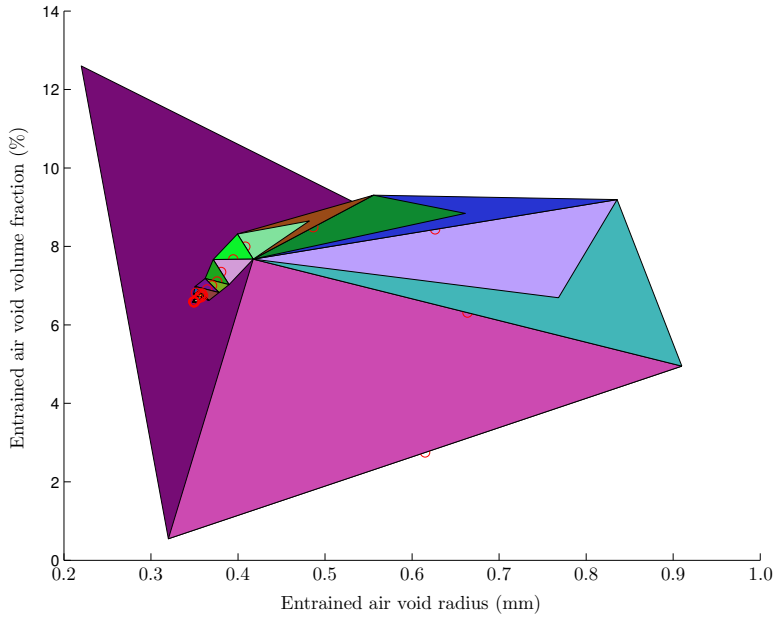

Figure 6.5: Simplex algorithm for the optimization

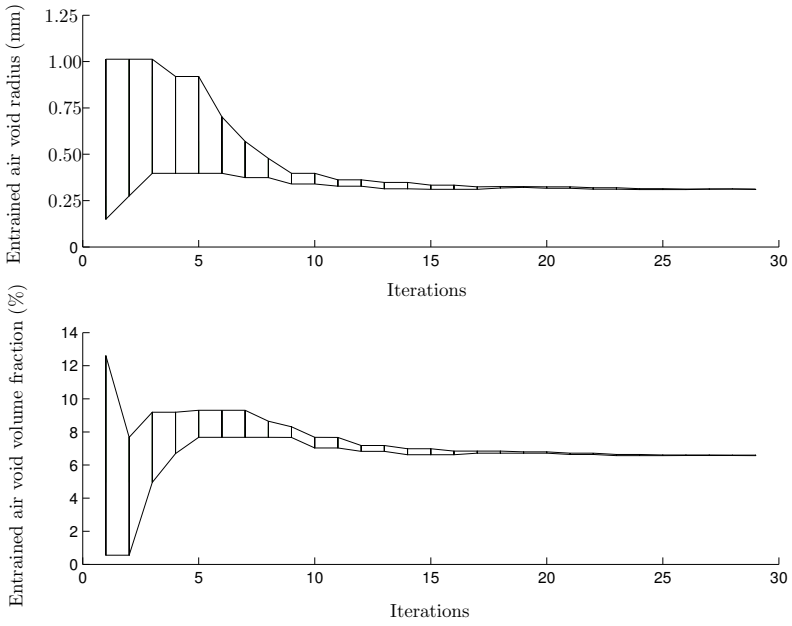

Figure 6.6: Convergence of the simplex algorithm

Table 6.2: Results of ultrasonic measurement of entrained air hardened cement paste specimens in comparison with results obtained by ASTM C457-98

Name	Volume Fraction, ϕ (%)			Radius, a (mm)	
	ASTM C457-98 (Method B)	Simplex Prediction	Percentage Difference	Simplex Prediction	Optical Reading Maximum
EACP1	4.1	3.3	19.5	0.33	0.32
EACP2	8.1	7	13.5	0.35	0.36
EACP3	12.2	11.3	7.4	0.50	0.49

Using the above methodology, Table 6.2 summarizes the best estimate a and ϕ values in the EACP1, EACP2, and EACP3 specimens obtained from the optimization routine and this is visually presented in Figure 6.7 where the experiment measured and forward prediction are coherently plotted on the same graph.

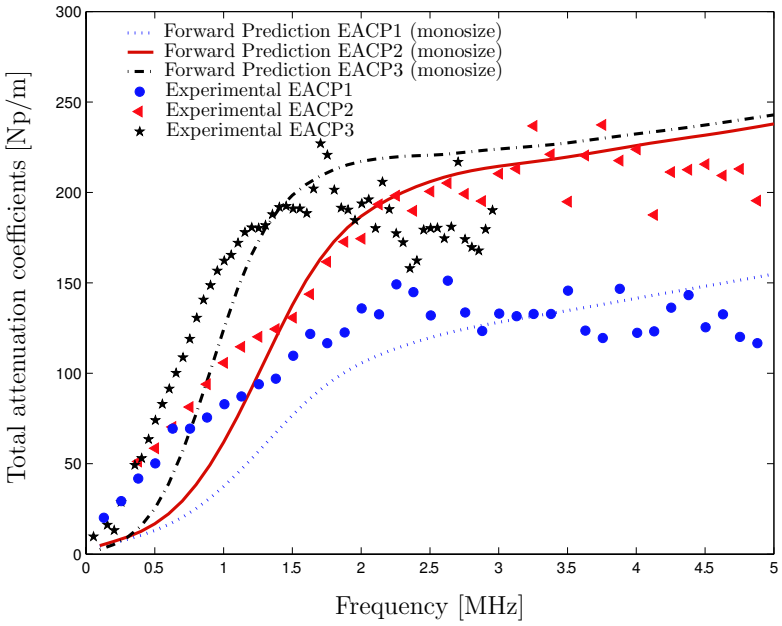

Figure 6.7: Correlation plot of predicted vs. actual values of total attenuation coefficients from entrained air hardened cement paste specimens

A comparison of the inversion results with the results obtained with the ASTM C457-98, method B [39] is listed in Table 6.2. A close correlation between ϕ the volume fraction "attenuation" predictions and the values directly (optically) measured following ASTM C457-98, method B is apparent. A very good agreement between these two set of values demonstrates the accuracy and effectiveness of using attenuation to measure entrained air void size and volume fraction in hardened cement paste.

ASTM C457-98 does not estimate the size of the entrained air voids, so another method is needed to validate the entrained air void sizes, a that are predicted with the inversion procedure. A commercial image analysis software package, IMAGE-PRO Plus, is used to calculate a "maximum" circularity index (or radius) by examining magnified digital surface area images (similar to Fig. 6.1). The procedure considers five randomly selected images (each with an area of 238 mm^2, and details are available in appendix C. Again, the results for the three EACP specimens are summarized in Table 6.2. There is very good agreement between the entrained air void sizes predicted by inversion of the attenuation data, and those optically measured. This very good agreement is further indication of the accuracy of the proposed ultrasonic procedure.

Deviations between predicted and measured total attenuation values are observed consistently in EACP specimens. As mentioned and shown earlier in Fig. 6.7, these are most likely due to the limitations of assessing over all possible air voids of the hardened cement paste and that has to do with the limitations of single sized scattering assumption used in the theoretical model. Working on improving the overall resolution of the statistical shape and distribution of air void size and volume fraction should better explain this. Following Mehta et al. [21], consider a more complicated cement paste microstructure system that has two dominant void sizes and fractions

(each having a normal distribution) as shown in Fig. 6.8 for the case of EACP1 and EACP2 and in Fig. 6.9 for the case of EACP3. The distribution of the smaller voids (referred to the entrained air voids) has a mean void radius of the a values from the inversion procedure (listed in Table 6.2), while the larger one (referred to as entrapped air voids) has a mean void radius of 1 mm and bigger (as suggested by [21]). Note that both distributions are symmetric, and have the same standard deviation, with more values near the center of their distribution, and relatively fewer in the tails.

With this assumed microstructure, it is now possible to calculate the number of voids at a particular radius, per unit volume (calculated by $n_s = \frac{3\phi}{4\pi a^3}$), which are shown in both figures. It is now possible to analytically predict the scattering attenuation coefficient for this new, two-size distribution microstructure by superimposing these discrete void sizes, and then calculating a new theoretical scattering attenuation with the theoretical attenuation model. By summing both absorption (cement paste matrix - measured from CP2 specimen) and the scattering attenuation, a new theoretical total attenuation is in a better agreement between the experimental values as shown in Fig. 6.8, for the case of EACP1 and EACP2 specimens and in Fig. 6.9 , for the case of EACP3. It is clear that the inclusion of a second (larger in size but lower in population density) scatterer improves the prediction of total attenuation coefficient (especially in the low frequency region); there is a much better agreement between the experimental and theoretical results. Note that these larger scatterers are most likely present in both the cement paste and entrained air cement paste specimens in the form of larger entrapped air voids. Future work could include this distribution into the inversion algorithm for a more robust measurement technique.

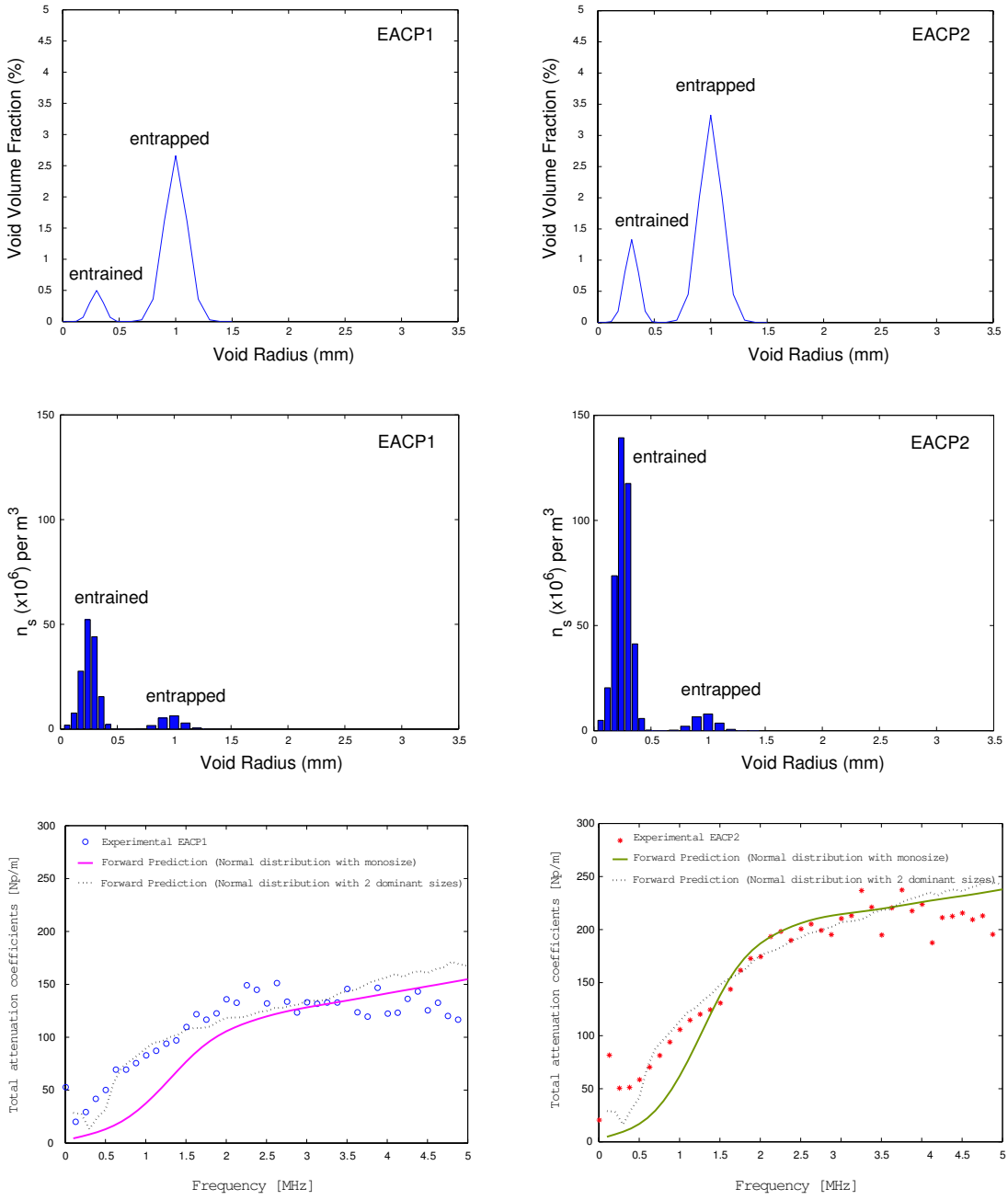

Figure 6.8: Comparison of the experimentally measured attenuation with the analytical predictions using simplex optimized values and the assumed two void size normal distributions for the case of EACP1 and EACP2

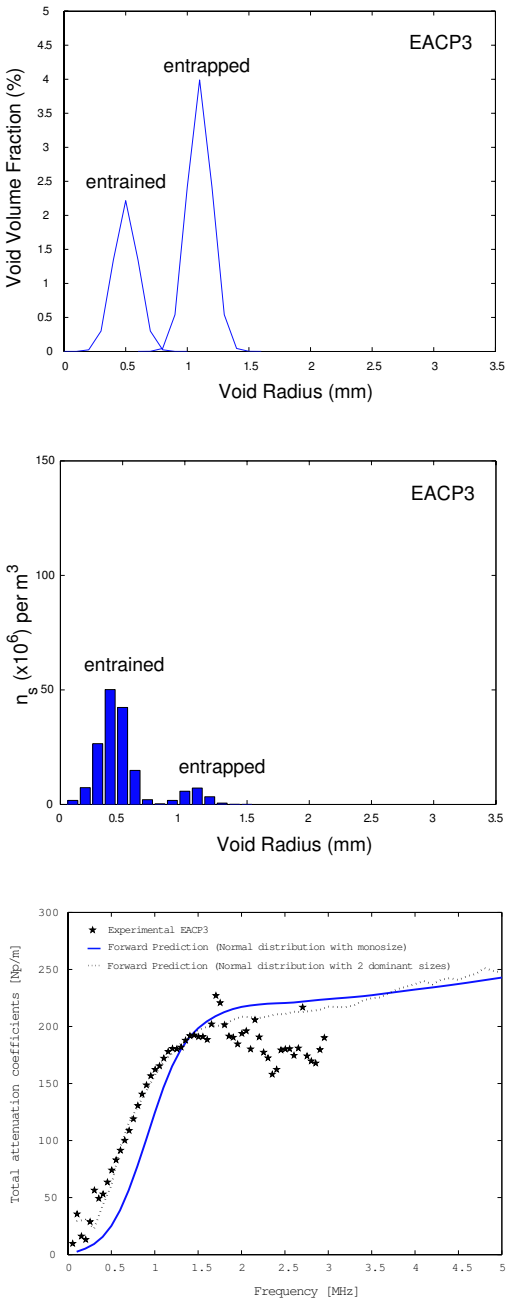

Figure 6.9: Comparison of the experimentally measured attenuation with the analytical predictions using simplex optimized values and the assumed two void size normal distributions for the case of EACP3

6.3.4 Relationship between w/c ratio and absorption attenuation

Measurement results conducted in hardened cement paste specimens containing different amounts of water reveal the pronounced effect of water content in the total attenuation. In Fig. 6.3 the attenuation vs frequency curves for different w/c specimens CP1, CP2, CP3, and CP4 is depicted. There is generally a linear relationship between α and frequency, and note that the total attenuation is much higher in the EACP as compared to the CP specimens. Noting from the model that the total attenuation is the sum of absorption and scattering. The microstructure of these specimens, which is mainly controlled by w/c, does not exercise significant influence on scattering but on absorption, so Fig. 6.3 shows the relationship between w/c ratio and absorption attenuation, α_a. This same linear relationship between absorption attenuation and frequency has been reported in polymers and biological tissues [46– 47] and is referred to as hysteresis absorption.

This measured absorption attenuation behavior can be explained by considering the influence of w/c ratio on microstructure. Consider [64], who report that changes in w/c ratio will result in changes in the volume of solids and capillary voids (the irregular 10 to 1000 nm void spaces sometimes filled with viscous liquid, but not occupied by the solids nor entrained air voids). A popular method of calculating the total volume of these voids is with the Power phenomenological model, and following [21], the ratio of capillary voids to total solids (hydration products and unhydrated cement) is shown in Fig. 6.10 for these four w/c ratios. There is a clear increase in the volume of capillary voids (and a corresponding decrease in the amount of solids) with increasing w/c mass ratios. Biot's theory [65], which is based on the friction losses of a fluid as it moves within the capillary voids, can be used to predict absorption

attenuation in such materials. While Biot's theory can explain the phenomena of increasing absorption attenuation for increasing w/c ratio, further research is needed to quantify this effect and thus use absorption attenuation to quantitatively measure w/c ratio.

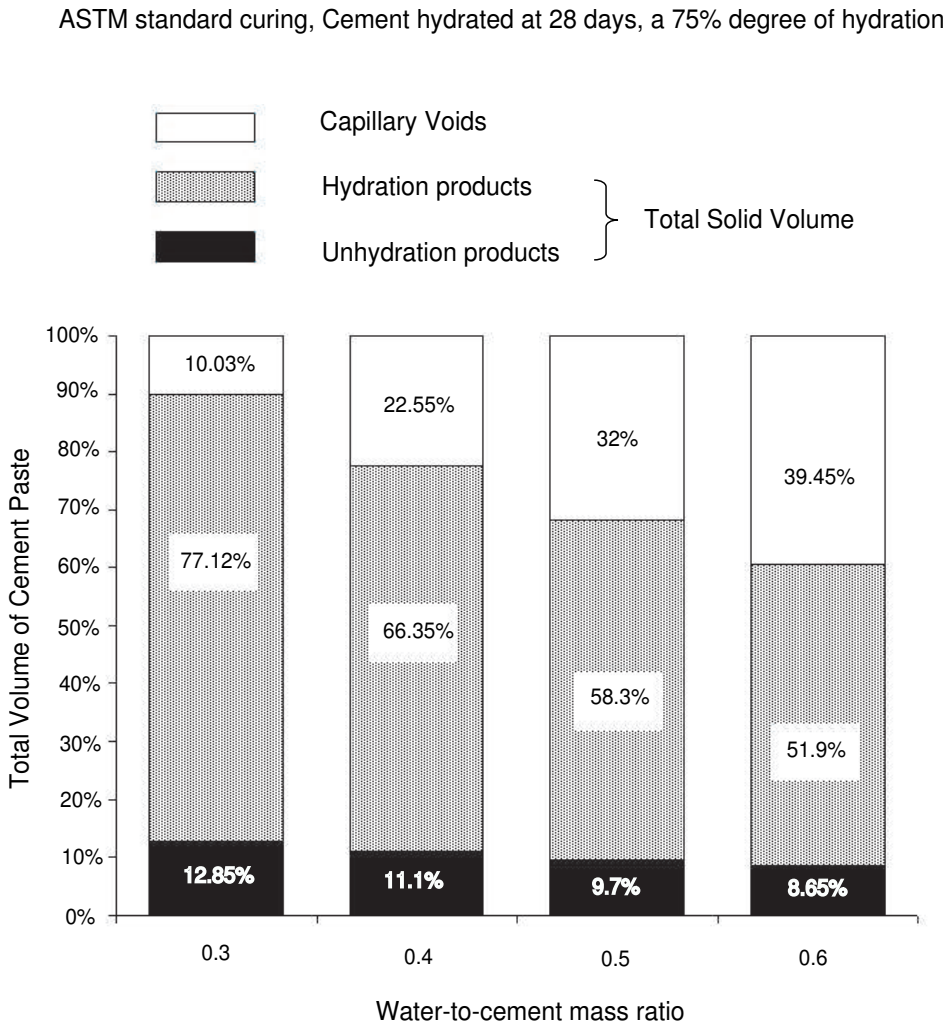

Figure 6.10: Microstructural phase model of hardened cement paste comprising solids, capillary voids and air with varying water/cement ratio

6.4 Summary

The objective of this study is two-fold: the study of ultrasonic wave propagation in hardened cement paste followed by an investigation on the possibility of characterizing microstructural properties. Results from the coherent measurement performed on a set of cement paste specimens with entrained air void content and w/c ratio varying indicate the attenuating nature of hardened cement paste. The dominant role of the entrained air void content in wave propagation affecting longitudinal wave attenuation is highlighted. Remarkable differences, especially in total frequency dependent attenuation, where entrained air rich mixes exhibit much higher attenuation than paste for megahertz frequencies. This leads to the assumption that the total attenuation of ultrasonic wave in the entrained air specimen can be related to the absorption in the cement paste matrix and scattering by the entrained air void. The theoretical investigation using established single (one-size) scattering theory is undertaken and the inversion algorithm applied on the experimentally measured scattering attenuation leads to the prediction of entrained air void size and volume fraction in each specimen. The accuracy of these ultrasonic predictions is verified by direct comparison to optical results. There is very good agreement between these two sets of results, showing the accuracy of using attenuation to measure entrained air void size and volume fraction in hardened cement paste. These attenuation measurements are then used to quantify the existence of additional larger entrapped air voids in the microstructure.

A final component develops a direct relationship between attenuation and w/c ratio. The dominant role of water content in wave propagation affecting both longitudinal wave velocity and attenuation is also highlighted. The major result of the experimental attenuation measurements has been to show that higher w/c ratio results in

higher absorption attenuation. A phenomenological model based on the existence of fluid-filled capillary voids (free volume not occupied by the solid) is used to help interpret the experimentally observed behavior. Guided by the experimental results found from these measurements, the free volume segments are the critical source of absorption losses in cement paste, and the absorption attenuation increases with increasing free volume.

Overall, this research shows the potential of combining ultrasonic measurement techniques with theoretical wave propagation models to quantitatively characterize cement-based materials. The technique posses the potential to be developed into a cheap but powerful nondestructive evaluation (NDE) technique for diagnostic test of cement-based materials.

CHAPTER 7

Application of diffusion sound field to attenuation measurement of cement-based materials

In Chapter 5, it is found that the sum of longitudinal waves that are singly scattered by random distributed heterogeneities can provide an adequate first order model of the scattering attenuation of the entrained air hardened cement paste. As elapse time increases, however, double, triple and higher-order multiple scattering contribute more than the single scattering process should be expected. A systematic approach for modelling the multiple scattering process is to use the principle of conservation of energy, in the form of the equation of radiative (energy) transfer. The theory states that at times long after an ultrasonic source has applied onto a solid body containing many scatterers, long that is compared to the typical time between the randomizing scattering events of an ultrasonic ray, the average transmission of ultrasonics energy may be described by the diffusion process. Many researcher who are accustomed to thinking of the propagation of scattering waves in terms of deterministic elastic wave theoretical approach, the notion of a diffusion process may seem improper. However, this is simply a different approach to the problem, and the characteristics of scattering waves is never denied. The diffusion process is probabilistic, which treats only the statistical aspects of the flow of energy, the total energy is conserved, and the equation that governs the energy flow is the diffusion equation with an additional term representing linear dissipation to heat. Thus it should apply equally well to the

description of the ultrasonic waves propagating in scattering medium, especially in the measurement of attenuation of ultrasonic waves providing a sensitive probe to the microstructure and the properties of material in which they propagate. In this chapter, the application of the diffusion formalism to the propagation of ultrasound pulses transmitted through seven cement paste specimens (each made with different entrained air void contents and w/c ratios) is explored. These specimens have been used in chapter 6. It can be shown that the use of diffusion equation and the key parameters (dissipation and diffusivity associated with the equation) does provide a good description of the propagation of ultrasonic waves in cement-based materials. There is a reasonable correlation between the dissipation and the amount of the cement paste present in these samples and the corresponding values can be related to the absorption attenuation values measured with a coherent measurement procedure (if the phase velocity is known). The measured diffusivity shows quantitative trends but does not precisely resolved variations in microstructure of the cement paste.

7.1 Diffusion formalism

The transmission of ultrasonic energy through strongly scattering media may be considered as a diffusion process. In this case, a measured of scattered wave field can not be easily approximated as a small disturbance of the direct waves as assumed in the Born approximation or in the quasi crystalline approximation [48], [66– 67] — these theories depend highly on geometry and dimensionality, as well as on the nature of the waves. As an alternative, the radiative transfer equation or the diffusion equation is used [42], [68–70] where instead of the reciprocity for the amplitude propagation of the waves the transport of energy in the scattering medium is examined. In this approach, the average energy density (energy per frequency and per volume) is treated as a wave undergoing a random walk. Subsequently, the phase information

is neglected and the variation of energy in time and space can be described by an analytical equation.

The success of the diffusion approach to the interpretation of the multiply scattered ultrasound in relation to much material micro-structural heterogeneity indicates that this is a valid approach. On using the diffusion equation, Guo et al [71] studied multiply scattered ultrasound in polycrystalline iron. Weaver et al [72] did similar work on brasses, steels, and aluminum foams. Page et al [73] studied diffuse multiply scattered ultrasound in a slurry of glass beads in water. Changes in phenomenological diffusion parameters of that diffusion equation — the diffusivity and the absorption were found however it becomes one of the experimental challenges in measuring these parameters. One of the reasons is that only a few materials actually exhibit strong scattering at the working frequencies. Another lies on the technology necessary to separate the frequency, time and space dependence of the speckle. Speckle is the result of the interference of scattered wave and can exist over a large domain of the ratio of scattering mean free path to the thickness of the specimen.

Anugonda and Turner [19] applied the diffusion approximation theory to concrete. The ultrasonic diffusion experiments were conducted on a series of circular cylinders of concrete over the range of 0.1-0.9 MHz. The diffusion of ultrasonic energy parameters was modelled by a 1-D diffusion equation. Dissipation and diffusivity were extracted from experimental data using a linear regression fit to the equation. The variation in the calculated parameters was found for one type of concrete having a water/cement/sand/aggregate mixture of 1:0.5:2.5:5. Becker et al [28] on the other hand used a 2-D diffusion theory to quantitatively measure dissipation and diffusion coefficients as a function of frequency and microstructure. The study was done by examining specimens made of a Portland cement paste matrix and glass bead with a

variety of sizes and distribution over a higher frequency range (0.3 - 2 MHz). Using a very small point-like padded transducer, the amplitude of the scattered ultrasound signals is measured. Experimentally measured ultrasonic waves are interpreted using diffusion theory and statistical time-frequency analysis. The results demonstrate one advantage of using diffuse ultrasound to measure dissipation and diffusivity in a separate manner. Both measured dissipation and diffusivity values convincingly demonstrated the effect of some features of the microstructure and validity of using the diffusion approximation on describing the propagation of ultrasound through cement-based materials. Additional theoretical studies were conducted through the use of the elastodynamic finite integration technique [74]. The 2-D concrete beam was modelled by using aggregates and air-filled voids embedded in a homogeneous cement paste matrix. The beam was subjected to a broad frequency excitation range from 0 to 1.5 MHz and diffuse responses were measured 45 cm away from the source. The numerical results of the plane strain analyses revealed a significant impact of porosity on the diffusion coefficients.

7.2 Basic diffusion equation

The formal derivation of diffusion equation has been given by Dainty and Toksoz [50]. For the sake of completeness, those equations as in acoustics will be repeated here to give a simple but generic idea of how the equation is derived. The extension to the elastic solid is then discussed for the application of ultrasonic experiments.

A situation is given in which the effect of scattering is so strong that all energy is scattered energy. The wave field is assumed as being made up of plane waves of frequency f, travelling in all directions with random phases — thus, energies are additive, not amplitudes. If one define direction by polar angles θ, φ, and $e(\vec{r}, t, \theta, \varphi)$

as the energy density at $(\vec{r}, t)$ of waves propagating in direction (θ, φ), then the total energy density $\langle E(\vec{r}, t)\rangle$ can be written as

$$\langle E(\vec{r}, t)\rangle = \int_S e(\vec{r}, t, \theta, \varphi) d\vartheta \tag{7.1}$$

where $d\vartheta$ is an element of solid angle and the integration is over all solid angles. It should be noted that the medium through which the waves are propagating has a wave velocity c_E, and n_s scatterers per unit volume. The scatterers each have a scattering cross section γ^{sca} and a differential scattering cross section $\Omega(\Theta)$, taken to be a function of scattering angle,Θ, only. Then

$$\gamma^{sca} = \int_S \Omega(\Theta) d\vartheta \tag{7.2}$$

It should be noted that γ^{sca} and $\Omega(\Theta)$ are generally strong functions of frequency. Consider an elemental volume V, and the waves travelling in direction θ, φ. Then the conservation of energy states that

$$\frac{\partial e}{\partial t} V = -\int_S \vec{F} \cdot \vec{n} dS + V[\int_S n_s c_e e(\acute{\theta}, \acute{\varphi}) \Omega(\Theta) d\acute{\vartheta} - \int_S n_s c_e e(\theta, \varphi) \Omega(\Theta) d\acute{\vartheta} - \sigma e] \tag{7.3}$$

The first term on the right in Eq.(7.3) is the net flux across the surface S of the elemental volume V, with normal $\vec{n}$, the second term represents energy scattered out of θ, φ from all other direction $\acute{\theta}, \acute{\varphi}$, the third term represents energy scattered out of θ, φ into all other directions, and the fourth term represents energy dissipated into heat in terms of dissipation coefficient σ.

For the flux expression for a travelling wave $\vec{F} = c_e \vec{k} e$, where $\vec{k}$ is a unit vector in the direction of the propagation of the wave. Applying Gauss's theorem to the second term in Eq.(7.3),

$$\frac{\partial e}{\partial t} + \vec{\nabla} \cdot c_e \vec{k} e + \sigma e = \int_S n_s c_e \Omega(\Theta) [e(\acute{\theta}, \acute{\varphi}) - e(\theta, \varphi)] d\acute{\vartheta} \tag{7.4}$$

Notice that this is the time-dependent equation of radiative transfer theory [75]. In deriving Eq.(7.3) and Eq.(7.4) it is assumed that it is possible to define a volume sufficiently small that multiple scattering may be ignored within V. Notice that this assumption is coincided with assumption made early on the independent single scattering theory. Next, it is one wish to parameterize the scattering medium in terms of a scale length. To do this, a wave field consisting of a plane wave travelling in some particular directions is considered θ_0, φ_0 at $t = 0$

$$e(\vec{r}, t, \theta, \varphi) = \delta(\theta - \theta_0)\delta(\varphi - \varphi_0)e(\vec{r}, t) \tag{7.5}$$

As time increases, energy will be scattered into other directions, and eventually, via multiple scattering, back into the direction θ_0, φ_0. It is, however, temporarily ignore this latter effect as well as an elastic attenuation, i.e., the first term in the square bracket on the right hand side of Eq.(7.4). Then Eq.(7.4) becomes

$$\frac{\partial e}{\partial t} + c\frac{\partial e}{\partial x} = -n_s \gamma^{sca} c_e e \tag{7.6}$$

Using the Lagrangian relation $\frac{\partial}{\partial t} + c\frac{\partial}{\partial x} = c\frac{d}{ds}$ where s is a distance in which waves travel with a particular wavefront, then

$$\frac{de}{ds} = -n_s \gamma^{sca} e \quad ; \quad e = e_0 \cdot e^{(-n_s \gamma^{sca} s)} \; = e_0 e^{(-\frac{s}{l_s})} \tag{7.7}$$

where $l_s = \frac{1}{n_s \gamma^{sca}}$ is the scattering mean free path. The scattering mean free path defined above is the average distance energy travels before it is scattered, and is the characteristic scale length of the scattering process as mention before in chapter 3. Since γ^{sca} is a function of frequency, so is l_s; l_s may be greatly different for waves of different frequencies.

Let us now return to the case of a random wave field with energy travelling in all directions. The terms on the right hand side of Eq.(7.4) represent the exchange of the

energy through the scattering process between waves travelling in various directions. If the scattering is strong, however, and a time long compared with $\frac{l_s}{c_e}$ has passed, a radiation balance will be set up such that

$$-\int_S \Omega(\Theta)[e(\acute{\theta},\acute{\varphi}) - e(\theta,\varphi)]d\acute{\vartheta} \longrightarrow 0. \tag{7.8}$$

Eq.(7.8) demands that all of the energy be scattered energy. Eq.(7.4) may be further modified by noting that it is written in terms of $e(\vec{r},t,\theta,\varphi)$, which is not a measurable quantity if waves travelling in different directions can not be separated. Integrations over all angles will yield $\langle E(\vec{r},t)\rangle$, which is measurable. Performing the integration

$$\frac{\partial\langle E(\vec{r},t)\rangle}{\partial t} + \vec{\nabla}\cdot c_e\int_S \vec{k}e(\vec{r},t,\theta,\varphi)d\vartheta + \sigma\langle E(\vec{r},t)\rangle = 0 \tag{7.9}$$

To evaluate the second integral in Eq.(7.9), additional assumptions that at any points in the medium, under the influence of strong scattering, radiation is isotropic to zeroth order must be made. Then

$$\langle E(\vec{r},t)\rangle \;=\; \int_S e(\vec{r},t,\theta,\varphi)d\vartheta \;=\; 4\pi e(\vec{r},t). \tag{7.10}$$

Since energy travels a finite distance l_s before being scattered, the energy field can not be completely isotropic unless the energy field is also homogeneous. If a gradient of energy is present, slightly more energy will come from the up gradient direction than from the down gradient direction, because there is more energy present at a distance l_s in the up gradient direction. Using Eq.(7.10), then

$$e(\vec{r},t,\theta,\varphi) = \frac{1}{4\pi}(\langle E(\vec{r},t)\rangle + l_s\vec{n}\cdot\vec{\nabla}\langle E(\vec{r},t)\rangle) \tag{7.11}$$

Eq.(7.11) states that the energy seen at $\vec{r}$ has come from the surface of a sphere of radius l_s centered about $\vec{r}$. $\vec{n}$ in Eq.(7.11) is a unit vector from $\vec{r}$ pointing in the direction $180-\theta, 180+\varphi$. Thus $\vec{k} = -\vec{n}$ in Eq.(7.9). The remaining integral in the same equation now becomes two integrals, the first of which is

$$-\frac{1}{4\pi}\int_S \vec{n}\langle E(\vec{r},t)\rangle d\vartheta \;=\; -\frac{\langle E(\vec{r},t)\rangle}{4\pi}\int_S \vec{n}d\vartheta \;=\; 0 \tag{7.12}$$

The second integral is

$$-\frac{l_s}{4\pi}\int_S \vec{n}[\vec{n}\cdot\vec{\nabla}\langle E(\vec{r},t)\rangle]d\vartheta \;=\; -\frac{l_s}{3}\vec{\nabla}\langle E(\vec{r},t)\rangle. \tag{7.13}$$

Eq.(7.13) is derived by setting up a rectangular coordinate system with one axis, x, say along the direction of $\vec{\nabla}E(\vec{r},t)$. Contributions along the y and z axes then cancel by symmetry in the integration over the sphere. Substituting Eq.(7.12) and (7.13) in Eq.(7.9) to obtain

$$\frac{\partial\langle E(\vec{r},t)\rangle}{\partial t} = \frac{c_e l_s}{3}\nabla^2\langle E(\vec{r},t)\rangle - \sigma\langle E(\vec{r},t)\rangle \tag{7.14}$$

The parameter $\frac{c_e l_s}{3}$ will be written for the three-dimensional case as D, and is known as the diffusivity. The parameter σ is known as dissipation, as previously stated as a function of frequency. This derivation is similar to that used in the kinetic theory of gases [76].

The discussion above was for the acoustic case. In homogeneous elastic solids two types of waves, compressional and shear waves, exist. The diffusion equation as derived in acoustics may apply. The general diffusion equation found in many books [77], [78] and can be written as

$$\frac{\partial\langle E(x,t,f)\rangle}{\partial t} - D\ \triangle\langle E(x,t,f)\rangle + \sigma\langle E(x,t,f)\rangle = P(x,t,f)\ \forall x\in\mathcal{B} \tag{7.15}$$

where $\langle E(x,t,f)\rangle$ is spectral energy density (at time t and frequency f) at the point specified by the vector x, averaged over configurations of the media. $P(x,t,f)$ is the spectral source energy density, D denotes the frequency-dependent diffusion coefficient and $\sigma > 0$ is the dissipation rate.

If there is strong scattering (or scattering is isotropic), the compressional and shear waves will be coupled, and if the coupling is strong enough the two waves will locked

in to a radiation balance [70] which depends only on the properties of the scattering medium, provided that the time and distance scales of the problem are much longer than the corresponding scales for the scattering process. Thus, diffusivity and dissipation coefficients appear in Eq.(7.15) are directional independent.

7.3 Special solutions of the diffusion equation

Solutions for certain (common) geometries are derived. The frequency dependence of the coefficients σ, D and the energy density $\langle E \rangle$ is omitted in the reminder of this chapter.

7.3.1 One-dimensional bar

Eq.(7.15) is solved for a semi-infinite bar with an impulse excitation $P(x,t) = P_0\delta(t)\delta(x)$. The bar thickness is $t << L$, so the problem can be treated as one-dimensional with x as a scalar variable neglecting the wave propagation perpendicular to x. This leads to a simplified PDE.

$$\frac{\partial \langle E(x,t) \rangle}{\partial t} - D\frac{\partial^2 \langle E(x,t) \rangle}{\partial x^2} + \sigma \langle E(x,t) \rangle = P(x,t) \tag{7.16}$$

$$\frac{\partial \langle E(x,t) \rangle}{\partial x} \;=\; 0 \quad for\ x = 0 \tag{7.17}$$

The solution of this equations is given by

$$\langle E(x,t) \rangle = \frac{P_0}{2\sqrt{D\pi t}}\; e^{-x^2/(4Dt)}\; e^{-\sigma t} \tag{7.18}$$

This is the solution that Turner uses to model the diffusion of ultrasound in a 1-D geometry [19]. It has the big advantage that easy linear regression to measured data is possible after a logarithm is taken on both sides.

7.3.2 Circular disc with radius R

The Laplacian differential operator in cylindrical coordinates is written as follows.

$$\triangle E = \frac{1}{\rho}\frac{\partial}{\partial\rho}(\frac{\rho\,\partial E}{\partial\rho}) + \frac{1}{\rho^2}\frac{\partial^2 E}{\partial\phi^2} + \frac{\partial^2 E}{\partial z^2} \tag{7.19}$$

After plugging the transformation Eq.(7.19) into Eq.(7.15) and confining the development to the case of radial symmetry, a nonlinear PDE in the new coordinates r and z is obtained for the circular disc with radius R.

$$\frac{\partial\langle E(z,r,t)\rangle}{\partial t} - D(\frac{1}{r}\frac{\partial}{\partial r}(r\frac{\partial\langle E(z,r,t)\rangle}{\partial r}) + \frac{\partial^2\langle E(z,r,t)\rangle}{\partial z^2}) + \sigma\langle E(z,r,t)\rangle = P(z,r,t) \tag{7.20}$$

The two boundary conditions transform into one boundary condition on the flux at $r = R$ and the requirement that the solution $\langle E(z,r,t)\rangle$ has to be finite at $r = 0$. An analytic solution that satisfies these conditions is a infinite series involving Bessel functions.

$$\langle E(x,y,t)\rangle = \frac{P_0}{\pi R^2}[1 + \sum_{n=0}^{\infty} e^{-D\alpha_n^2 t}\frac{J_0(r\alpha_n)}{J_0^2(R\alpha_n) + J_1^2(R\alpha_n)}]\; e^{-\sigma t} \tag{7.21}$$

J_0 and J_1 denote the Bessel functions of zeroth and first order, α_n are the positive roots of $J_1(R\alpha) = 0$. Note the complex structure of the equation making it difficult to use it for a robust curve fitting procedure as it is needed later on.

7.3.3 Two-dimensional plate

Eq.(7.15) is solved in rectangular coordinate system (x, y) with an impulse excitation at the origin.

$$P(x,y,t) = P_0\delta(t)\delta(x)\delta(y) \tag{7.22}$$

The plate thickness is small relative to the plate size, therefore the gradient in z-direction is approximately equal to 0. The plate is assumed to have infinite extent

$(x \to \infty, y \to \infty)$. From this, a closed-form solution is easily found.

$$\langle E(x,y,t)\rangle = \frac{P_0}{4D\pi t}\, e^{-(x^2+y^2)/(4Dt)}\, e^{-\sigma t} \tag{7.23}$$

In Eq.(7.23), x^2+y^2 can be set to r^2 to clarify that this solution is radial symmetric.

Eqs. (7.18),(7.21), and (7.23) describe the form of the envelope with time at a given range of r, where P_0 is the power spectrum of the source. Curves based on these equations have been used in the studies of multiply scattered diffuse ultrasound. In this study, the solution of eq.(7.23) is used to approximate the ultrasound diffusion in the circular specimen of thickness b and varying entrained air void volume fraction. It is anticipated that the dissipation — the inverse equivalent measure of absorption attenuation, is only due to the matrix paste and not the entrained air voids. If this is true, the dissipation in Eq.(7.23) has to be dependent on the amount of cement paste matrix (unoccupied void space) in the specimen and that should be proportional to the fractions of the voids presence in the specimen as predicted early on using independent single scattering theory.

In the limit of many scattering events, laboratory diffusivities have been studied, it appears only few published for cement-based materials and deserves further investigation. While one imagines that D could be varied roughly as functions of frequency. Another objective of this study is to repeat the measurements such as that of Becker et al. [79]. The attempt to extract and study of D is envisioned as progress towards an eventual nondestructive implementation of measurements of scattering attenuation and the specific microstructure of cement-based materials.

7.4 Numerical time domain simulation of a diffusion process

To have a better understanding of how D and σ, coefficients affect the energy density $\langle E(r,t)\rangle$, variations of the D and σ are used in Eq. (7.23) to numerically simulate the energy density values. As can be seen from Fig.7.1, variations in dissipation σ (in $\frac{1}{s}$) lead to very different exponential decay at late times while diffusivity D (in $\frac{m^2}{s}$) lead more to changes at early times, including the edge rate and the delay in the arrival of the energy maximum caused by scattering. For this document, "edge rate" is meant to indicate the time for the diffusing energy to develop its maximum t_{max} and that time can be computed by differentiating Eq.(7.23) with respect to time and equated to zero. It follows that $t_{max} = \frac{1}{2\sigma}\{(1+\frac{\sigma r^2}{D})^{\frac{1}{2}} - 1\}$.

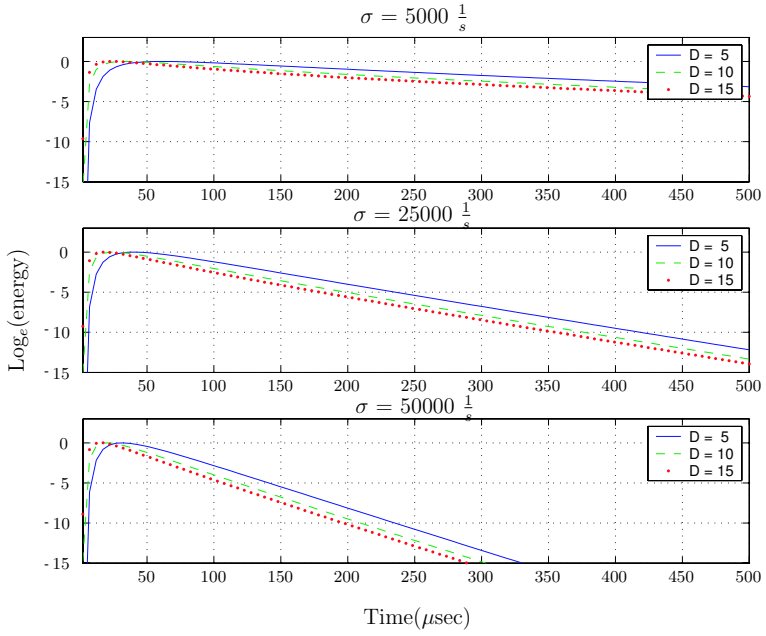

Figure 7.1: Results of the numerical experiment for the logarithm of energy density as a function of time, for different combinations of diffusivity D, and dissipation σ values

7.5 Benchmark experiments

To test the applicability of the diffusion equation to ultrasonic energy propagation in heterogeneous cement-based materials a set of ultrasonic diffuse measurements was carried out in the laboratory. The experiments used the propagation of ultrasonic pulses in two cement paste specimens made of a cement paste matrix with and without entrained air voids. Both specimens were circular in shape with diameter of 100 mm and thicknesses of about 20 mm. The model scatterers consisted of randomly distributed spherical entrained air voids (with diameter smaller than the dominant wavelength). The preparation of these specimens was described earlier in Chapter 5 section 5.4 and shall not be repeated here. The cement paste matrix was used to simulate the effect of viscoelastic properties of cement-based materials onto the dissipation. An addition of entrained air voids (or scatterers) into the matrix simulates the effect of scattering as well as a reduction of dissipation.

A schematic diagram of the experimental setup is shown in chapter 4, section 4.2.2. In brief, a pulse of approximately 1.5 μs duration is generated by the pulse generator and applied to the specimen by the LC50-5 source transducer. A digital wave B1025 receiving transducer is mounted at the opposite side and measured 40 mm off the center from the source transducer. The bandwidth of the source and receiver transducer combination is from 0.45 to 3.0 MHz and that gives the center frequency of about 1.7 MHz which corresponds to the wavelength of about 2 mm.

A 1 x 1 mm contact pad was attached on the receiving transducer surface prior to the mounting. This is to enable point-like detection. This process is to eliminate the effects of having more than one speckle impinge on the transducer, while retaining the good sensitivity of piezoelectric transducers [73],[79]. The multiply scattered diffuse

ultrasonic field is recorded with 30000 points at 25 MHz sampling rate. This corresponds to the total time of 1200 μs. Due to both the presence of intrinsic absorption, and to the dilution of volumetric distribution of entrained air voids, measured diffuse field signals are expected to be weaker, meaning electronic noise can be a problem. In order to improve the signal to noise ratios, the repetitive signals were averages, as much as 500 times during the acquisition on a digital oscilloscope. According to a simple calculation, this averaging procedure reduces the noise power level by $\log_e(500) = 6.2$ nepers of power (or 27 dB) and increased the signal to noise ratio by the same amount.

7.5.1 Calculation of energy density and fitting procedure

A typical typical recorded time domain signal obtained from the ultrasonic model experiment is shown in Fig. 7.2. As described in Becker [79], this waveform may be inverted for the three parameters σ, D, and P_0 by performing a time-frequency analysis for its fit to the solution of diffusion equation.

7.5.1.1 Time-frequency analysis for energy density estimation

The waveform such as one shown in Fig. 7.2 is first divided into several overlapping time windows (Δt $= 60\mu$s each with overlapping of $75 - 90$ %). Each time window is given smoothed edge with a Hanning window, as the one shown in Fig. 7.3, [53] and separately calculate the Discrete Fourier Transform. For each overlapping time-window the power spectrum is then squared and integrate over the frequency bin of arbitrary width (Δf $= 0.2$ MHz). The result is a quantity proportion to the energy at the center band frequency f_c as a function of time, $\hat{E}(r, t, f)$. $\hat{E}(r, t, f)$ is not precisely ultrasonic energy density $\langle E(r, t, f)\rangle$, but differs from that by a factor related to transducer efficiency, coupling effect, influence of the time-frequency analysis parameters.

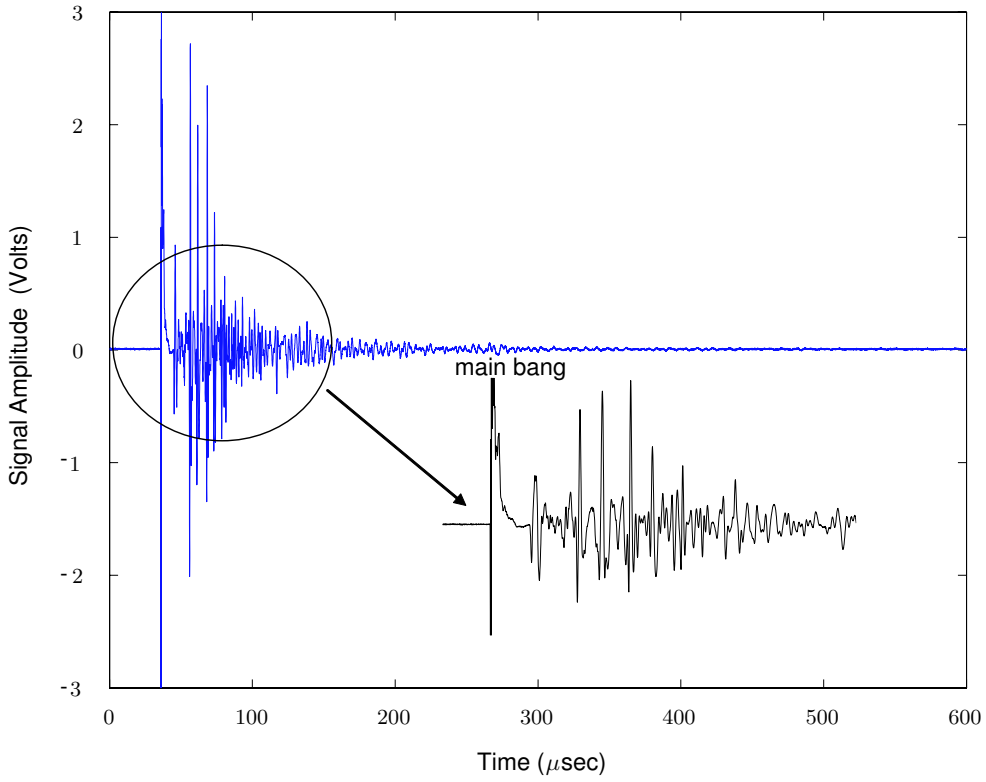

Figure 7.2: The first 600 μs of a 500 repetition average diffuse response of a cement paste specimen. Also shown insert, is the zoom in to time 100μs

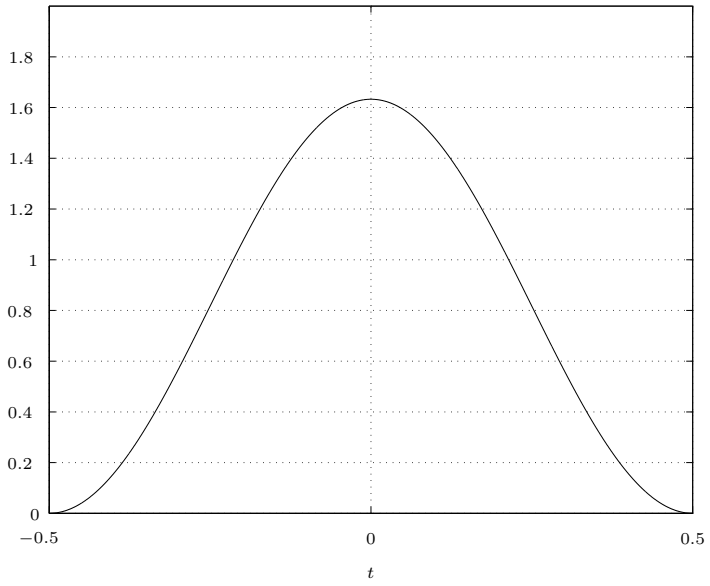

Figure 7.3: A normalized Hanning window

For example, it has been shown that the measured $\hat{E}(r,t,f)$ fluctuates away from $\langle E(r,t,f)\rangle$ by one part of the square root of the product Δt and Δf [79], [80]. For the results presented in this chapter, $\Delta t = 60\mu$s and $\triangle f = 0.25$ MHz, such that the $\langle E(r,t,f)\rangle$ should be differ from $\hat{E}(r,t,f)$ by the factor of $\pm 1/\sqrt{(\triangle t \triangle f)} = \pm 25\%$. The fluctuations are reducible by increasing Δt and/or Δf. However, an increasing proportion of Δt and Δf lead to loss of time as well as frequency resolution, and hence decreases the quality of the diffusion model parameters when performing a fit to the data.

7.5.1.2 Fitting Procedure

By taking the natural logarithm, the Eq.(7.23) can be linearized. Then Eq.(7.23) becomes

$$\log_e \langle E(r,t)\rangle + \log_e t = A + Bt + C/t \tag{7.24}$$

with

$$A = \log_e(\frac{P_0}{4\pi D}), \tag{7.25}$$

$$B = -\sigma, \tag{7.26}$$

$$C = -\frac{r^2}{4D} \tag{7.27}$$

If the spectral energy density $\hat{E}$ can be measured for time $t > 0$ at a reference distance r and at a certain frequency f then the quantity $\log_e\langle\hat{E}\rangle + \log_e$t depends only linearly on the three base function 1, t and 1/t. Applying the standard method of least squares [81] the three unknown parameters A, B, and C can be computed. After the inversion, the parameters D, σ, and P_0 (or α_a, α_s, and P_0) are calculated from A, B, and C. The first two parameters D and σ are sensitive to the material losses whereas the third parameter P_0 is highly related to the measurement related factors and thus P_0 obtained from the calculations will not be addressed.

Figure 7.4 shows a typical plot of the tabulated observed energies ($\log_e$(energy)), versus time for each of several frequency bins. Superimposed on the scatter plot in the same figure is the best-fit solution to the two dimensional diffusion equation. The expected deviations (as calculated and mentioned in section 7.5.1.1) are also plotted as bars at some points on the curves and they are all the same for all points.

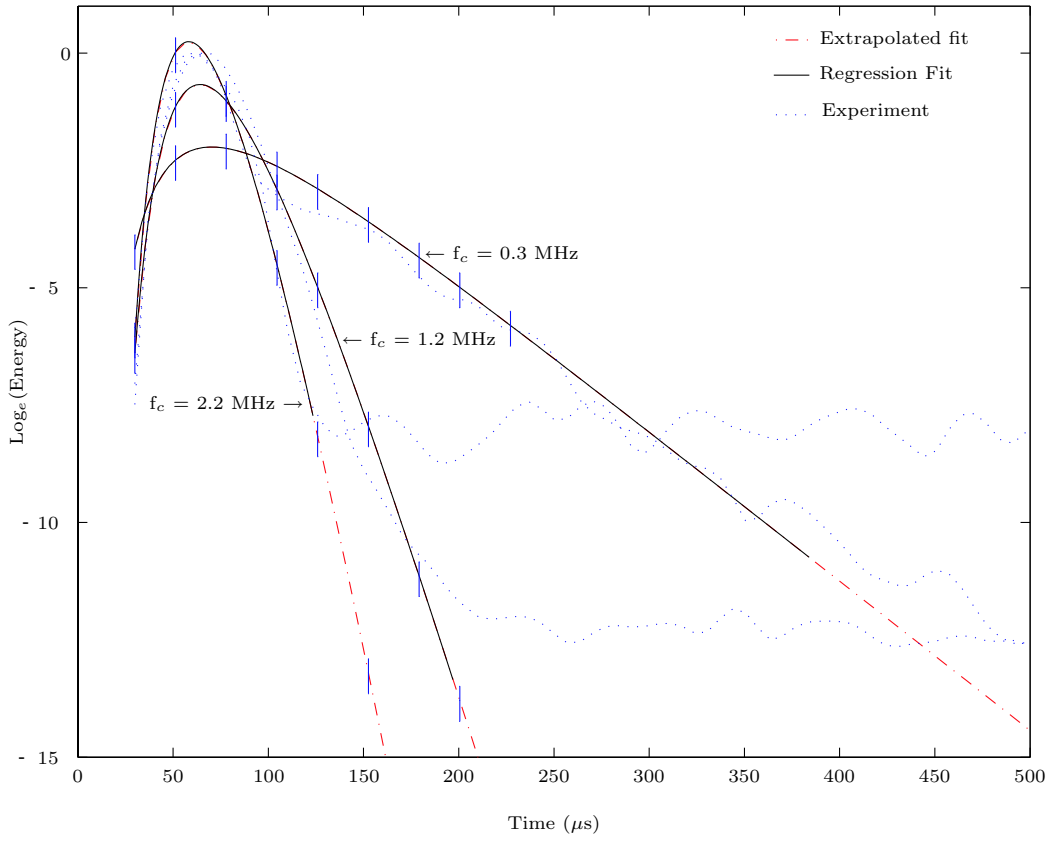

Figure 7.4: Experimental energy envelopes (dot curves) and theoretical fits to a two-dimensional diffusion equation (dashed curves) for the cement paste specimen at f$_c$ = 0.3, 1.2, and 2.2 MHz. Bars show plus/minus expected deviations based on the product of Δt and Δf

.

7.5.2 Evaluation and discussion of the recovered diffusion parameters

The ultrasonic diffusion experiments were conducted on cement paste and entrained air cement paste specimens having the same water to cement mass ratio of 0.4. Experimental waveforms were collected from five locations where $r = 40$ mm. Dissipation σ and diffusivities D were then calculated from experimental data by fitting the energy curves to solutions of the two dimensional model partial differential equation. Figure 7.5 shows the five locations of the energy curve fits. The time range used for energy curves fitting at certain frequencies are listed in Table 7.1. For each specimen, the recovered dissipation σ as well as diffusivity D were plotted and shown as a function of frequency (see Fig.7.6 and 7.7). It should be noted that not all values are displayed for all specimens. The missing points are for cases where data did not allow reliable or consistent estimates of dissipation σ and diffusivity D especially in the frequency range above 2.25 MHz. As was hypothesized earlier, if dissipation and diffusivity were all influenced by material microstructure then the dissipation σ and diffusivity D values observed in one specimen should be different from another. A comparison of the average σ and D values obtained from these plots will be used and discussed towards the final conclusion.

Table 7.1: Time windows used for energy curves fitting for all specimens

f_c (MHz)	t_{start} (μs)	t_{end} (μs)	f_{center} (MHz)	t_{start} (μs)	t_{end} (μs)
0.2	8	430	1.6	8	135
0.4	8	350	1.8	8	120
0.6	8	265	2.0	8	120
0.8	8	235	2.2	8	120
1.0	8	210	2.4	8	100
1.2	8	190	2.6	8	90
1.4	8	165	2.8	8	70

7.5.2.1 Dissipation

Figure 7.8 compares the average dissipation values recovered from the five locations on the two specimens. Both specimens clearly show dissipation increase linearly with increasing frequency. The cement paste specimen has higher recovered dissipation values than the entrained air cement paste specimen. This observation is rather important, since it confirms the earlier findings — the major factor of the attenuation in cement paste specimen is the viscoelastic absorption in the cement paste matrix, so that the entrained air cement paste, when entrained by air voids, yields lower attenuation than the cement paste matrix. It is proposed here that the total volume fraction of air voids (whether entrained or entrapped air voids existing in addition to the cement paste) can be estimated by 1 - the ratio of the two dissipation slopes. That is equal to $1 - 0.93 = 0.07$ or about 7% by volume. This result is consistent with the result obtained from previous chapter and it suggests that the dissipation parameter is sensitive to the total air content rather than the entrained air void content alone.

7.5.2.2 Diffusivity

Figure 7.9 shows a comparison of diffusivity values recovered from the two specimen. Notice that diffusivity decreases with increasing frequency, the decreased diffusivity means decreased mean free path; it also means higher probability of scattering. Thus, stronger scattering is indicated at higher frequencies than at lower frequencies. The two specimens show different diffusivities, with entrained air cement paste exhibiting lower than the cement paste specimen. Thus, ultrasonic waves are more scattered in the former specimen than in the latter. This observation is consistent with diffusion theory since a larger number of voids means stronger scattering and thus, a further delayed energy propagation. The observation is also a good indicator of heterogeneity. Diffusivity values indicate that entrained air cement paste is structurally more

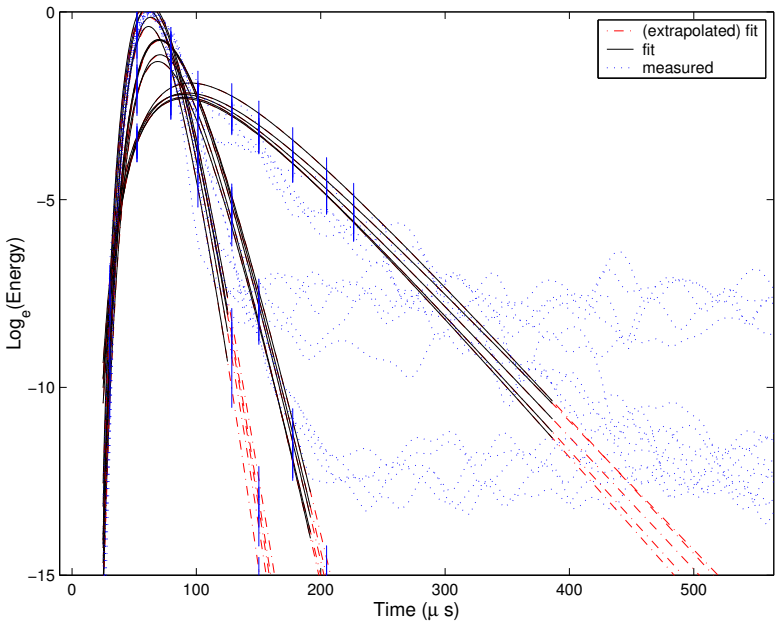

(a) Cement paste specimen

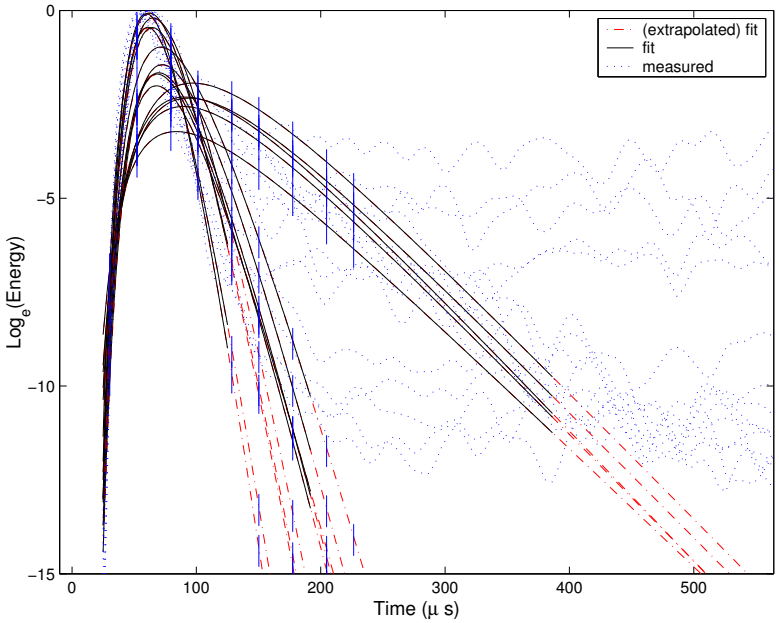

(b) Entrained air cement paste specimen

Figure 7.5: The five locations of the energy curve fits for (a) cement paste and (b) entrained air cement paste specimen at f_c = 0.3, 1.2, and 2.2 MHz.

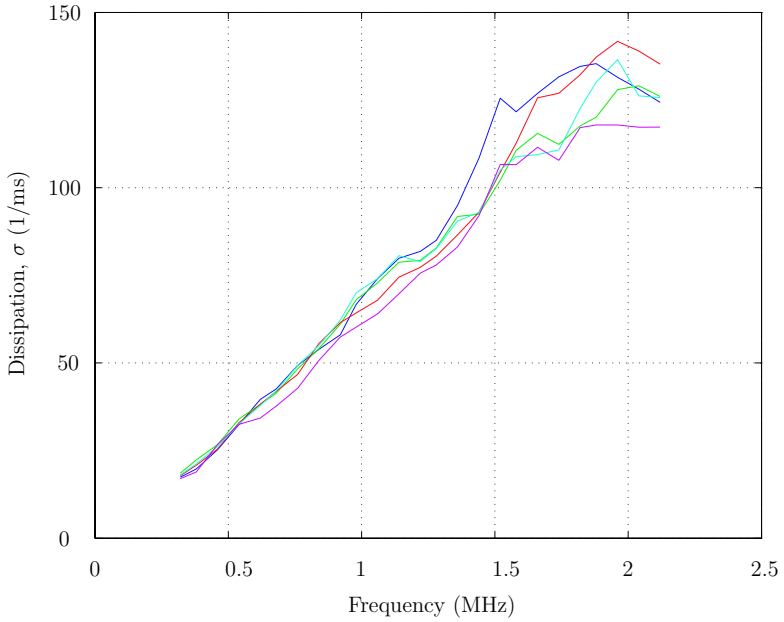

(a) Dissipation, σ (1/ms)

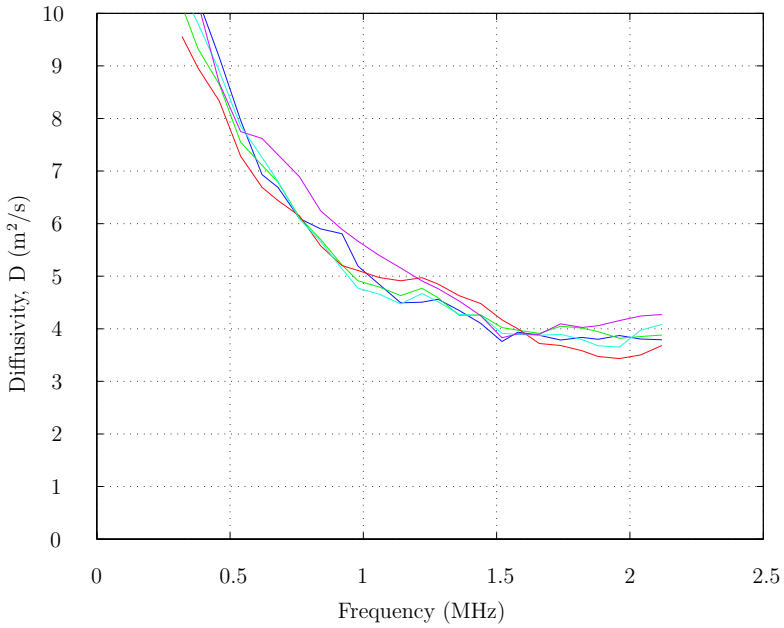

(b) Diffusivity, D (m^2/s)

Figure 7.6: Recovered diffuse parameters (a) dissipation, (b) diffusivity from cement paste specimen

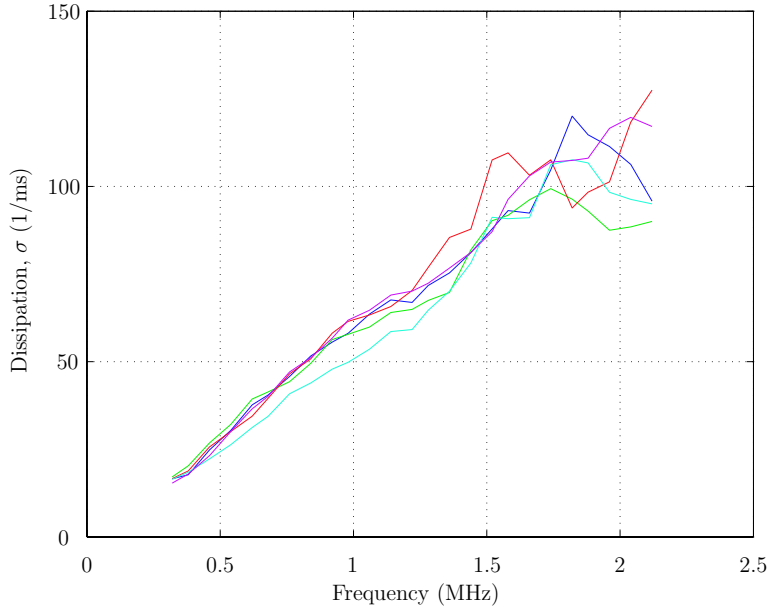

(a) Dissipation, σ (1/ms)

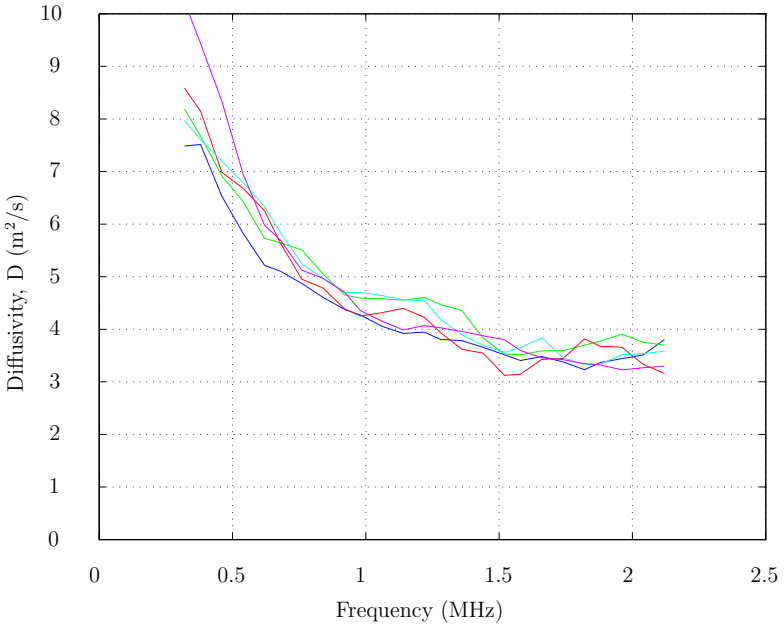

(b) Diffusivity, D (m^2/s)

Figure 7.7: Recovered diffuse parameters (a) dissipation, (b) diffusivity from entrained air cement paste specimen

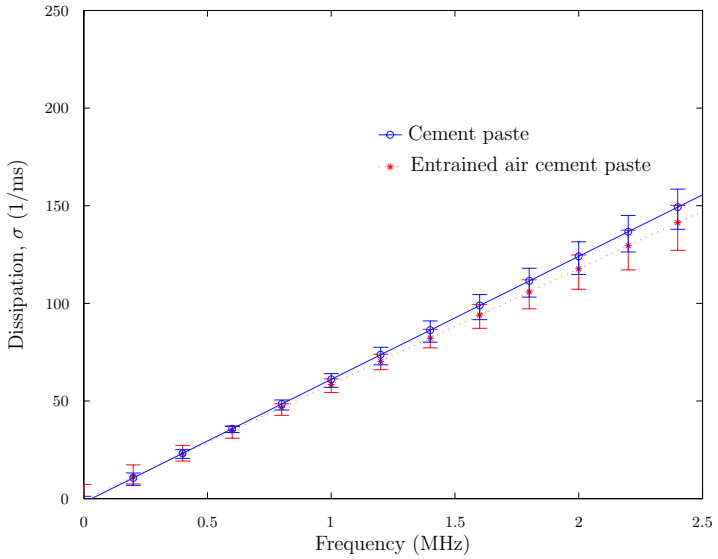

Figure 7.8: Comparison of averaged values of dissipation σ recovered from cement paste and entrained air cement paste specimen

heterogeneous (more scatterers per unit area) than the homogeneous cement paste. This difference is obviously resulted from the difference in the presence of entrained air voids in the cement paste microstructure.

7.5.3 Intrinsic absorption in relation to the dissipation

The intrinsic absorption of a material can be directly to specific material features; this relationship has been extensively studied in polymers and tissues, where internal friction and viscoelastic dissipation losses dominate. If dissipation σ is a measure of the intrinsic absorption (as convinced by its linear frequency dependency behavior observed from the benchmark measurement) then dimensional analysis suggests that dissipation, σ, is related to the intrinsic material absorption coefficient,α_a, by $\alpha_a = \frac{\sigma}{c}$, where c is the average wave speed of the diffuse wave field measured by the point detector. It is further assumed that the source transducer produces a wave field which is predominantly longitudinal, the overall diffuse wave field is dominated by the

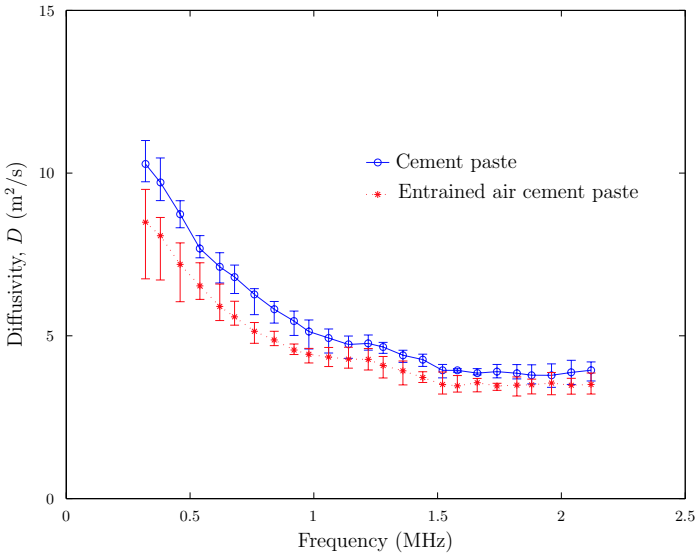

Figure 7.9: Comparison of averaged values of diffusivity D recovered from cement paste and entrained air cement paste specimen

phase velocity of the longitudinal wave. Coherent measurement (referred to Table 5.1 and Fig. 5.6 in chapter 5) measures the phase velocity of longitudinal waves in the cement paste specimen as 3750 m/s for the frequency range of interest (with limited dispersion), so the dissipation values are converted to intrinsic absorption coefficient and compared to the corresponding absorption attenuation directly with the corresponding absorption attenuation directly measured with a coherent measurement technique; these results are shown in Fig. 7.10. There is good agreement between the two values, which suggests that dissipation, σ, can be used as an equivalent measure of intrinsic (material) absorption attenuation when the phase velocity is known.

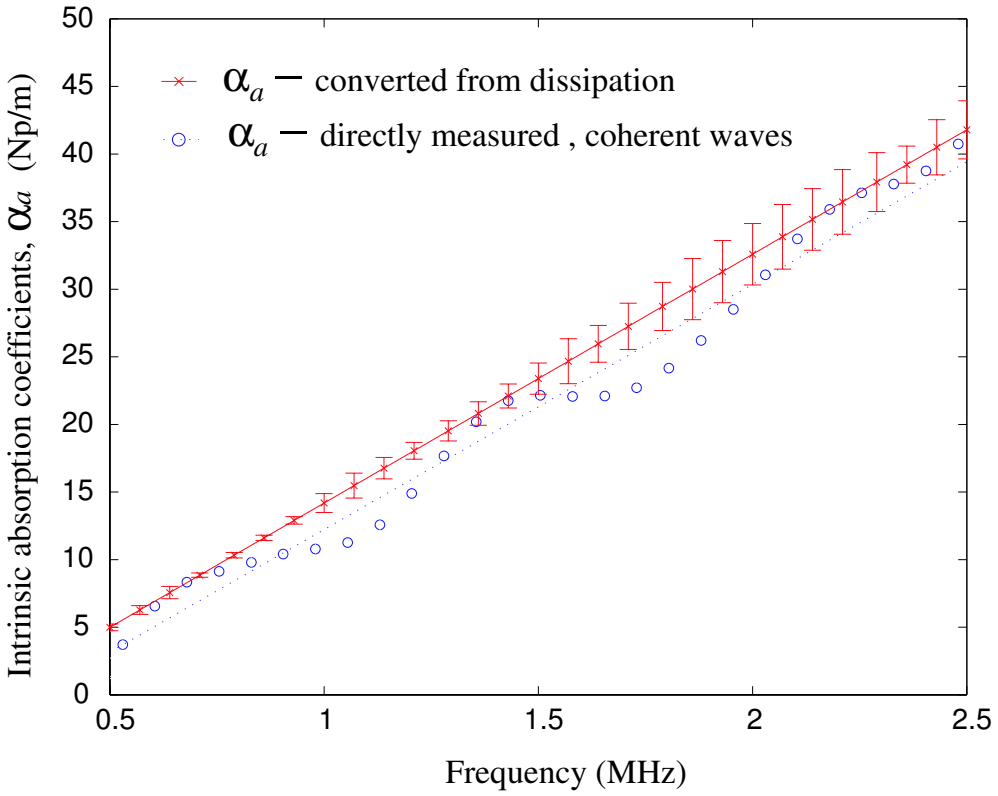

Figure 7.10: Comparison of the directly measured absorption attenuation (coherent) and the corresponding value calculated with the measured dissipation and phase velocity

7.6 Effect of cement-based material microstructure on diffusion parameters

Using the knowledge obtained from the benchmark measurement, the ultrasonic diffusion experiments were conducted on the seven specimens previously undergone coherent attenuation measurement testing. The description of these specimens were described in chapter 6, section 6.1. Experimental waveforms were collected and analyzed to obtain the average dissipation σ, and diffusivity D values following the approach given in section 7.5 with exactly the same time-frequency analysis parameters. As was hypothesized and shown earlier in the benchmark experiment that

dissipation σ and diffusivity D values observed in the benchmark specimens were all influenced by the microstructure of hardened cement paste. It is expected that the dissipation σ and diffusivity D values are observed to be different as going from one specimen microstructure to the other. A comparative discussion of these results is provided in the subsequent section.

7.6.1 Effect of entrained air voids and w/c ratio on dissipation

Figure 7.11(a) compares the variation of average dissipation values (in 1/millisecond) vs frequency curve (in MHz) of material systems CP2, EACP1, EACP2 and EACP3. These specimens contain different amounts of entrained air voids and share the same w/c of 0.4. In all cases of Fig 7.11(b), linear regression for frequencies 0.3-2.2 MHz shows dissipation values increase linearly with increasing frequency. The CP2 cement paste specimen made with zero percent entrained air content exhibits the highest recovered dissipation values. All other EACP specimens show different dissipation values, with the EACP1, EACP2, and EACP3 exhibiting 5.5%,10.2%, and 13.9% lower than the CP2. Since the specimens were cast in the same manner and should have approximately the same volume. This observation is a strong indication that the addition of entrained air voids in the cement paste matrix decreases energy dissipation. This experimental observation supports the mathematically derived theoretical explanation of the attenuation model previously discussed in chapter 5 as it is shown earlier in chapter 6 that the measure of dissipation could be used as the equivalent measure of the absorption attenuation coefficient.

The case concerning water content influence on dissipation is also depicted here. The

measured dissipation coefficients for specimens CP1, CP2, CP3 and CP4 are plotted as functions of frequency and shown in Fig. 7.12(a). Linear regression of these data for frequencies 0.3- 2.25 MHz shows very good linear dissipation dependence of frequency and that is shown in Fig. 7.12(b). From this figure, CP1 specimen which has the lowest w/c ratio of 0.3 shows the highest and steepest lineal slopes in the energy dissipation curve while others exhibit in similar fashion but lower values (CP1>CP2>CP3>CP4) as the w/c ratio increases. In trying to explain these results, the effect of the irregular capillary void comes first to mind. Under Power's phenomenological model, capillary voids are governed by w/c ratio and by the degree of hydration. Capillary porosity is lower for cement paste with low w/c ratios. It is plausible that more of these capillary voids cause stronger decrease of the dissipation. While this is a good indicator of the presence of the capillary voids, no quantitative conclusions are drawn from these results because specimens are expected to be different as going from one to the other.

Finally, if dissipation is a measure of the intrinsic viscoelastic losses in the cement paste then dimensional analysis suggests that dissipation, σ, is related to the absorption attenuation coefficient, α_a, by $\alpha_a = \sigma/c$, where c is the average wave speed of the diffuse wave field measured by the point detector. If it's assumed that the source transducer produces a wavefield which is dominated by the phase velocity of the longitudinal wave. Using the method by previous research [82], the phase velocity values of longitudinal waves in the CP1, CP2, CP3, and CP4 are measured for the frequency range of interest. The measurement results are plotted and shown in Fig. 7.13(a). Using these phase velocity values, the dissipation values are converted to the intrinsic absorption and these should be compared to the corresponding absorption attenuation directly measured with a coherent measurement as presented earlier in Fig. 6.3; these results are shown in Fig. 7.13(b). Obviously, the values obtained

from the conversion do not match perfectly with the values obtained from the coherent measurement on one-to-one basis however they follow the same trend. That is the CP4 specimen (w/c=0.6) shows the highest absorption attenuation while CP1 (w/c=0.3) shows the lowest absorption attenuation. The difference of the two values may be due to the measurement variation of phase velocity. By default, a similar trend suggests that dissipation, σ can be used as an equivalent measure of intrinsic (material) absorption attenuation when the phase velocity is known.

7.6.2 Effect of entrained air voids and w/c ratio on diffusivity

The effect of entrained air voids on diffusivity is depicted in Fig. 7.14. A systematic pattern of lower diffusivity values for the EACP specimens when compared to the CP2 specimen is observed in this figure. Thus, ultrasonic waves are more scattered in the former case than in the latter, indicating that all EACP specimens are structurally more heterogeneous than the CP2 specimen.

This difference may have resulted from the differences in either the entrained air void size or the entrained air void content in the volume of the EACP specimens. It is obvious from the measurements that the entrained air void sizes are more distinguishable by the diffusivity. This is convinced by reasons that the diffusivity values in the EACP1 and EACP2 are very close to each other and the diffusivity values obtained from EACP3 specimen are more separable from the other two — the separation of the two curves is more than 10% as opposed to the results reported in the coherent measurement section.

The effect of w/c ratio on diffusivity is considered in Fig. 7.15. No systematic effects were seen as a function of w/c ratio. The almost equal diffusivity values for the CP1, CP2, CP3 and CP4 suggests that the apparent difference in diffusive wave characteristics between the specimens seems to be primarily a difference in the dissipation characteristics of specimen rather than a difference in degree of scattering. No quantitative conclusions are drawn from these diffusivity results; these diffusivity results are most likely dominated by the multiple reflections off of the specimen boundaries, as opposed to scattering from the microstructure. This finding supports the contention that the microstructure of CP1, CP2, CP3, and CP4 specimens, which is mainly controlled by w/c, does not exercise significant influence on scattering but on absorption.

7.7 Summary

The heterogeneous structure of cement paste is studied using an active diffuse ultrasonic experiment. The addition of entrained air voids, even with a small amount, forms strong impedance contrasts for ultrasonic waves and causes scattering effects.

Diffuse signals obtained from the experiment indicate strong scattering and the transmission of scattered energy is governed by a diffusion equation with frequency dependent dissipation and diffusivity. A time-frequency analysis combining with statistical approach is applied to interpret these signals.

It is shown in this research that it is possible to calculate dissipation σ and diffusivities D from experimental data by fitting the energy curves to solutions of the two dimensional diffusion equation. The results show a linear dependency on frequency for energy dissipation; this behavior is similar to that of a polymer (hysteresis absorption) and is primary due to intrinsic viscoelastic losses in the cement paste. There is also a reasonable correlation between these dissipation losses and the amount of cement paste present in a sample. The measured diffusivity show qualitative trends, but not that robust. Diffusivity has a limited capability to resolve variations in cement paste microstructure.

Overall, the application of diffuse field measurements provides a basic understanding of the effect of microstructure of cement-based materials, supplying a first step in the characterization of cement-based materials of microstructure of the cement-based materials.

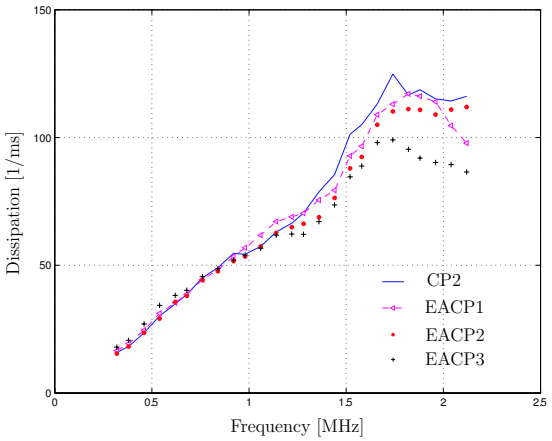

(a) Averaged, recovered dissipation, σ

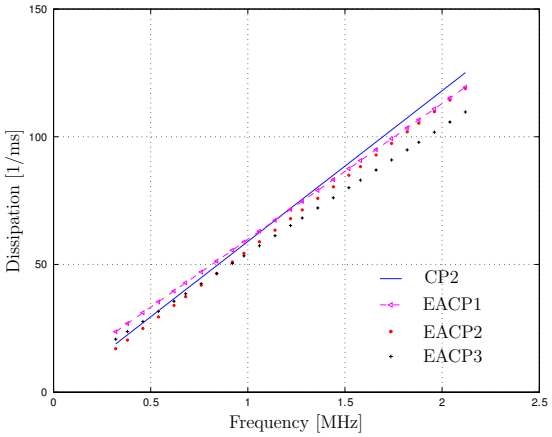

(b) Linear regression fit

Figure 7.11: Dissipation comparison for specimens with different entrained air content

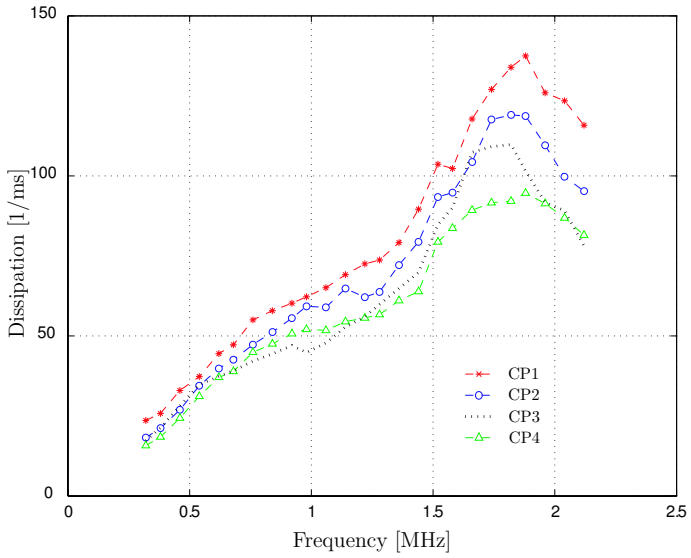

(a) Averaged, recovered dissipation, σ

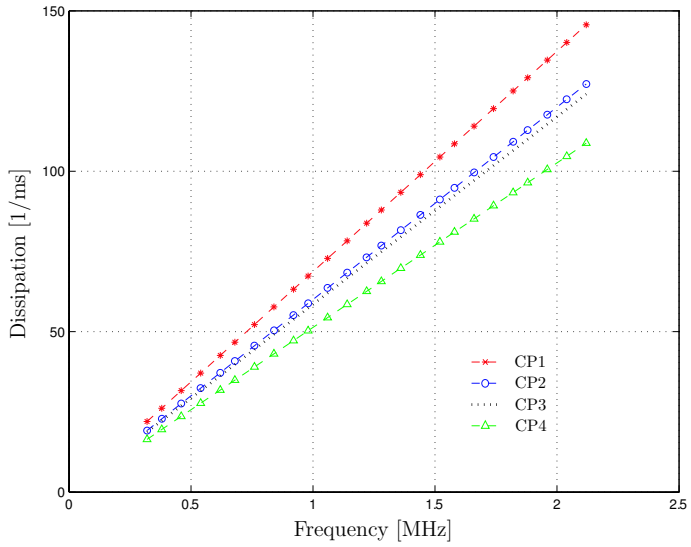

(b) Linear regression fit

Figure 7.12: Dissipation comparison for specimens with different w/c ratio

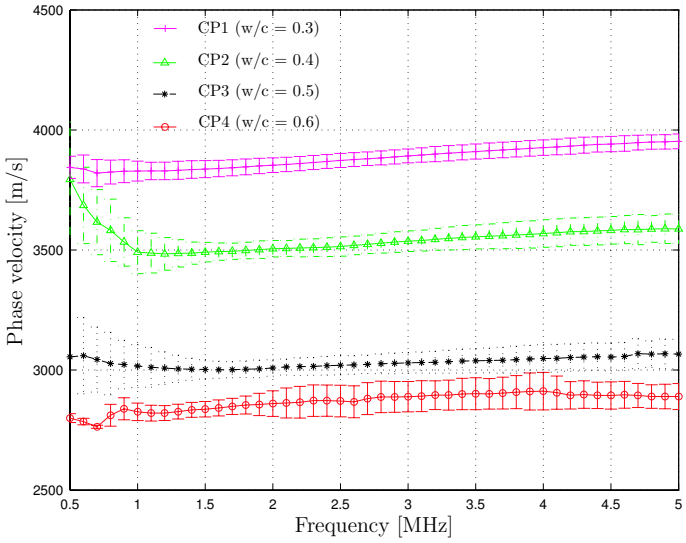

(a) Phase velocities determined with coherent measurement.

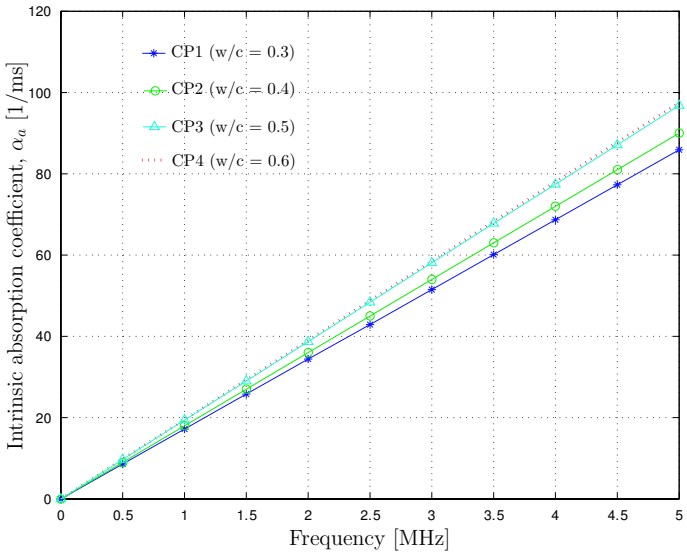

(b) Absorption values calculated with the measured dissipation and phase velocity.

Figure 7.13: (a) Phase velocities (coherent measurement) and (b) absorption attenuation values calculated with the measured dissipation and phase velocity for specimens with different w/c ratio

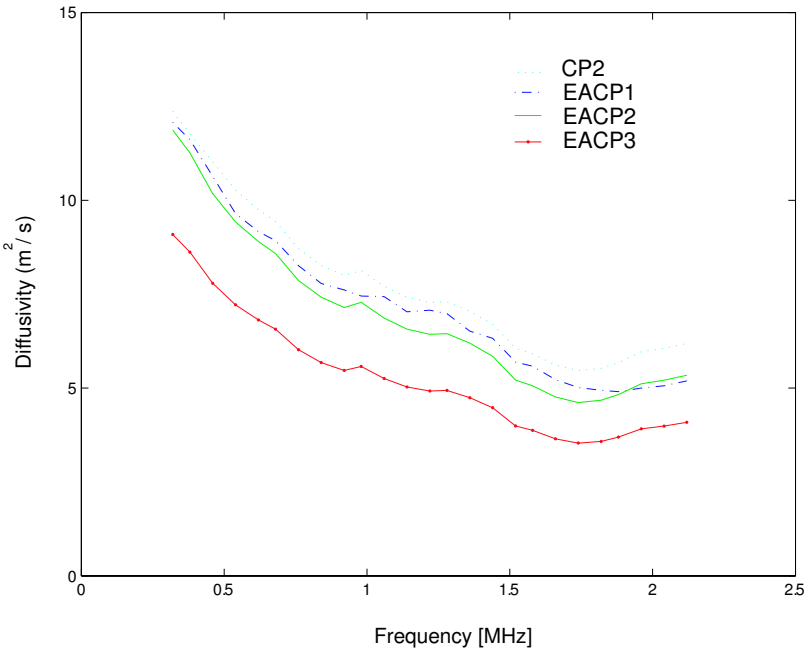

Figure 7.14: Averaged diffusivity of the CP2, EACP1, EACP2, and EACP3 specimens

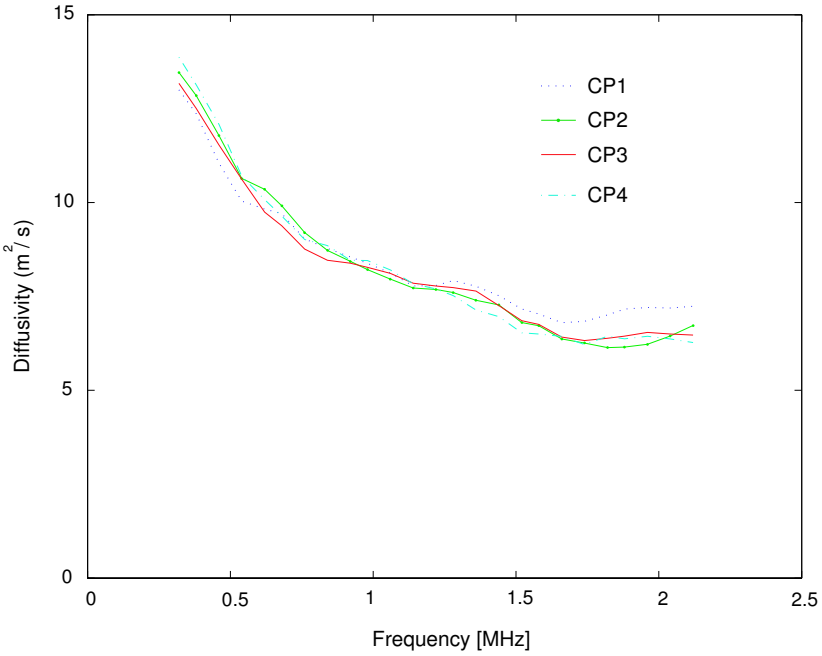

Figure 7.15: Averaged diffusivity of the CP1, CP2, CP3, and CP4 specimens

CHAPTER 8

Conclusions and recommendations

This research demonstrates the effectiveness of using ultrasonic attenuation measurement to characterize cement-based materials. The results of the studies further the comprehension of the underlying mechanics of ultrasonic attenuation in cement-based materials.

Chapter 5 reports attenuation characteristics of longitudinal ultrasonic waves in entrained air hardened cement paste. Benchmark experimental results obtained from coherent measurements have been analyzed based on a theoretical estimation of scattering as well as absorption losses, with explicit consideration of viscoelastic properties of cement paste matrix. The simplistic independent scattering/absorption approximation has been employed in the numerical analysis in order to gain first insight into ultrasonic wave attenuation in entrained air hardened cement paste, its dependence on frequency, entrained air void size and volume fraction. The numerical results show the capability of the model in predicting entrained air void size and volume fraction. A minimization of the sum squared between the model and the experiments using the Nelder-Mead downhill simplex algorithm results in a reasonable estimate of entrained air void size and volume fraction. It is important to note that the model that is used on this study assumes spherical inclusions and does not account for any possible distribution of different air void sizes, although it is shown in reality that air voids in hardened cement paste are not all of the same size but instead will have a

certain statistical distribution. By taking into account a distribution of two dominant void sizes – entrained and entrapped air voids (each having a normal distribution), it is demonstrated that there is a much better agreement between the theoretical prediction and the experimental measured attenuation especially in the low megahertz frequency range. A future work could include a cumulative frequency distribution of void sizes, fractions into the inversion algorithm for a more robust techniques.

In chapter 6, the results of an experimental investigation quantify attenuation in seven different cement paste specimens, each consisting of a different structural morphology, are presented. Within a given material, there is considerability variability in attenuation for different material volumes and that is due to the randomness and variability present in cement paste. For systems of entrained air void in hardened cement paste, the predominate attenuation feature observed in these experiments is that scattering losses caused by air voids are not negligible when compared to the absorption losses present. The use of well established scattering models enables the use of the quantitative attenuation technique to accurately measure the entrained air void microstructure of cement paste. The study also shows the dominant role of the hardened cement paste microstructure (in the absence of entrained air voids), which is controlled by w/c, in ultrasonic wave propagation affecting absorption attenuation. This trend corresponds to the expected behavior similar to polymer and tissues. The phenomenological model is used in this study to indicate the microstructural contribution in relation to the ultrasonic absorption mechanism. Further theoretical studies could lead to the more effective measuring w/c ratio technique.

Chapter 7 explores the application of the diffusion approximation and diffusion theory to the measurement of ultrasound attenuation in hardened cement paste specimens.

Specimens previously used in chapter 6 were undergone diffuse ultrasonic model experiments. Not only the study shows that it is possible to quantify the dissipation losses in cement paste both with and with out entrained air voids but these dissipation values are shown to be relatively robust to quantify differences in microstructure such as the existence of entrained air voids. More importantly, it is shown that these dissipation values can be related to the absorption attenuation values measured with a coherent ultrasound procedure (if the phase velocity is known). The results show a linear dependency on frequency for energy dissipation which is similar to that of a polymer (hysteresis absorption) and is primarily due to the intrinsic viscoelastic losses in cement paste. A reasonable correlation between these dissipation losses and the amount of cement paste present in a sample is reported. The measured diffusivity values also show qualitative trends. The results from test specimens show different diffusivity values with entrained air cement paste specimen exhibiting lower than the cement paste specimen. Lower diffusivity means higher probability of scattering. Thus, the values are capable of differentiating the specimens. It is however uncertain if the diffusion values obtained can be used to resolve variations in size and volume fraction of entrained air voids. Further studies should examine the connection between this parameter and some type of statistical approach which can then be related to the information about void size and distribution.

Given the obtained promising results for cement paste, further studies are necessary to establish the nondestructive measurement that could be useful for the characterization of concrete structure in situ.

Appendix A

The calculation of cross section expressions for the scattering of a plane longitudinal wave by a spherical cavity

The formal analysis of elastic waves scattering by a spherical obstacle has been given by Ying and Truell [57]. Therefore, those equations can be directly adopted.

A.1 Representation of waves and solution of equations of motion

Consider a plane, simple harmonic wave, has a unit of amplitude and propagates in the positive direction of the z-axis. This wave can be described by the simple displacement expression,

$$u = \bar{u_i} e^{i\omega t} \tag{A.1}$$

where u_i is a function of the spatial coordinates only (e.g. $\bar{z}e^{-ikz}$), ω is the angular frequency, $\bar{u_i}$ is a unit vector in the positive direction of the z-axis, k is the wave number and ρ is the density of the medium.

On using the spherical coordinates with origin at the center of the sphere, the z-axis is the axis of symmetry for all the waves. Then the solution of the equation of motion

for a general displacement u in an isotropic medium can be written as

$$u = -\nabla\Psi + \nabla \times [\nabla \times (r\Pi)], \tag{A.2}$$

where the potentials $\Psi = \Psi(r, \theta)$ and $\Pi = \Pi(r, \theta)$ represent the longitudinal and transverse parts of the waves and satisfy the equations

$$(\nabla^2 + k^2)\Psi = 0 \;\; ; \;\; (\nabla^2 + \kappa^2)\Psi = 0 \tag{A.3}$$

with

$$k = \omega(\frac{\rho}{\lambda + 2\mu})^{\frac{1}{2}} \;\; ; \;\; \kappa = \omega(\frac{\rho}{\mu})^{\frac{1}{2}} \tag{A.4}$$

Here k and κ are the longitudinal and shear wave numbers in the medium surrounding the cavity. λ and μ are the second order Lam*é* constants of the medium.

Assuming an incident longitudinal wave, the solution to the wave equation is assumed to be of the form

$$\Psi_i = \frac{1}{k}\sum_{m=0}^{\infty}(-i)^{m+1}(2m+1)j_m(kr)P_m(\cos\theta) \quad ; \quad \Pi_i = 0 \tag{A.5}$$

where $j_m(\xi)$ is the spherical Bessel function of the first kind of order m, P_m is the Legendre polynomial of degree m.

When a travelling wave impinges on the cavity, scattering occurs. Subsequently, the scattered wave potentials may be written as

$$\begin{aligned} \Psi_s &= \sum_{m=0}^{\infty} A_m h_m(kr)P_m(\cos\theta) \\ \Pi_s &= \sum_{m=0}^{\infty} B_m h_m(\kappa r)P_m(\cos\theta) \end{aligned} \tag{A.6}$$

Here $h_m(\xi)$ is the abbreviation of $h_m^{(2)}(\xi)$ and is spherical Bessel function of the third kind:

$$h_m(\xi) = (\frac{\pi}{2})^{\frac{1}{2}}\frac{H_{m+\frac{1}{2}}{}^{(2)}(\xi)}{\sqrt{(}\xi)} \tag{A.7}$$

Here $H_{m+\frac{1}{2}}{}^{(2)}(\xi)$ being the Bessel function of the third kind.

In choosing these forms of the expressions for the scattered wave, it has been borne in mind that for large r one has

$$\Psi_s, \Pi_s \sim \frac{e^{-ikr}}{kr}, \tag{A.8}$$

which represents an outgoing simple harmonic spherical wave, as to be physically expected. Noting that there are two sets of unknown coefficients — A_m and B_m that have to be determined from the boundary conditions. In the case of a spherical cavity of radius a, the boundary conditions at $r = a$ are

$$\sigma_{rr}{}^{(i)} + \sigma_{rr}{}^{(s)} = 0 \tag{A.9}$$

$$\sigma_{r\theta}{}^{(i)} + \sigma_{r\theta}{}^{(s)} = 0 \tag{A.10}$$

A.2 Expression for displacements and stresses

It can be shown that displacements and stresses for all the waves can be expressed also in terms of Ψ and Π and they are

$$\sigma_{rr} = \rho\omega^2[\Psi + \frac{2}{\kappa^2}[\frac{2}{r}\frac{\partial}{\partial r}\Psi + \frac{1}{r^2}\Omega\Psi - \frac{\partial}{\partial r}(\frac{1}{r}\Omega\Pi)]] \tag{A.11}$$

$$\sigma_{r\theta} = \frac{-2\rho\omega^2}{\kappa^2}\frac{d}{d\theta}[\frac{1}{r}\frac{d}{dr}\Psi - \frac{1}{r^2}\Psi + \frac{1}{r}\frac{d}{dr}\Pi + \frac{1}{r^2}(1 + \frac{\kappa^2 r^2}{2})\Pi + \frac{1}{r^2}\Omega\Pi)] \tag{A.12}$$

$$u_r = -\frac{d}{dr}\Psi - \frac{1}{r}\Omega\Pi \tag{A.13}$$

$$u_\theta = -\frac{1}{r}\frac{d}{d\theta}\Psi + \frac{1}{r}\frac{d^2}{d\theta dr}(r\Pi) \tag{A.14}$$

where

$$\Omega = \frac{1}{sin\theta}\frac{d}{d\theta}(sin\theta\frac{d}{d\theta}) \tag{A.15}$$

Start with $\sigma_{rr}{}^{(s)}$,

$$\sigma_{rr}{}^{(s)} = \rho\omega^2[\Psi_s + \frac{2}{\kappa^2}[\frac{2}{r}\frac{\partial}{\partial r}\Psi_s + \frac{1}{r^2}\Omega\Psi_s - \frac{\partial}{\partial r}(\frac{1}{r}\Omega\Pi_s)]] \tag{A.16}$$

$$\rho\omega^2\Psi_s = \rho\omega^2\sum_{m=0}^{\infty} A_m h_m(kr)P_m(\cos\theta) \tag{A.17}$$

$$\frac{2\rho\omega^2}{\kappa^2}\frac{2}{r}\frac{\partial\Psi_s}{\partial r} = \frac{2\rho\omega^2}{\kappa^2}\frac{2}{r}\sum_{m=0}^{\infty} A_m P_m(\cos\theta)\frac{dh_m(kr)}{dr} \tag{A.18}$$

$$\frac{2\rho\omega^2}{\kappa^2}\frac{1}{r^2}\Omega\Psi_s = -\frac{2\rho\omega^2}{\kappa^2}\frac{1}{r^2}\sum_{m=0}^{\infty}(m(m+1))A_m h_m(kr)P_m(\cos\theta) \tag{A.19}$$

$$\frac{-2\rho\omega^2}{\kappa^2}\frac{d}{dr}(\frac{1}{r}\Omega\Pi_s) = -\frac{2\rho\omega^2}{\kappa^2}[\frac{1}{r}\frac{d}{dr}\Omega\Pi_s + \Omega\Pi_s\frac{d}{dr}(r^{-1})] \tag{A.20}$$

It should be noted that the equation (A.19) can be obtained using one of the properties of associated Legendre functions in the book by Arfken and Weber pp. 722 [83]. Now let's simplify these equations. Starting with equation (A.20), it is found that

$$\begin{aligned}\frac{-2\rho\omega^2}{\kappa^2}\frac{d}{dr}(\frac{1}{r}\Omega\Pi_s) &= -\frac{2\rho\omega^2}{\kappa^2}[\frac{1}{r}\frac{d}{dr}\Omega\Pi_s + \Omega\Pi_s(-\frac{1}{r^2})] \\ &= 2\mu[\frac{1}{r}\sum_{m=0}^{\infty}(m(m+1))B_m P_m(\cos\theta)\frac{d}{dr}h_m(\kappa r) \\ &\quad -\frac{1}{r^2}\sum_{m=0}^{\infty}(m(m+1))B_m P_m(\cos\theta)h_m(\kappa r)]\end{aligned} \tag{A.21}$$

Let's try to simplify equation (A.18) and (A.19) in the form

$$2\mu[\sum_{m=0}^{\infty} A_m P_m(\cos\theta)(\frac{2}{r}\frac{d}{dr}h_m(kr) - \frac{(m(m+1))}{r^2}h_m(kr))] \tag{A.22}$$

Using a modified Bessel equation in the book by Arfken and Weber [83] pp. 684,

$$\frac{d^2}{dr^2}R + \frac{2}{r}\frac{d}{dr}R + [k^2 - \frac{m(m+1)}{r^2}]R = 0 \tag{A.23}$$

Let $R = h_m$ and rearrange the equation into the following form

$$\frac{2}{r}\frac{d}{dr}h_m - \frac{m(m+1)}{r^2}h_m = -k^2 h_m - \frac{d^2}{dr^2}h_m \tag{A.24}$$

Substitute back into the earlier equation to get

$$2\mu[\sum_{m=0}^{\infty} A_m P_m(\cos\theta)(-k^2 h_m(kr) - \frac{d^2}{dr^2}h_m(kr))] \tag{A.25}$$

Consider equation A.17, and

$$\rho\omega^2 \sum_{m=0}^{\infty} A_m h_m(kr) P_m(\cos\theta) = k^2(\lambda + 2\mu)\sum_{m=0}^{\infty} A_m h_m(kr) P_m(\cos\theta) \tag{A.26}$$

Notice that the second term presented in this equation can be cancelled with the one shown in Eq. (A.25). Now combine Eqs. (A.21), (A.25), and (A.26) to get to the final expression for ${\sigma_{rr}}^{(s)}$

$$\begin{aligned} {\sigma_{rr}}^{(s)} &= \lambda k^2 \sum_{m=0}^{\infty} A_m h_m(kr) P_m(\cos\theta) \\ &\quad +2\mu \sum_{m=0}^{\infty} [-A_m \frac{d^2}{dr^2}h_m(kr) + B_m(m(m+1))(\frac{1}{r}\frac{d}{dr}h_m(\kappa r) - \frac{h_m(\kappa r)}{r^2})]P_m(\cos\theta) \end{aligned} \tag{A.27}$$

Next, compute the $\sigma_{r\theta}^{(s)}$

$$\sigma_{r\theta}^{(s)} = \frac{-2\rho\omega^2}{\kappa^2}\frac{d}{d\theta}[\frac{1}{r}\frac{d}{dr}\Psi_s - \frac{1}{r^2}\Psi_s + \frac{1}{r}\frac{d}{dr}\Pi_s + \frac{1}{r^2}(1 + \frac{\kappa^2 r^2}{2})\Pi_s + \frac{1}{r^2}\Omega\Pi_s)] \tag{A.28}$$

$$\frac{1}{r}\frac{d}{dr}\Psi_s = \frac{1}{r}\sum_{m=0}^{\infty} A_m P_m(\cos\theta)\frac{d}{dr}h_m(kr) \tag{A.29}$$

$$\frac{1}{r^2}\Psi_s = \frac{1}{r^2}\sum_{m=0}^{\infty} A_m P_m(\cos\theta) h_m(kr) \tag{A.30}$$

$$\frac{1}{r}\frac{d}{dr}\Pi_s = \frac{1}{r}\sum_{m=0}^{\infty} B_m P_m(\cos\theta)\frac{d}{dr}h_m(\kappa r) \tag{A.31}$$

$$\frac{1}{r^2}(1 + \frac{\kappa^2 r^2}{2})\Pi_s = \frac{1}{r^2}(1 + \frac{\kappa^2 r^2}{2})\sum_{m=0}^{\infty} B_m P_m(\cos\theta) h_m(\kappa r) \tag{A.32}$$

$$\frac{1}{r^2}\Omega\Pi_s = \frac{1}{r^2}\sum_{m=0}^{\infty} B_m P_m(\cos\theta)[(-m(m+1))h_m(\kappa r)] \tag{A.33}$$

$$\frac{d}{d\theta}(\frac{1}{r}\frac{d}{dr}\Psi_s) = \frac{1}{r}\sum_{m=0}^{\infty} A_m \frac{d}{dr}h_m(kr)\frac{d}{d\theta}P_m(\cos\theta) \tag{A.34}$$

$$\frac{d}{d\theta}(\frac{1}{r^2}\frac{d}{dr}\Psi_s) = \frac{1}{r^2}\sum_{m=0}^{\infty} A_m \frac{d}{dr}h_m(kr)\frac{d}{d\theta}P_m(\cos\theta) \tag{A.35}$$

$$\frac{d}{d\theta}(\frac{1}{r}\frac{d}{dr}\Pi_s) = \frac{1}{r}\sum_{m=0}^{\infty} B_m \frac{d}{dr}h_m(\kappa r)\frac{d}{d\theta}P_m(\cos\theta) \tag{A.36}$$

$$\begin{aligned}\frac{d}{d\theta}(\frac{1}{r^2}(1+\frac{\kappa^2 r^2}{2})\Pi_s) &= \frac{1}{r^2}\sum_{m=0}^{\infty} B_m \frac{d}{dr}h_m(\kappa r)\frac{d}{d\theta}P_m(\cos\theta) \\ &\quad + \frac{\kappa^2}{2}\sum_{m=0}^{\infty} B_m \frac{d}{dr}h_m(\kappa r)\frac{d}{d\theta}P_m(\cos\theta)\end{aligned} \tag{A.37}$$

$$\frac{d}{d\theta}(\frac{1}{r^2}\Omega\Pi_s) = \frac{1}{r^2}\sum_{m=0}^{\infty} B_m(-m(m+1))h_m(\kappa r)\frac{d}{d\theta}P_m(\cos\theta) \tag{A.38}$$

Rewrite $\sigma_{r\theta}^{(s)}$ in terms of these equations, it follows that

$$\sigma_{r\theta}^{(s)} = -2\mu\sum_{m=0}^{\infty}[(A.34) - (A.35) + (A.36) + (A.37) + (A.38)] \tag{A.39}$$

If a factor of 2 is being multiplied through the expression above, two terms (one appears in Eq. (A.36), the other is the second term appears in Eq. (A.37) can be grouped using the modified Bessel properties in the book by Arfken and Weber pp. 722 [83] pp. 684,

$$\begin{aligned}\frac{d^2}{dr^2}h + \frac{2}{r}\frac{d}{dr}h + [k^2 - \frac{m(m+1)}{r^2}]h = 0 \\ \frac{2}{r}\frac{d}{dr}h + k^2 h = -\frac{d^2}{dr^2}h + \frac{m(m+1)}{r^2}\end{aligned} \tag{A.40}$$

Using Eq. (A.40) to combine Eqs. (A.36),(A.37), and (A.38) together to get

$$\sum_{m=0}^{\infty} B_m[-\frac{d^2}{dr^2}h_m(\kappa r) - (m(m+1)-2)\frac{h_m(\kappa r)}{r^2}]\frac{d}{d\theta}P(\cos\theta) \tag{A.41}$$

Substitute Eqs.(A.34), (A.35) and Eq. (A.41) into Eq. (A.39) to get the $\sigma_{r\theta}^{(s)}$ expression which can be written again as

$$\sigma_{r\theta}^{(s)} = -\mu\sum_{m=0}^{\infty}[2A_m(\frac{1}{r}\frac{d}{dr}h_m(kr) - \frac{h_m(kr)}{r^2}) + B_m(-\frac{d^2}{dr^2}h_m(\kappa r) - (m(m+1)-2)\frac{h_m(\kappa r)}{r^2})]\frac{d}{d\theta}P(\cos\theta) \quad (A.42)$$

Now let us determine the displacement components. Start with ${u_r}^{(s)}$

$${u_r}^{(s)} = -\frac{d}{dr}\Psi_s - \frac{1}{r}\Omega\Pi_s \quad (A.43)$$

$$\frac{d}{dr}\Psi_s = \sum_{m=0}^{\infty}A_m P_m(\cos\theta)\frac{d}{dr}h_m(kr) \quad (A.44)$$

$$\Omega\Pi_s = \sum_{m=0}^{\infty}B_m P_m(\cos\theta)[(-m(m+1))h_m(\kappa r)] \quad (A.45)$$

Therefore the ${u_r}^{(s)}$ can be expressed as

$${u_r}^{(s)} = -\sum_{m=0}^{\infty}A_m P_m(\cos\theta)\frac{d}{dr}h_m(kr) - \frac{1}{r}\sum_{m=0}^{\infty}B_m P_m(\cos\theta)[(-m(m+1))h_m(\kappa r)]$$

$${u_r}^{(s)} = \sum_{m=0}^{\infty}[-A_m\frac{d}{dr}h_m(kr) + \frac{1}{r}B_m(m(m+1))h_m(\kappa r)]P_m(\cos\theta)$$

Next compute ${u_\theta}^{(s)}$

$${u_\theta}^{(s)} = -\frac{1}{r}\frac{d}{d\theta}\Psi_s + \frac{1}{r}\frac{d^2}{d\theta dr}(r\Pi_s) \quad (A.46)$$

$$-\frac{1}{r}\frac{d}{d\theta}\Psi_s = -\frac{1}{r}[\sum_{m=0}^{\infty}A_m h_m(kr)\frac{d}{d\theta}P_m(\cos\theta)] \quad (A.47)$$

$$\frac{1}{r}\frac{d^2}{d\theta dr}(r\Pi_s) = \frac{1}{r}[\frac{d}{d\theta}(r\frac{d}{dr}\Pi_s) + \Pi_s] \quad (A.48)$$

$$r\frac{d\Pi_s}{dr} = r\sum_{m=0}^{\infty}B_m P_m(\cos\theta)\frac{d}{dr}h_m(\kappa r) \quad (A.49)$$

$$\frac{d}{d\theta}(r\frac{d}{dr}\Pi_s) = r\sum_{m=0}^{\infty}B_m\frac{d}{d\theta}P_m(\cos\theta)\frac{d}{dr}h_m(\kappa r) \quad (A.50)$$

$$\frac{d}{d\theta}\Pi_s = \sum_{m=0}^{\infty}B_m h_m(\kappa r)\frac{d}{d\theta}P_m(\cos\theta) \quad (A.51)$$

Therefore ${u_\theta}^{(s)}$ can be rewritten as

$$\begin{aligned} {u_\theta}^{(s)} &= -\frac{1}{r}[\sum_{m=0}^{\infty} A_m h_m(kr)\frac{d}{d\theta}P_m(\cos\theta)] \\ &\quad +\sum_{m=0}^{\infty} B_m \frac{d}{dr}h_m(\kappa r)\frac{d}{d\theta}P_m(\cos\theta) \\ &\quad +\frac{1}{r}\sum_{m=0}^{\infty} B_m \frac{d}{dr}h_m(\kappa r)\frac{d}{d\theta}P_m(\cos\theta) \end{aligned}$$

$$u_\theta{}^{(s)} = \sum_{m=0}^{\infty}[-\frac{h_m(kr)}{r}A_m + (\frac{d}{dr}h_m(\kappa r) + \frac{h_m(\kappa r)}{r})B_m]\frac{d}{d\theta}P_m(\cos\theta) \tag{A.52}$$

For the incident wave, stresses and displacements are computed in the same manner except Π_i is taken to be zero. Given

$$\Psi_{(i)} = \frac{1}{k}\sum_{m=0}^{\infty}(-i)^{m+1}(2m+1)P_m(\cos\theta)j_m(kr) \tag{A.53}$$

$$u_r{}^{(i)} = \frac{-1}{k}\sum_{m=0}^{\infty}(-i)^{m+1}(2m+1)P_m(\cos\theta)\frac{dj_m(kr)}{dr} \tag{A.54}$$

$$u_\theta{}^{(i)} = \frac{-1}{k}\sum_{m=0}^{\infty}(-i)^{m+1}(2m+1)P_m(\cos\theta)\frac{j_m(kr)}{r} \tag{A.55}$$

$$\begin{aligned} {\sigma_{rr}}^{(i)} &= \frac{(\lambda+2\mu)k^2}{k}\sum_{m=0}^{\infty}(-i)^{m+1}(2m+1)j_m(kr)P_m(\cos\theta) \\ &\quad +\frac{2\mu}{k}\sum_{m=0}^{\infty}(-i)^{m+1}(2m+1)\frac{2}{r}\frac{d}{dr}j_m(kr)P_m(\cos\theta) \\ &\quad +\frac{2\mu}{k}\sum_{m=0}^{\infty}(-i)^{m+1}(2m+1)\frac{1}{r^2}j_m(kr)(-m(m+1))P_m(\cos\theta) \end{aligned} \tag{A.56}$$

$${\sigma_{r\theta}}^{(i)} = \frac{-2\mu}{k}\sum_{m=0}^{\infty}(-i)^{m+1}(2m+1)[\frac{1}{r}\frac{d}{dr}j_m(kr) - \frac{1}{r^2}j_m(kr)]\frac{dP_m(cos\theta)}{d\theta} \tag{A.57}$$

A.3 Scattering cross section expression

From the displacement and the stress of the scattered wave, the scattering cross section can be computed. The scattering cross section is defined as the area, which if placed into the incident field normal to the direction of propagation, would intercept an energy flux equal to that of the total scattered wave field through a closed surface which contains the scatterer.

Followed Ying and Truell [57], the energy flux $F^{(s)}$ of scattered waves through a spherical surface having a radius b that completely surrounds the spherical void object of radius a. On writing in the spherical components,

$$F^{(s)} = -\int\int(\Sigma \cdot \frac{\partial \mathbf{u}}{\partial t}) \cdot n dA, \tag{A.58}$$

where Σ, and $\mathbf{u}$ are the complex stress and displacement tensors and n is the outward unit normal to the surface of integration which bounds the volume under the consideration. Since only the real or the imaginary parts of the complex stress and displacement tensors shall be used for the computation of the energy, one uses $\Sigma = \frac{1}{2}(\Sigma + \Sigma^*)$ and $\mathbf{u} = \frac{1}{2}(\mathbf{u} + \mathbf{u}^*)$ where "$*$" denotes a complex conjugate. In spherical components one can write,

$$\begin{aligned} F^{(s)} &= \frac{1}{2}\,\omega \int\int(\sigma_{rr}u_r^* + \sigma_{r\theta}u_\theta^* + \sigma_{\phi r}u_\phi^* - \sigma_{rr}^* u_r - \sigma_{r\theta}^* u_\theta - \sigma_{\phi r}^* u_\phi)^{(s)} dA \\ &= \frac{1}{2}\,\omega \int_{\theta=0}^{\pi}\int_{\phi=0}^{2\pi}(\sigma_{rr}u_r^* + \sigma_{r\theta}u_\theta^* - \sigma_{rr}^* u_r - \sigma_{r\theta}^* u_\theta)^{(s)} b^2 sin\theta d\theta d\phi \\ &= \frac{1}{2}\,\omega \int_{\theta=0}^{\pi}(\sigma_{rr}u_r^* + \sigma_{r\theta}u_\theta^* - \sigma_{rr}^* u_r - \sigma_{r\theta}^* u_\theta)^{(s)} 2\pi b^2 sin\theta d\theta \end{aligned} \tag{A.59}$$

Notice that

$$\begin{aligned} \sigma_{rr}u_r^* - \sigma_{rr}^* u_r &= \sigma_{rr}u_r^* - (\sigma_{rr}u_r^*)^* \\ A - A^* &= 2\mathrm{Im}[A] \end{aligned}$$

So one need to calculate just $\mathrm{Im}[\sigma_{rr}u_r^*]$ and $\mathrm{Im}[\sigma_{r\theta}u_\theta^*]$. Also, if one assume that b is so large $b \to \infty$, the values of ${\sigma_{rr}}^{(s)}, {\sigma_{\theta\ r}}^{(s)}, {u_r}^{(s)}, {u_\theta}^{(s)}$ can be written as

$$\begin{aligned}
{\sigma_{rr}}^{(s)} &= \lambda k^2 \sum_{m=0}^{\infty} A_m h_m P_m(cos\theta) + 2\mu \sum_{m=0}^{\infty} -A_m \frac{d^2}{dr^2} h_m(kr) P_m(cos\theta) \\
{\sigma_{r\theta}}^{(s)} &= -\mu \sum_{m=0}^{\infty} B_m - \frac{d^2}{dr^2} h_m(\kappa r) d\theta P_m(cos\theta) \\
{u_r}^{(s)} &= \sum_{m=0}^{\infty} -A_m \frac{d}{dr} h_m(kr) P_m(cos\theta) \\
{u_\theta}^{(s)} &= \sum_{m=0}^{\infty} B_m \frac{d}{dr} h_m(\kappa r) \frac{d}{d\theta} P_m(cos\theta)
\end{aligned} \tag{A.60}$$

For mathematical simplicity, one shall use important relations for spherical bessel functions of the third kind [84]:

$$\begin{aligned}
h_n(z) &= \frac{i^{n+1}}{z} e^{-iz} \\
h_n^*(z) &= \frac{(-i)^{n+1}}{z} e^{iz} \\
\frac{dh_n(z)}{dz} &= \frac{i^n}{z} e^{-iz} = -ih_n \\
\frac{dh_n^*(z)}{dz} &= \frac{(-i)^n}{z} e^{iz} = -ih_n^* \\
\frac{d^2h_n(z)}{dz^2} &= \frac{i^{n-1}}{z} e^{-iz} = -h_n \\
\frac{d^2h_n^*(z)}{dz^2} &= \frac{(-i)^{n-1}}{z} e^{iz}
\end{aligned} \tag{A.61}$$

Rewrite ${\sigma_{rr}}^{(s)}, {\sigma_{r\theta}}^{(s)}, {u_r}^{(s)}, {u_\theta}^{(s)}$ in terms of h_m terms and one has

$$
\begin{aligned}
{\sigma_{rr}}^{(s)} &= (\lambda+2\mu)k^2\sum_{m=0}^{\infty}A_m h_m P_m cos\theta \\
{\sigma_{r\theta}}^{(s)} &= -\mu\sum_{m=0}^{\infty}B_m\kappa^2 h_m\frac{dP(cos\theta)}{d\theta} \\
u_r^{*(s)} &= \sum_{m=0}^{\infty}ik^*A_m^*h_m^*P_m(cos\theta) \\
u_\theta^{*(s)} &= \sum_{m=0}^{\infty}-i\kappa^*B_m^*h_m^*\frac{dP_m(cos\theta)}{d\theta}
\end{aligned}
\tag{A.62}
$$

Substitute these into Eq.(A.59) to get

$$
\frac{1}{2}(\omega\int_{\theta=0}^{\pi}2\mathrm{Im}(\sigma_{rr}u_r^*)+2\mathrm{Im}(\sigma_{r\theta}u_\theta^*)\,2\pi R^2 sin\theta d\theta)
$$

Apply orthogonality relations [84]:

$$
\begin{aligned}
\int_{\theta=0}^{\pi}P_m(cos\theta)P_n(cos\theta)sin\theta d\theta &= \frac{2}{2n+1}\delta_{pq} \\
\int_{\theta=0}^{\pi}\frac{dP_m(cos\theta)}{d\theta}\frac{dP_{n-m}(cos\theta)}{d\theta}sin\theta d\theta &= \frac{2m(m+1)}{2m+1}\delta_{m(n-m)},
\end{aligned}
\tag{A.63}
$$

The first integral on the left hand side of Eq.(A.63) can be reduced to:

$$
\begin{aligned}
&\frac{1}{2}(2\omega\int_{\theta=0}^{\pi}\mathrm{Im}(\sigma_{rr}u_r^*)\,2\pi R^2 sin\theta d\theta) = \\
&\frac{1}{2}(2\omega\int_{\theta=0}^{\pi}\mathrm{Im}[(\lambda+2\mu)k^2\sum_{m=0}^{\infty}A_m h_m P_m\sum_{m=0}^{\infty}iA_m^*k^*h_m^*P_m\,2\pi R^2 sin\theta d\theta]) \\
&\frac{1}{2}(2\omega\,\mathrm{Im}[(\lambda+2\mu)k^2\sum_{m=0}^{\infty}i|A_m|^2k^*\frac{1}{|k|^2R^2}\frac{2(2\pi)}{2m+1}R^2]) \\
&\frac{1}{2}(2\omega\,\mathrm{Im}[\omega^2\rho\sum_{m=0}^{\infty}i|A_m|^2\frac{1}{k}\frac{4\pi}{2m+1}]) \\
&\frac{1}{2}(2\omega\,[4\pi\rho\omega^2\sum_{m=0}^{\infty}|A_m|^2\frac{1}{k}\frac{1}{2m+1}]) \\
&4\pi\rho\omega^3\sum_{m=0}^{\infty}|A_m|^2\frac{1}{k}\frac{1}{2m+1}
\end{aligned}
\tag{A.64}
$$

The second integral of Eq.(A.63) can be reduced to:

$$\frac{1}{2}(2\omega \int_{\theta=0}^{\pi} \mathrm{Im}(\sigma_{r\theta} u_\theta^*)\, 2\pi R^2 sin\theta d\theta) =$$
$$\frac{1}{2}(2\omega \int_{\theta=0}^{\pi} \mathrm{Im}[\kappa^2 \mu \sum_{m=0}^{\infty} B_m h_m \frac{dP_m}{d\theta} \sum_{m=0}^{\infty} iB_m^* \kappa^* h_m^* \frac{dP_m}{d\theta}\, 2\pi R^2 sin\theta d\theta])$$
$$\frac{1}{2}(2\omega \int_{\theta=0}^{\pi} \mathrm{Im}[\kappa^2 \mu \sum_{m=0}^{\infty} |B_m|^2 (i) \frac{\kappa^*}{|\kappa|^2 R^2} \frac{2m(m+1)}{2m+1} 2\pi R^2])$$
$$\frac{1}{2}(2\omega \int_{\theta=0}^{\pi} \mathrm{Im}[\omega^2 \rho \sum_{m=0}^{\infty} |B_m|^2 (i) \frac{\kappa^*}{|\kappa|^2 R^2} \frac{2m(m+1)}{2m+1} 2\pi R^2])$$
$$\frac{1}{2}(2\omega \int_{\theta=0}^{\pi} \mathrm{Im}[4\pi\rho\omega^2 \sum_{m=0}^{\infty} |B_m|^2 (i) \frac{1}{|\kappa|} \frac{m(m+1)}{2m+1}])$$
$$4\pi\rho\omega^3 \sum_{m=0}^{\infty} |B_m|^2 \frac{1}{\kappa} \frac{m(m+1)}{2m+1} \tag{A.65}$$

At the end we get the rate $F^{(s)}$

$$F^{(s)} = 4\pi\rho\omega^3 \sum_{m=0}^{\infty} \frac{1}{2m+1} [\frac{1}{k} |A_m|^2 + \frac{m(m+1)}{\kappa} |B_m|^2] \tag{A.66}$$

The scattering cross section is usually defined as the ratio of the total energy scattered per unit time to the energy per unit area carried per unit time by the incident wave, the unit area being normal to the propagation direction of the plane incident wave. The rate of energy transport per unit area for the incident wave is found to be $F^{(i)} = \frac{\rho\omega^3}{k}$. It follows that the scattering cross section of a spherical obstacle is

$$\gamma^{sca} = 4\pi \sum_{m=0}^{\infty} \frac{1}{2m+1} [|A_m|^2 + m(m+1) \frac{k}{\kappa} |B_m|^2] \tag{A.67}$$

Although it is not obvious, γ^{sca} has the dimensions of area. Such coefficient is very useful in experimental detection of voids.

It is also interesting to see that the function γ^{sca} from A.67 is closely connected with the value of the field $u(r, \theta = 0)^{(s)}$ of scattered waves that is observed along the

positive forward propagation direction in the far-filed. At large distance from the scatterer, the radial displacement component is approximated by ${u_r}^{(s)} \cong f(\theta)e^{(-ikr)}/r$. The term $f(\theta)$ is denoted as the far-field scattering amplitude of the longitudinal wave. In the far-field, spherical Hankel functions can be approximated as Eq. (A.61). Using these relations, the far field scattering is then determined as

$$f(\theta) = \sum_{n=0}^{\infty} - A_m(i^m)P_m(cos\theta) \tag{A.68}$$

For the special case of the forward propagation direction, one obtain

$$f(\theta = 0) = \sum_{n=0}^{\infty} - A_m(i^m) \tag{A.69}$$

by using $P_m(1) = 1$.

Through the optical theorem [49], a different expression for scattering cross-section can also be obtained

$$\gamma^{sca} = -\frac{4\pi}{k}\mathrm{Im}f(0) \tag{A.70}$$

The expression in Eq.(A.70) is a useful relationship between the amplitude of the forward scattered field and the total energy scattered in all directions by the inclusion.

A.4 Determination of the series coefficients from the boundary conditions

Having found expressions for the stresses and displacements, one make use of the boundary condition at $r = a$. In matrix form, the two equations can be written as

$$\begin{pmatrix} H_{11} & H_{12} \\ H_{21} & H_{22} \end{pmatrix} \begin{pmatrix} A \\ B \end{pmatrix} = \frac{-1}{k}(-i)^{m+1}(2m+1) \begin{pmatrix} J_{11} \\ J_{21} \end{pmatrix} \tag{A.71}$$

where

$$H_{11} = \frac{\lambda}{2\mu}(kr)^2 h_m(kr) - r^2\frac{d^2h_m(kr)}{dr^2} \quad (A.72)$$

$$H_{12} = m(m+1)(r\frac{dh_m(\kappa r)}{dr} - h_m(\kappa r))$$

$$H_{21} = (r\frac{dh_m(kr)}{dr} - h_m(kr)) \quad (A.73)$$

$$H_{22} = \frac{-1}{2}(r^2\frac{d^2h_m(\kappa r)}{dr^2} + (m^2+m-2)h_m(\kappa r) \quad (A.74)$$

$$J_{11} = \frac{\lambda}{2\mu}(kr)^2 j_m(kr) - r^2\frac{d^2j_m(kr)}{dr^2} \quad (A.75)$$

$$J_{21} = r\frac{dj_m}{dr}(kr) - j_m(kr) \quad (A.76)$$

Notice that one can also simplify and write H and J in terms of h_m and h_{m+1} using the following relations:

$$\begin{aligned}
r\frac{dh_n(kr)}{dr} &= kr\frac{dh_n(kr)}{dkr} = kr(\frac{n}{kr}h_n(kr) - h_{n+1}(kr)) \\
r\frac{dh_n(kr)}{dr} &= kr\frac{dh_n(kr)}{dkr} = nh_n(kr) - (kr)h_{n+1}(kr) \\
r\frac{dh_n(kr)}{dr} + h_n(kr) &= (n+1)h_n(kr) - (kr)h_{n+1}(kr) \\
r\frac{dh_n(kr)}{dr} - h_n(kr) &= (n-1)h_n(kr) - (kr)h_{n+1}(kr)
\end{aligned}$$

Using these relations together with the modified bessel equation, the H and J components can be related to

$$\begin{aligned}
r\frac{dh_m(kr)}{dr} - h_m(kr) &= (m-1)h_m(kr) - (kr)h_{m+1}(kr) \\
\frac{\lambda}{2\mu}(kr)^2 h_m(kr) - r^2\frac{d^2h_m(kr)}{dr^2} &= -(m^2 - m - \frac{(\kappa r)^2}{2})h_m(kr) - 2(kr)h_{m+1}(kr) \\
\frac{-1}{2}(r^2\frac{d^2h_m(\kappa r)}{dr^2} + (m^2+m-2)h_m(\kappa r)) &= -(m^2 - 1 - \frac{(\kappa r)^2}{2})h_m(\kappa r) - (\kappa r)h_{m+1}(\kappa r)
\end{aligned}$$

Numerical calculations can be performed different kr for the longitudinal wave scattering by a spherical cavity in a solid matrix. The matlab program can be used. The

basic factors involved in the calculations are as follows:

(1) Parameters-the input parameters, which characterize a given computation, are ρ, c_l, c_s, which signify, respectively, the density, the longitudinal and transverse velocities in the matrix medium and cavity. The other quantities relevant to the computation such as normalized wave numbers ka, κa are also computed.

(2) Bessel and Neumann functions - the coefficients A_m and B_m which appear earlier in the previous section involve spherical Bessel and Neumann functions of the normalized wave number ka. In performing these calculations, the functions are computed by means of a computer subroutine.

(3) Linear equations - the computation necessitates numerically solving for A_m and B_m coefficients. The method which is used is usually one of matrix inversion, where the solution matrix can be found by multiplying the inverse of the matrix.

(4) Series Summation - It has been reported elsewhere that typical calculation requires the summation should be carried out until the ratio of the current term to the current partial sum is less than 0.00001. A general rule of thumb is to use a number of m approximately equal to $ka + 6$. This is generally true for most materials.

Appendix B

Ultrasonic hysteresis absorption of Lucite

Lucite methyl methacrylate polymer was among the first plastics derived from petrochemical. It is sold by the short tradenames Plexiglas, Acrylite, Perspex and is commonly called acrylic. The material is often used as an alternative to glass because it is lighter. Its density is about 1190 kg/m^3 which is half of that of glass. It is not shatter, softer and can be easily formed by heat. It also transmits more light (92% of visible light than glass). Unlike glass, PMMA does not filter ultraviolet light. Some manufacturers coat their PMMA with UV films to add this property. Other uses include laser discs, rear light of cars, windows, and dental implants.

Reliable absorption attenuation measurements were made on PMMA by Hartmann and Jarzynski [46] and reported in a recent book by Cheeke [60] over a wide ultrasonic frequency range. In this study, measurements of longitudinal wave phase velocity and absorption attenuation with a PMMA specimen serves as a testing ground for a measurement accuracy of absorption attenuation measurement in hardened cement paste. The PMMA used here was provided by GE polymerland, an authorized distributor of Altuglas and was received in the form of a cast thick plate. The specimen is 5" x 5" x 1" (12.7 cm x 12.7 cm x 2.54 cm). The same experimental setup as is sketched in Fig. 5.6 is used. Ultrasonic pulses are sent from one transducer to the other with the specimen in the path of the ultrasound beam.

Followed the methodology presented in Chapter 5, longitudinal absorption and phase velocity at room temperature of the PMMA specimen are measured for a frequency range of 0.5 - 5 MHz. The results are plotted and shown in Fig. B.1 and Fig B.2. As can be seen from Fig. B.1, the major component of the room-temperature longitudinal absorption attenuation in PMMA has a linear dependency of frequency. This type of the absorption is referred to as a hysteresis absorption [47]. A hysteresis absorption is one for which the absorption α_a per wavelength is constant. That is $\alpha_a\lambda$ = constant. As with PMMA, the data shown in Fig B.1 follow a straight line and the $\alpha\lambda$ (longitudinal) is estimated to be equal to 0.045 Np at room temperature. The longitudinal phase velocity is found to be 2787 m/s. For PMMA, Hartman and Jarzynski [46] finds $\alpha_a\lambda = 0.022$ Np and $c_L = 2787$ m/s for Lucite (optical grade) and Cheeke [60] finds $\alpha_a\lambda = 0.045$ Np and $c_L = 2750$ m/s for clear Plexiglass G (lower density as compared to the optical grade one). Guided by the above values, it can be seen that there is some variability in published values, particularly for absorption attenuation. Within experimental accuracy, the given measurement values are within the range of published values.

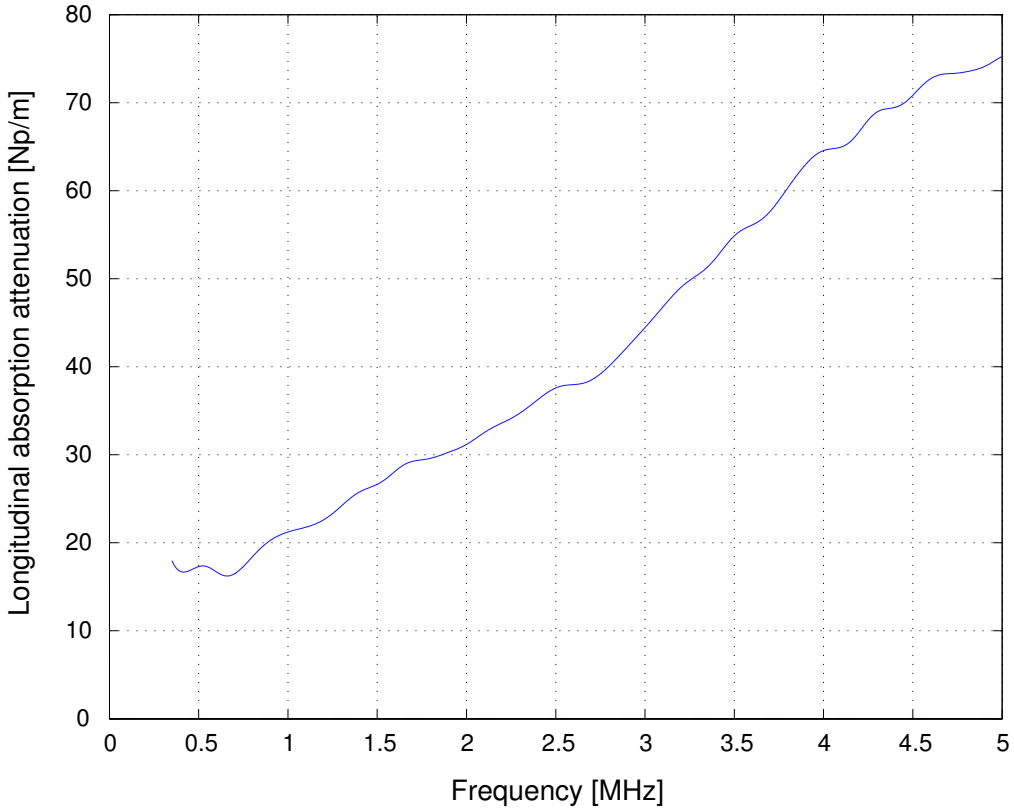

Figure B.1: Longitudinal absorption vs frequency at room temperature for Lucite

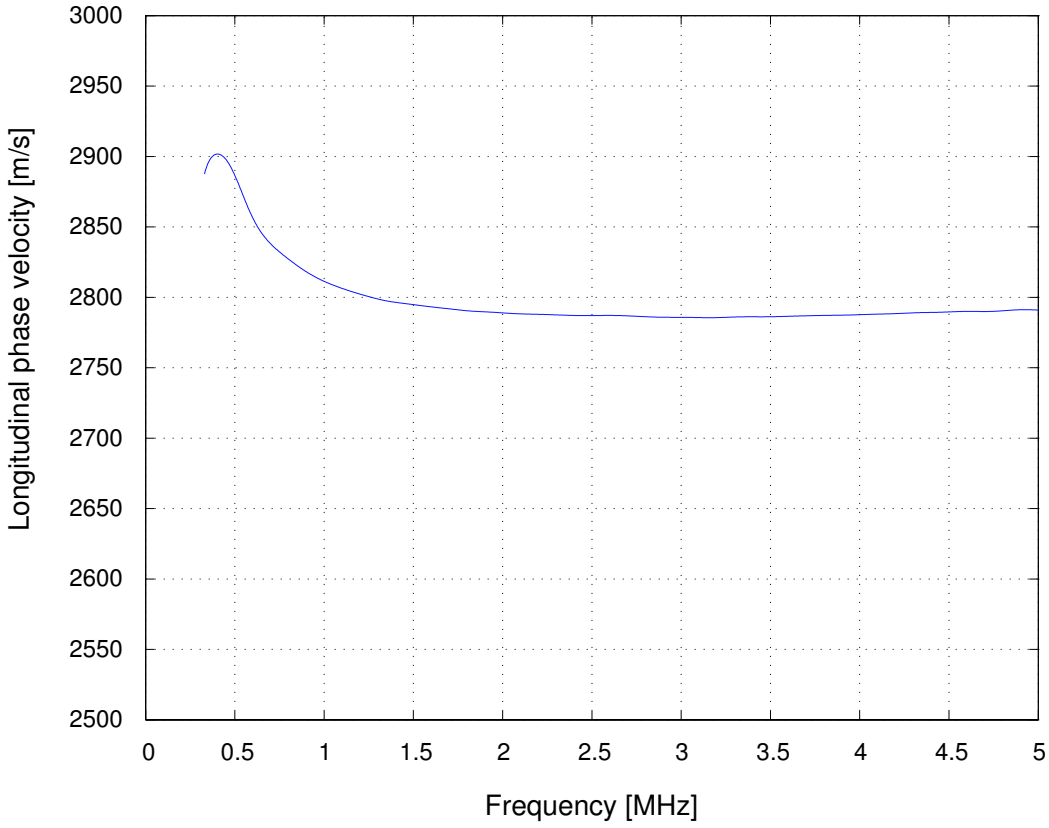

Figure B.2: Longitudinal phase velocity vs frequency at room temperature

Appendix C

Void sizing using Image-Pro Plus

This appendix describes the void size measurement technique using a commercial image processing and analysis software, Image-Pro Plus. Noting that the software runs on Window 98 Pro platform and the following steps summarize the procedure.

1. Preparing the specimen for testing

When analyzing air void size of hardened cement paste samples, the image can be analyzed best if the test specimens are polished to provide a smooth surface for microscopic examinations. The preparation includes grinding and polishing, which are accomplished by hand on a general purpose variable speed grinder/polisher ECOMET 4. Polishing is done by using silicon carbide grit no. 240, 320 and 600 as abrasive. The purpose of polishing the surface is to remove any deformations as well as scratches induced during the saw-cutting process. At the end of preparation stage, the specimen is cleaned thoroughly to remove any polishing deposits. No materials were used to enhance contrast between the air voids and the cement paste matrix.

2. Image acquisition

Images of hardened cement paste specimens are captured using the image analysis system. The system consists of a Leica SZX2 stereomicroscope, a video camera, and a computer with Image-Pro Plus image analysis software. The microscope has a zoom

objective lenses with stop setting of 0.63X magnification. To begin with the acquisition, one must do the following:

a) Setting up the microscope: Turn on the light source of the microscope and adjust light intensity to an appropriate level using the knob at the right and rear of the microscope base. The illumination bench has Bright Field (BF) and Dark Field (DF) capabilities, and either mode shall be selected from the detector switch located at the front of the microscope base to make the edge of the void more visible. Alternatively, two spotlight microscope lamps can also be used to provide illumination at a low and variable incident angle to the surface, so that the air voids are demarked by a shadow. Next, select the zoom position to the lowest magnification, and then place specimen on the specimen holder. If the voids are very small, other magnifications may be selected. In general, it is beneficial to have a focus clear, large number of voids in the field of two-dimensional planar view.

b) Acquiring and saving the image: Open the Image-Pro Plus software (double-click on the IMAGE ANALYSIS icon on the desktop) if it's not open already. Figure C.1 shows the first screen that opens up when the program starts, and points to a few of the icons and menus mentioned below. From the "Acquire" menu select "Scan", when the picture appears on the screen, fine-tune the focus if necessary and click "Capture" button in the image dialog box. To save the image, click on "File" menu, select "Save as..." and type a name that identifies the picture and select the folder with appropriate name and file type for later use.

3. Performing size analysis

Once the desired image has been saved to the disk, a void size analysis can be done using the software. The following list of steps is provided only as guide. More detailed

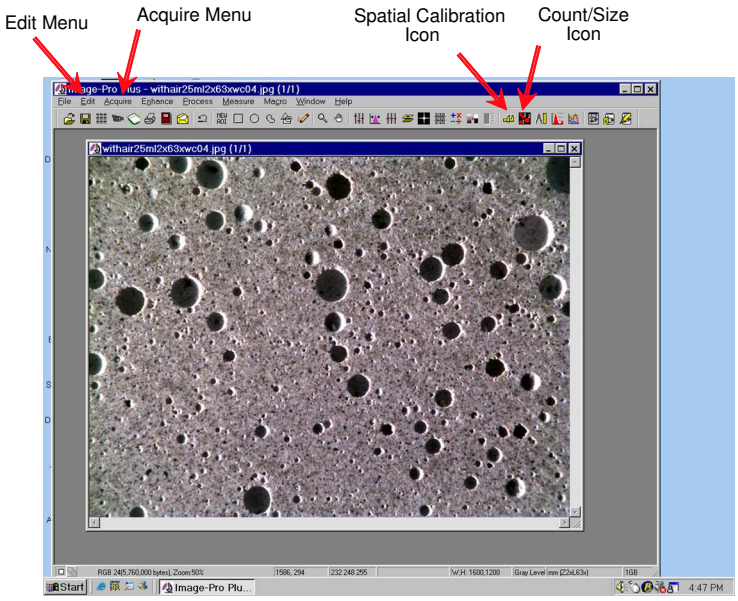

Figure C.1: First screen of the image analysis program showing a typical image

explanation should refer to the software manual.

a) Select image scale: The program relies on a series of reference images of known size to determine the actual size of the items on a picture (e.g. a ruler). These calibrations are necessary and for this study they have been made (in millimeter units). To do this select the "Spatial Calibration" icon (see Fig.C.1) and from the list select the appropriate zoom position used (for example if the 0.63X zoom position is used with the microscopic objective, select "SZX2-63" from the list)

b) Select measures to report size: There is a large amount of measures that can be reported. To get a report on void size, click on the "Count/Size icon" (see Fig C.2) and when the "Count/Size" window appears, select the "Measure" menu then the "Select Measurement..." option. This will open up the "Select Measurements" window. Choose a measure of circularity index (or radius). This will highlight all the

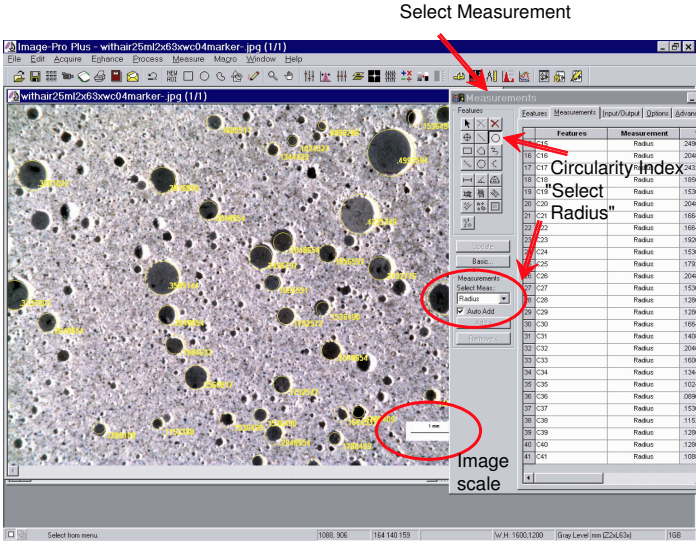

Figure C.2: Segmentation window showing the measurement example

voids counted, with yellow circle and a number assigned to each void. Figure C.2 shows this window and its regions. Sometimes, if air voids are not well demarked or separated very well by shadows, two or more voids will be measured as one. To correct this, a variety of ways can be selected from the program to try to separate the image of these voids either automatically or manually. For example, "Watershed Split" can be selected from the "Edit" menu in the "Count/Size" window. Each time a split option is used the program will select a proper threshold value (to differentiate the background from the image objects of interest), recount and remeasure the size of voids.

c) Viewing measurement values: Once the voids have been sized and counted, the results can be viewed by clicking on the "View" menu of the "Count/Size" window. The "Measurement Data" option will produce a summary of void radius data. Data file, "Measurement Data", can be directly exported to Excel files using the "DDE to Excel" option in the "File" menu in each of the data windows.

Bibliography

[1] Meyer, C. Concrete materials and sustainable development in the USA. *Structural Engineering International*, 2004.

[2] Truell, R., and Hikata, A. Fatigue in 2s aluminum as observed by ultrasonic attenuation methods. *Special Technical Publication*, No. 213, 1957.

[3] Bratina, W.J., and Mills, D. Study of fatigue in metals using ultrasonic technique. *Canadian Metallurgical Quarterly*, 1:83–97, 1962.

[4] Joshi, N.R., and Green, R.E. . Ultrasonic detection of fatigue damage. *Journal of Engineering Fracture Mechanics*, 4:527–538, 1972.

[5] Papadakis, E.P. Ultrasound attenuation caused by scattering in polycrystalline metals. *Journal of the Acoustical Society of America*, 37:711–717, 1965.

[6] Roney, R.K. *The influence of metal grain size on the attenuation of an ultrasonic wave.* Ph.D. Thesis, California Institute of Technology.

[7] Gubernatis, J.E., and Domany, E. Effects of microstructure on the speed and attenuation of elastic waves in porous materials. *Wave Motion*, 6:579–589, 1984.

[8] Sayers, C.M., and Smith, R.L. The propagation of ultrasound in porous media. *Ultrasonics*, 20:201–205, 1982.

[9] Adler, L., Rose, J.H., and Mobley, C. Ultrasonic method to determine gas porosity in aluminum alloy casting theory and experiment. *Journal of Applied Physics*, 59:336–347, 1986.

[10] Nair, S.M., Hsu, D.K., and Rose, J.H. Porosity estimation using the frequency dependence of the ultrasonic attenuation. *Journal of Nondestructive Evaluation*, 8:13–26, 1989.

[11] Kumar, A., Jayakumar, T., Palanichamy, P., and Raj, B. . Influence of grain size on ultrasonic spectral parameters in aisi type 316 stainless steel. *Scripta Materialia*, 40:333–340, 1999.

[12] Smith, R.L. The effect of grain size distribution on the frequency dependence of the ultrasoinc attenuation in polycrystalline materials. *Ultrasonics*, 20:211–214, 1982.

[13] Mal, A.K., Bar-Cohen, Y., and Lih, S.S. . Wave attenuation in fiber-reinforced composites. *ASTM Special Technical Publication*, 1169:245–261, 1992.

[14] Yang, R.B., and Mal, A.K. Multiple scattering of elastic waves in a fiber reinforced composites. *Journal of mechanical physics and solids*, 42:1945–1968, 1994.

[15] Kozlov, V.N., Shevaldykin, V.G., and Yakovlev, N.N. Experimental determination of an ultrasonic wave in concrete. *Scientific Research Institute for NDT, Moscow,*, 2:67–75, 1988.

[16] Jacobs, L.J., and Owino, J. Effect of aggregate size on attenuation of Rayleigh surface waves in cement-based materials. *Journal of Engineering Mechanics*, 126:1124–1130, 2000.

[17] Landis, E.N., and Shah, S.P. Frequency-dependent stress wave attenuation in cement-based materials. *Journal of Engineering Mechanics*, 121:737–743, 1995.

[18] Schickert, M. Ultrasonics NDE of concrete. *2002 IEEE Ultrasonics Symposium. Proceedings (Cat. No.02CH37388)*, 1:739–748, 2002.

[19] Anugonda, P., Wiehn, J.S., and Turner, J.A. Diffusion of ultrasound in concrete. *Ultrasonics*, 39:429–435, 2001.

[20] Popovics, S., Bilgutay, N., Karaoguz, M., and Akgul, T. High frequency ultrasound technique for testing concrete. *ACI Material Journal*, 97:58–65, 2000.

[21] Mehta, P.K., and Monteiro, P.J.M. *Concrete: microstructure, properties, and materials*. Prentice-Hall, Inc. Eaglewood Cliffs, New Jersey, 1993.

[22] Suaris, W., and Fernando, V. Ultrasonic pulse attenuation as a measure of damage growth during cyclic loading of concrete. *ACI Materials Journal*, 84:185–193, 1987.

[23] Selleck, S.F., Landis, E.N., Peterson, M. L., Shah, S.P., and Achenbach, J.D. Ultrasonic investigation of concrete with distributed damage. *ACI Materials Journal*, 95:27–36, 1998.

[24] Gaydecki, P.A., Burdenki, F.M., John, D.G., and Payne, P.A. The propagation and attenuation of medium frequency ultrasonic waves in concrete: a signal analytical approach. *Measurement and Science Technology*, 3:126–134, 1992.

[25] Li, D. Frequency spectrum analysis of ultrasonic testing signal in concrete. *Nondestructive Testing of Concrete Elements and Structures*, pages 104–114, 1992.

[26] Berthelot, J.-M., Souda, M.B., and Robert, J.L. Study of wave attenuation in concrete. *Journal of Material Research*, 8:2344–2353, 1993.

[27] Daponte, P., Maceri, F., and Ollivito, R. Ultrasonic signal processing techniques for the measurement of damage growth in structural materials. *IEEE Transactions on Instrumentation and Measurement*, 44:1003–1008, 1995.

[28] Becker, J., Jacobs, L.J., and Qu, J. Characterization of cement-based materials using diffuse ultrasound. *Journal of Engineering Mechanics*, 39:1478–1484, 2003.

[29] Biwa, S. Independent scattering and wave attenuation in viscoelastic composites. *Mechanics of Materials*, 33:635–647, 2001.

[30] Powers, T.C. *Properties of fresh concrete*. John Wiley and Sons Inc., New York, 1968.

[31] Rose, J.L. *Ultrasonic waves in solid media*. Cambridge University Press, 1999.

[32] Stark, D. *Characteristics and utilization of coarse aggregate associated with D-cracking*, volume Bulletin RD047.01p.

[33] Powers, T.C. *Freezing effects in concrete*. Durability of Concrete. SP.-47, American Concrete Institute, Detroit, MI, 1975.

[34] Du, L., and Folliard, K. J. Mechanisms of air entrainment in concrete. *Cement and Concrete Research*, 35:1463–1471, 2005.

[35] ACI Committee 201 - Guide for making a condition survey of concrete in service (ACI 201.R-92). *American Concrete Institute*. Farmington Hills, Mich., 1992.

[36] Lawrence, C.D. *An examination of possible errors in the determination of nitrogen isotherms on hydrated cements*. Cement and Concrete Association, UK (technical report no. 42.520).

[37] ASTM C173 - air content of freshly mixed concrete by the volumetric method. *American Society of Testing and Materials*. Philadelphi, PA, 1994.

[38] ASTM C231 - standard test method for air Content of freshly mixed concrete by the pressure method. *American Society of Testing and Materials*. Philadelphi, PA, 1991.

[39] ASTM C457 - microscopical determination of parameters of the air-void system in the hardened concrete. *American Society of Testing and Materials*. West Conshohocken, PA, 2000.

[40] Achenbach, J.D. *Wave propagation in elastic solids*. North-Holland, 1975.

[41] Graff, K.F. *Wave motion in elastic solids*. Dover publications, 1975.

[42] Ishimaru, A. *Wave propagation and scattering in random media*. Academic Press, New York, 1978.

[43] Hutchins, D.A., and Hayward, G. *The radiated field of ultrasonic transducers*. Physical Acoustics, Vol. XIX, Academic Press, New York, Thurston, R.N., and Pierce, A.D., eds., 1990.

[44] Rogers, P.H., and Van Buren, A.L. An exact expression for the Lommel diffraction correction integral. *Journal of the Acoustical Society of America*, 55:724–728, 1974.

[45] Mason, W.P. *Physical acoustics and the properties of solids*. Van Nostrand, Princeton, NJ, 1958.

[46] Hartmann, B., and Jarzynski, J. Ultrasonic hysteresis absorption in polymers. *Journal of Applied Physics*, 43:4304–4312, 1972.

[47] Fung, Y.C. *A first course in continuum mechanics*. Springer-Verlag, New York, 1980.

[48] Foldy, L.L. The multiple scattering of waves. i. general theory of isotropic scattering by randomly distributed scatterers. *Physical Review*, 67:107–119, 1945.

[49] Waterman, P.C., and Truell, R. Multiple scattering of waves. *Journal of Mathematical Physics*, 2:512–537, 1961.

[50] Dainty, A.M., and Toksoz, M.N. Elastic eave propagation in a highly scattering medium-a diffusion approach. *Journal of Geophysics*, 43:375–388, 1977.

[51] Mason, W.P. *Piezoelectric crystals and their application to ultrasonics.* Van Nostrand, New York, 1950.

[52] Middleton, R.G. *Handbook of oscilloscope waveform analysis and applications.* Reston Publishing Co., VA, 1977.

[53] Oppenheim, A.V. and Schafer, R.W. *Discrete-time signal processing, second edition.* Prentice-Hall, Inc.: Upper Saddle River, NJ, 1999.

[54] Santamarina, J.C. and Fratta, D. *Introduction to discrete signals and inverse problems in civil engineering.* ASCE Press, Reston, VA, 1998.

[55] Beltzer,A.I., and Brauner, N. Wave propagatin in random pariculate composites: a modification of the foldy-lax theory. *Acustica*, 65:156–162, 1988.

[56] Brauner, N., and Beltzer,A.I. Wave-obstacle interaction in a lossy medium: energy perturbations and negative extinction. *Ultrasonics*, 26:328–334, 1988.

[57] Ying, C.F., and R. Truell. Scattering of a plane longitudinal wave by a spherical obstacle in an isotropically elastic solid. *Journal of Applied Physics*, 27:1086–1097, 1956.

[58] Kinra, V.K., Petraitis, M.S., and Datta, S.K. Ultrasonic wave propagation in a random particulate composite. *International Journal of Solids and Structures*, 16:301–312, 1980.

[59] Sears, F.M., and Bonner, B.P. Ultrasonic attenuation by spectral ratios utilizing signal processing techniques. *IEEE Transactions on Geoscience and Remote Sensing*, 2:95–99, 1981.

[60] Cheeke, J.D.N. *Fundamentals and applications of ultrasonic waves*. CRC Press, Boca Raton, FL, 2002.

[61] Pao, Y.-H. and Mow, C.-C. *Diffraction of elastic waves and dynamic stress concentrations*. Crane, Russak, New York, 1971.

[62] Kalliopi, K.A. and Philip, D.C. Air content and size distribution of air voids in hardened cement pastes using the section-analysis method. *Cement and Concrete Research*, 29:273–280, 1999.

[63] Nelder, J.A. and Mead, R. A simplex method for for function minimization. *Computer Journal*, 7:308–313, 1965.

[64] Roy, D.M., Brown, P.W., Shi, D., Scheetz, B.E. and May, W. *Concrete microstructure porosity and permeability*. Strat Hwy Res Prog, Report SHRP-C-628, Nat Res Counc, Washington DC, 1993.

[65] Biot, M.A. Mechanics of deformation and acoustic propagation in porous media. *Journal of Applied Physics*, 33:1482–1498, 1962.

[66] Twersky, V. Acoustic bulk parameters in distribution of pair correlated scatterers. *Journal of Acoustical Society of America*, 81:1609–1618, 1987.

[67] Varadan, V.K., Bringi, V.N., Varadan, V.V., and Ishimaru, A. Multiple scattering theory for waves in discrete random media and comparison with experiments. *Radio Science*, 18:321–327, 1983.

[68] Barabanenkov, Y.N. Problem of light diffusion in strongly scattering media. *Physical Review Letters*, 69:1364–1366, 1992.

[69] Sheng, P. *Introduction to wave scattering, localization and mesoscopic phenomena*. Academic Press, San Diego, 1995.

[70] Weaver, R.L. On diffuse waves in solid media. *Journal of the Acoustical Society of the America*, 71:1608–1609, 1982.

[71] Guo, C.B., Holler, D., and Goebbels, K. Scattering of ultrasonic waves in anisotropic polycrystalline metals. *Acustica*, 59:112–120, 1985.

[72] Weaver, R.L. Ultrasonics in aluminum foam. *Ultrasonics*, 36:435–442, 1998.

[73] Page, J.H., Schriemer, H.P., Bailey, A.E., and Weitz, D.A. Experimental test of the diffusion approximation for multiply scattered sound. *Physical Review B*, 52:3106–3114, 1995.

[74] Schubert, F. and Koehler, B. Numerical time-domain simulation of diffusive ultrasound in concrete. *Ultrasonics*, 42:781–786, 2004.

[75] Turner, J.A., and Weaver, R.L. Radiative transfer of ultrasound. *Journal of the Acoustical Society of America*, 96:3654–3674, 1994.

[76] Jeans, J.H. *The dynamical theory of gases, 4th edition.* Cambridge University Press, London, 1925.

[77] Carslaw, H.S., and Jaeger, J.C. *Conduction of heat in solids, 2nd edition.* Oxford University Press, London, 1959.

[78] Glicksman, M.E. *Diffusion in solids: field theory, solid-state principles, and applications.* John Wiley & Sons Inc, NY, 1999.

[79] Becker, J. *Investigation of the microstructure of heterogeneous materials using ultrasonic waves.* Master's thesis, Georgia Institute of Technology, August, 2002.

[80] Weaver, R.L. Diffusivity of ultrasound in polycrystal. *Journal of the Mechanics and Physics of Solids*, 38:55–86, 1990.

[81] Press, W.H., Flannery, B.P., Teukolsky, S.A., and Vetterling, W.T. *Numerical Recipes in C: the Art of Scientific Computing*. Cambridge University Press, Cambridge, 1988.

[82] Punurai, W., Jarzynski, J., Qu, J., Kurtis, K.E. and Jacobs, L.J. Characterization of entrained air voids in cement paste with scattered ultrasound. *NDT & E International*, to appear, 2006.

[83] Arfken, G.B. and Weber, H.J. *Mathematical methods for physicists*. Academic Press, San Diego, 1995.

[84] Abramovicz, M. and Stegun, I.A. *Handbook of mathematical functions*. Dover Press, New York, 1974.